**Instituut voor**
**Kern- en Stralingsfysica**
Departement Natuurkunde
Faculteit Wetenschappen


# Isospin Mixing Impurities and Magnetic Moments Close to the $N = Z$ Line

Promotor:
Prof. Dr. N. Severijns

Proefschrift ingediend tot
het behalen van de graad van
doctor in de wetenschappen
door

**Victor V. Golovko**

**Leuven 2005**

*This thesis is dedicated to my parents, with gratitude and affection.*

# Acknowledgments

At this final stage in my work, I would like to thank all those who have contributed in one way or another to the realization of this thesis. For the last four years my research activities have concentrated on studies of isospin mixing impurities as well as magnetic moments in nuclei close to the $N = Z$ line. The pleasure derived from arriving at an understanding of these concepts has been surpassed only by the pleasure of working with extraordinary people who were just as consumed by the topic: the members of the Nuclear Orientation group at the IKS.

First of all, I am happy to acknowledge Prof. Nathal Severijns for his invaluable encouragement, support and advice on every aspect of the work, as well as for his friendly guidance. Many of the important ideas in this work originate from him. I appreciate particularly his assistance in preparing this thesis, the careful reviewing, checking the entire text for accuracy and offering numerous suggestions to improve clarity. My own understanding of nuclear physics grew significantly with each visit as we discussed the results of experiments, sharpened up arguments or devised more incisive representation.

I am particular indebted to my colleague and co-worker, Titia Phalet for her expert help in all aspects of the low temperature nuclear orientation work. Without her assistance, operating the complicated $He^3$-$He^4$ dilution refrigerator would not have been possible. She has also generously provided detailed comments on my published articles that improved their quality significantly. I thank her for her advice and her effort.

It also has been a pleasure during past four years to work alongside with Marcus

Beck. His wonderful assistance, the fruitful discussions we had, as well as his indispensable knowledge in many different fields and his tremendous enthusiasm have enriched the progress of my research dramatically.

I deeply appreciate the great help in preparation of our experiments and sharing with me the long and difficult beamtime shifts given by the entire NO team; Valentin Kozlov, Sam Coeck. In particular, I would like to thank Il'ya Kraev, who provided a lot of practical help during our stays at ISOLDE/CERN. I would like to thank the former members of the Nuclear Orientation group, particularly, Paul Schuurmans, Bart Vereecke, Stefan Versyck, Bavo Delauré, and Axel Lindroth. Their attitude towards physics in general and towards nuclear physics in particular was always inspiring.

I wish to thank especially my collaborators from HISKP, Bonn University, Germany for their important contributions to this work. It is a pleasure to acknowledge the contribution from Prof. Peter Herzog and Christian Tramm in helping me understand the subject of Nuclear Magnetic Resonance in oriented nuclei.

I am also very much obliged to my collaborators from the Nuclear Physics Institute ASCR, Řež, Czech Republic for their prompt assistance in all research activities during our experiments at ISOLDE/CERN as well as at IKS. I like to thank Prof. Drahos Vénos and Dalibor Zákoucký for their enormous expertise not only in electronics and DAQ, but also in various aspects of nuclear orientation techniques as well as in particle detectors for nuclear physics applications. The help of Prof. Drahos Vénos in developing the code for calculations of spin-relaxation phenomena, which we adopted for our analysis package is highly appreciated.

I would also like to express my gratitude:

- To the IT-team: Luc Verwilst and Joris Knuts, whose expertise in computers and software were much appreciated.
- To the administrative staff of IKS: Josee Pierre, Katia Cools and Sally Vetters, who always provided any possible and impossible help and for their ready counsel and support. I am also indebted to Josee Pierre for her help with my Belgian visa.

- To the people of the mechanical and electronical workshops, whose help in the construction work and manufacturing of experimental devices, was absolutely essential.
- To everyone at IKS for being wonderful colleagues and for the very pleasant time spent together.

Above all, my special gratitude goes to the jury members: Prof. Piet Van Duppen, Prof. Gerda Neyens, Prof. Peter Lievens, Prof. Nathal Severijns, Prof. Peter Herzog and Dalibor Zákoucký, who read the entire manuscript and made many important and helpful comments on it. I hope the final product is better for their efforts than it would have been.

I would like to thank those who provided research funds: the Katholieke Universiteit Leuven (KU Leuven), the Fund for Scientific Research Flanders (FWO), and the IHRP program of the European Commission.

A special note of appreciation goes to my friends, Vika Tsepenko and Valentin Profatilo for their support, friendship, and for the marvellous times we spent together.

Last but not least, I am very grateful for the continuous encouragement and support of my family during this work as well as the rest of my life. Special thanks go to my mother, Vera P. Golovko. I would like to especially thank my father Vasiliy G. Golovko for his invaluable advice continues to guide me in life. He died in June 2002. I want to record here my own profound sense of loss.

Katholieke Universiteit Leuven
Nuclear and Radiation Physics Institute, (IKS)
Leuven, Belgium
April 2005

*Victor V. Golovko*

# Contents

# List of Figures

# List of Tables

# Introduction

During recent years it has become possible to produce many new proton-rich nuclei. Thus, at present most nuclei around the $N = Z$ line that are supposed to be bound have been observed up to $A = 100$. In the mean time, the production rate of most of these nuclei was significantly improved, such that more and more of their properties can be measured, thereby extending our understanding of nuclear structure close to the $N = Z$ line.

This fact has renewed the interest for isospin admixtures in $N = Z$ nuclei. Isospin is a good quantum number under the fundamental assumptions of charge symmetry and charge independence of strong forces, which imply that proton and neutron can be viewed as two different states of the same particle, the nucleon. However, with increasing mass the repulsive Coulomb interaction is expected to dominate over the attractive symmetry energy which tries to minimize the difference between proton and neutron densities. Since the Coulomb interaction does not conserve isospin, isospin mixing can thus be induced in nuclear ground states. The mixing increases with $Z$ and is largest for the $N = Z$ nuclei.

In this work we study isospin mixing in ground states with isospin $T$ from 1/2 to 5 of nuclei ranging from $Z = 29$ to $Z = 47$ (see Table 1). The isospin mixing amplitudes were obtained by combining the $ft$-values for the $\beta$-transitions studied with the asymmetry in the emission of the $\beta$ particles when the nuclei are oriented. These $\beta$ asymmetries were measured with the low temperature nuclear orientation technique. In order to reach a sufficient precision the degree of nuclear polarization has to be known very well. This requires that

**Table 1:** Main properties of the isotopes and $\beta$ transitions of relevance to this work. $E^{\beta}_{\text{end}}$ is the endpoint energy of the $\beta$-transition that was studied to extract the isospin impurity for each isotope.

| Isotope | $T_{1/2}$ | $I^{\pi}$ | $E^{\beta}_{\text{end}}$, keV | $T$ |
|---|---|---|---|---|
| $^{59}$Cu | 82 s | $3/2^{-}$ | 3778 | 1/2 |
| $^{69}$As | 15.4 m | $5/2^{-}$ | 2991 | 3/2 |
| $^{104m}$Ag | 33.5 m | $2^{+}$ | 2708 | 5 |

the temperature and the implantation quality (i.e. the fraction of nuclei 'at good lattice sites') of the sample be determined and that also the product $\mu B_{\text{tot}}$ of the magnetic moment $\mu$ and the total magnetic field the nuclei feel is accurately known. The implantation quality is obtained from a simultaneous measurement of the $\gamma$-ray anisotropies of the isotope studied of another isotope of the same element. The sample temperature is determined with a calibrated $^{57}$CoFe nuclear orientation thermometer that is attached to the sample holder.

As for the second requirement, the hyperfine magnetic field (which is the major contribution to $B_{\text{tot}}$) of all isotopes studied in this work was known with NMR-precision from previous NMR/ON experiments. This was not the case, however, for the magnetic moments. We have therefore determined these moments in a NMR/ON experiment that was carried out on the same sample and in the same experimental run during which the isospin impurity was measured. As these moments are of interest themselves, i.e. in the context of nuclear structure, they form the other main part of this work.

The first two chapters of this work describe the method and the formalism of the nuclear orientation and NMR/ON methods that are used in this work. In addition, the simulations that were performed in order to take into account the effects of scattering and of the magnetic field on the $\beta$-particle trajectories will be described too.

Chapters 3 to 5 contain all relevant information about the experiments that were performed to determine the nuclear magnetic moments of the nuclei studied. In addition, the results are interpreted on the basis of simple theoretical models, and are compared with, albeit less precise, values in the literature.

Chapter 6 contains a discussion of the available simple theoretical models to estimate isospin impurities in various nuclei. We will not try to review all but only the most important models that are available in the literature. In addition, several techniques to measure isospin impurities are discussed with emphasis to the nuclear orientation technique that was used in this work. This leads to an assessment of our ability to use Low Temperature Nuclear Orientation (LTNO) to obtain information about isospin mixing in the ground state of the nuclei studied. A unique and outstanding advantage of the LTNO technique is the possibility to study isospin mixing contributions from the analog state of the daughter (mother) state in $\beta^+$ ($\beta^-$) decay.

Chapters 7 to 8 contain all relevant information about the experiments that were carried out to determine the isospin mixing for $^{59}$Cu and for $^{104m}$Ag. Finally, in Chapter 9 these results compared and discussed with the isospin admixture amplitude that are found in the literature.

# Chapter 1

# Nuclear Orientation

## 1.1 Introduction

The study of the angular distribution of radiation emitted by oriented nuclei has proven to be a powerful tool to deduce both nuclear and hyperfine interactions parameters. Low Temperature Nuclear Orientation (LTNO) exploits the fact that the probability with which a radioactive nucleus emits radiation in a particular direction depends on the degree of orientation,with the orientation axis usually being defined by the direction of an external magnetic field. The technique has the advantage that a rather large degree of orientation can be obtained, compared to other methods. This degree of orientation can be calculated accurately if the temperature and the strength of the orienting interaction are known for isotopes of many elements.

The technique of LTNO is outlined in detail in the monograph edited by Stone and Postma (see Postma and Stone (1986)). The general nuclear orientation formalism for almost any type of radiation is given in Krane (1986). In this work we will restrict to the emission of $\gamma$-rays and $\beta$-particles from oriented nuclei. The information from $\gamma$-asymmetries will be used mostly for nuclear orientation thermometry (Marshak (1986)), as well as for the determination of the fraction of the nuclei feeling the full orienting magnetic field. The information from

the $\beta$-asymmetry will be used to determine the nuclear magnetic moments of various isotopes, as well as to extract information on isospin impurities in nuclei close to the $N = Z$ line.

Nuclear spin-relaxation can significantly affect the degree of orientation when using the On-Line low temperature Nuclear Orientation (OLNO) technique. For a quantitative analysis of the data it is then useful to work with so-called attenuation coefficients, which take into account the effects of the relaxation process, and which modify the orientation parameter $B_\lambda$. Klein in chapter 12 of Postma and Stone (1986) outlined in detail the theory of nuclear spin-lattice relaxation related to nuclear orientation.

## 1.2 Nuclear Orientation Formalism

In a magnetic field $B$ a nuclear level with a spin $I$ is Zeeman splitted into magnetic sub-levels with quantum numbers $m = I, I-1, I-2, \ldots, -I$. The splitting is determined by $E_m = -m\mu B/I$ with $\mu$ the nuclear magnetic dipole moment. For an ensemble of nuclei in thermal equilibrium at temperature $T_L$, the Boltzman distribution function governs the population probabilities

$$p_m = \frac{\exp(-E_m/kT_L)}{\sum_m \exp(-E_m/kT_L)} \tag{1.1}$$

To achieve a reasonable difference between these population probabilities $p_m$ the thermal energy $kT_L$ should be comparable to the energy splitting of the sublevels

$$\Delta E_{m\leftrightarrow m+1} = E_m - E_{m+1} = \frac{\mu}{I}B \tag{1.2}$$

This leads to the requirement that $B/T_L$ should be of order $10^4$ T/K, which demands large magnetic fields (i.e. tens of Tesla) and low temperatures (typically in the mK region). This is achieved in this work by the combination of several experimental techniques: i.e. the $^3$He-$^4$He dilution refrigerator NICOLE (Nuclear Implantation into Cold On Line Equipment; see Berkes et al. (1985)), which allows to reduce the temperature of a sample down to the mK region, and implantation of the radioactive ions into a Fe host lattice in which a large hyperfine field is induced by a 2 Tesla superconducting split-coil magnet in the dilution refrigerator.

The spatial distribution of radiation emitted by oriented nuclei can be described by the angular distribution function $W(\theta)$ which gives the probability to detect radiation at an angle $\theta$ with respect to the orientation axis. This function has the form (assuming cylindrical symmetry)

$$W(\theta) = 1 + f \sum_{\lambda} B_\lambda U_\lambda A_\lambda Q_\lambda P_\lambda (\cos\theta) \tag{1.3}$$

where $P_\lambda(\cos\theta)$ are the Legendre polynomials; $f$ represents the fraction of the nuclei that can be found at "good lattice sites", experiencing the full hyperfine interaction, while the rest $(1-f)$ is supposed to feel no interaction at all; $B_\lambda$ are the nuclear orientational parameters; $U_\lambda$ are the deorientation coefficients, which account for the effect of unobserved intermediate radiations (see Krane (1986)); $A_\lambda$ are the directional distribution coefficients which depend on the properties of the observed radiation itself, and $Q_\lambda$ are solid angle correction factors. Only terms with $\lambda = \textit{even}$ occur for $\gamma$-radiation while for $\beta$-radiation, both $\lambda = \textit{even}$ and $\lambda = \textit{odd}$ terms can be present. In the next paragraphs these factors are explained in more detail.

### 1.2.1 Orientation parameters $B_\lambda$

The orientation parameters $B_\lambda$ describe the orientation of a nuclear ensemble with spin $I_0$ when the orientation mechanism has axial symmetry. They are given by

$$B_\lambda = [(2\lambda+1)(2I_0+1)] \sum_m (-1)^{I_0+m} \begin{pmatrix} I_0 & I_0 & \lambda \\ -m & m & 0 \end{pmatrix} p_m. \tag{1.4}$$

The $B_\lambda$ are normalized such that $B_0 = 1$ when $\sum_m p_m = 1$, while the triangle condition for $3j$-symbols requires that $0 \leq \lambda \leq 2I_0$. The population probabilities are given by the Boltzmann distribution (see Eq. 1.1). Since this distribution depends on the ratio between the energy splitting of the nuclear sub-levels and the temperature, the energy difference is often conveniently expressed in units of temperature (mK). This quantity is also called the "interaction temperature".

$$T_{\rm int}(\text{mK}) = \frac{0.366\mu(\mu_{\rm N})B_{\rm tot}(\text{Tesla})}{I_o(\hbar)} \tag{1.5}$$

The $B_\lambda$ were tabulated originally by Krane (1973). Later these tables were extended to take into account the effects of relaxation (see Shaw and Stone (1989) and Vénos et al. (2003)).

Because of the temperature dependence of the orientation parameters, a measurement of the anisotropy as a function of the temperature makes it possible to deduce the strength of the interaction (i.e. the product of the nuclear magnetic moment $\mu$ and the total magnetic field $B_{\mathrm{tot}}$ at the site of the nucleus). Alternatively, knowing the hyperfine interaction, the temperature can be deduced from the observed anisotropy (this is the main principle of nuclear orientation thermometry, as outlined in detail in Marshak (1986)). Furthermore, because of this same feature it is rather easy to vary the degree of polarization by changing the sample temperature. This is in contrast with polarization achieved in e.g. nuclear fusion-evaporation reactions or through nuclear decay or laser optical pumping, where the degree of orientation is a fixed quantity determined by angular momentum coupling factors.

### 1.2.2 Deorientation coefficients $U_\lambda$

In general nuclear orientation experiment the observed radiation is not necessarily emitted by the oriented state with spin $I_0$ but rather from a state $I_\mathrm{i}$ that is reached from $I_0$ via a number of unobserved transitions. The effect of these unobserved intermediate transitions is accounted for by introducing the deorientation coefficients $U_\lambda$ that essentially modify the orientation coefficients $B_\lambda$ such that they are valid for the initial sate $I_\mathrm{i}$

$$B_\lambda(I_0, I_\mathrm{i}) = U_\lambda(I_0, \cdots, I_\mathrm{i}) B_\lambda(I_0). \tag{1.6}$$

An expression for the $U_\lambda(I_0, \cdots, I_\mathrm{i})$ can be found in Krane (1986).

### 1.2.3 Nuclear spin-lattice relaxation in on-line LTNO

With OLNO the activity is produced and directly implanted into the cooled host at ∼10 mK, with a travel time through the radioactive beam distribution system of much less than one second. The on-line technique therefore allows

the systematic study of nuclei far from the stability line which is not possible with conventional off-line LTNO.

In order to achieve on equilibrium on-line nuclear orientation, two requirements must be fulfilled:

- a static interaction is required to split the nuclear sub-levels, combined with a low enough temperature so that $\Delta E \geq kT$ (where $\Delta E$ is the sub-level energy splitting; see Eqs. 1.1 and 1.2),
- a sufficiently strong interaction must exist between the *hot* implanted nuclei and the *cold* host lattice so that the nuclei relax to the lattice temperature in a time that is short compared to their half-life.

The second condition is of particular importance for OLNO, where the half-life can often be short enough to be comparable with the relaxation time. If this is the case, the orientation observed will be attenuated compared with the full thermal equilibrium value, and a detailed knowledge of the relaxation mechanism is essential for a complete analysis.

The theory of nuclear spin-lattice relaxation (SLR) has been developed for nuclear orientation by several authors, see e.g. Bacon et al. (1972), Klein (1983), and Shaw and Stone (1988); Shaw and Stone (1989). In particular, Klein (1986) has given a very complete treatment of the problem. Theoretical predictions of the relaxation time $T_1$ (assuming to first approximation a single exponential behavior) based on the Green's functions method for impurities in ferromagnetic iron are given in Akai (1988).

For on-line experiments the impurity concentration is in general so low (a few ppm or less) that the single impurity limit is assumed to be valid at all times (i.e. each nucleus is coupled only to the host lattice and mutual interactions within the nuclear spin system can be neglected). The impurity nuclei are simply too far apart (on average many tens of lattice spacings) for spin-spin interactions to produce a spin temperature. In this limit the nuclei all relax independently and the level populations will not obey a Boltzmann distribution (i.e. the nuclear system cannot be characterized by means of a temperature).

In the formalism of Klein (1986) the time-dependent angular distribution of

radiation from nuclei oriented by an axially-symmetric static interaction (see Eq. 1.3) is given by

$$W(\theta) = 1 + f \sum_{\lambda} B_{\lambda}(p_m(t)) U_{\lambda} A_{\lambda} Q_{\lambda} P_{\lambda}(\cos\theta) \tag{1.7}$$

where the orientation parameters $B_\lambda(p_m(t))$ describe the nuclear orientation through the time-dependent population probabilities $p_m(t)$ of the sub-levels of the oriented state. Assuming absence of any external perturbation, infinite lifetime, and constant temperature $T_L$, the $p_m(t)$ will always tend towards the thermal equilibrium time-independent Boltzmann values given by Eq. 1.1.

During continuous implantation of the radioactive beam, the sub-level populations of the implanted nuclear ensemble attain a secular equilibrium (theoretically at $t = \infty$, practically: the implantation time is much longer than the lifetime of the radioactivity) for which the condition $dp_m(t)/dt = 0$ applies and which is found somewhere between the initial, i.e. equal populations, and the thermal equilibrium populations given by Eq. 1.1. In this condition the observed angular distribution can be described in terms of attenuated orientation parameters $B_\lambda(\mathrm{sec})$ which are reduced with respect to the thermal equilibrium orientation parameters $B_\lambda(\mathrm{th})$ by factors $\rho_\lambda$, i.e.,

$$B_\lambda(\mathrm{sec}) = \rho_\lambda(I, T_\mathrm{i}, T_\mathrm{L}, C_\mathrm{K}) B_\lambda(\mathrm{th}), \tag{1.8}$$

where $C_\mathrm{K}$ is the Korringa relaxation constant. An overview of measured values of $C_\mathrm{K}$ for ferromagnetic host metals is given in Klein (1986). Shaw and Stone (1989) have tabulated attenuation coefficients $\rho_\lambda$ for $\lambda = 2, 4$. Recently Vénos et al. (2003) extended those tables to include also terms with $\lambda = 1, 3, 6$ and 8. Later we will show the importance of taking into account relaxation effects for our experiments.

The Korringa law relates the Knight shift $K$ and the relaxation constant $C_\mathrm{K}$ as

$$K^2 \gamma_\mathrm{n}^2 C_\mathrm{K} = \frac{\hbar}{4\pi k_\mathrm{B}} \gamma_\mathrm{e}^2 \tag{1.9}$$

where $\gamma_\mathrm{e}$ and $\gamma_\mathrm{n} = \mu\mu_\mathrm{N}/(\hbar I)$ are the gyromagnetic ratios of the electron and the nucleus. From a practical point of view, it is more convenient to use instead Eq. 1.9 the formula (Matsuta et al. (1996))

$$C_\mathrm{K} = \left( \mathrm{K}^2 A \left( \frac{\mu}{I} \right)^2 \right)^{-1} \tag{1.10}$$

where

$$A = \frac{2\pi^2 k_{\mathrm{B}}}{h} \left( \frac{\mu_{\mathrm{N}}}{\mu_{\mathrm{B}}} \right)^2 . \tag{1.11}$$

Since the Knight shift depends on the local electron densities at the Fermi level, which is identical for different isotopes of the same element, Eq. 1.9 implies that for two different isotopes of the same element in a given host the following relation between their $C_{\mathrm{K}}$ values and gyromagnetic ratios $\gamma_{\mathrm{n}}$ holds

$$(\gamma_{\mathrm{n}}^2 C_{\mathrm{K}})_1 = (\gamma_{\mathrm{n}}^2 C_{\mathrm{K}})_2. \tag{1.12}$$

If $C_K$ is thus known for one isotope of a given element it can be calculated for any other isotope of that element provide the $g$-factors are known. If for none of the isotopes of a given element $C_K$ is known from experiment, one can still estimate the relaxation time in Fe from the empirical relation for the relaxation of impurities in Fe given in Klein (1986), i.e.

$$C_{\mathrm{K}} T_{\mathrm{int}}^2 = 1.4 \cdot 10^{-4} \mathrm{s} \cdot \mathrm{K}^3, \tag{1.13}$$

which holds for $B_{\mathrm{ext}} \geq 0.5$ T and is usually valid up to a factor of 4.

For practical purposes it is further useful to use the relation

$$T_1 \approx \begin{cases} C_{\mathrm{K}}/IT_{\mathrm{int}} & \text{for } T_{\mathrm{L}} \leq IT_{\mathrm{int}} \\ C_{\mathrm{K}}/T_{\mathrm{L}} & \text{for } T_{\mathrm{L}} \geq IT_{\mathrm{int}} \end{cases} \tag{1.14}$$

to estimate the relaxation time $T_1$ for a given isotope in a Fe host lattice at a given lattice temperature $T_{\mathrm{L}}$. Finally, it is important to note that the value $C_K$ is depending on the magnetic field strength (Klein (1986)). Saturation occurs at $B_{\mathrm{ext}} \simeq 0.5$ T, while at e.g. $B_{\mathrm{ext}} \simeq 0.1$ T relaxation proceeds a factor of $\simeq 2.5$ faster than at $B_{\mathrm{ext}} \geq 0.5$ T.

### 1.2.4 The angular distribution coefficients $A_\lambda$

The angular distribution coefficients describe the observed transition between the initial state $I_i$ and the final state $I_f$. They depend on the properties of the radiation and, therefore, should be treated separately for $\gamma$- and $\beta$-radiation.

### Gamma radiation

The general formula for the angular distribution coefficients for $\gamma$-radiation is quite complicated and given elsewhere (Krane (1986)). Here we consider the case when only two multipoles contribute ($L$ and $L' = L + 1$). The angular distribution coefficient is then given by:

$$A_\lambda = \frac{F_\lambda(LLI_fI_i) + 2\delta F_\lambda(LL'I_fI_i) + \delta^2 F_\lambda(L'L'I_fI_i)}{1+\delta^2} \tag{1.15}$$

where the $F_\lambda$ are tabulated in Yamazaki (1967), and $\delta$ is a the multipole mixing ratio (i.e. for $E_2$ and $M_1$ multipoles contributing)

$$\delta = 0.835 E_\gamma(\text{MeV}) \frac{\langle I_f||E_2||I_i\rangle(\text{eb})}{\langle I_f||M_1||I_i\rangle(\mu_N)} \tag{1.16}$$

with $\langle I_f||E_2||I_i\rangle$ and $\langle I_f||M_1||I_i\rangle$ reduced matrix elements. The relative amplitude of each multipolarity in the transition is then determined by $\delta^2/(1+\delta^2)$.

### Beta radiation

The description of the full Hamiltonian in nuclear $\beta$-decay is quite complex (i.e. Lee and Yang (1956)). In order to simplify it a few assumptions can be made:

- The interaction is assumed to be of pure V-A (Vector and Axial vector) type, with maximal parity violation.
- Time reversal invariance is assumed.
- The neutrino is assumed to be massless and therefore to move at velocity $c$ and to have fixed helicity.
- Only allowed decays are considered.

**Allowed $\beta$-decay** In allowed $\beta$-decay, the total orbital angular momentum $L$ of the two leptons ($\beta$-particle and neutrino) is zero. The selection rules are (see also Table 1.1):

$$\pi_i\pi_f = +; \quad |I_i - I_f| = 0, 1 \tag{1.17}$$

**Table 1.1:** Selection rules for allowed nuclear $\beta$-decay. $I$ represents the nuclear spin, $T$ the isospin and $\pi_{i,f}$ the parity of initial and final states.

| | F | GT |
|---|---|---|
| $\Delta I$ | 0 | 0,1 (no $0 \rightarrow 0$) |
| $\Delta T$ | 0 | 0,1 (no $0 \rightarrow 0$) |
| $\pi_i \pi_f$ | + | + |

In this case only $\lambda$=1 terms differ from zero, due to angular momentum coupling in the so-called particle parameters which appear in the most general expression for the $\beta$-angular distribution coefficients (Krane (1986)).

When $I_f = I_i = 0$ only the Fermi (vector) matrix element contributes to the decay and no anisotropy can be observed. For the case $I_i - I_f = 1$, only the Gamow-Teller (axial vector) matrix element contributes and

$$A_1(\beta^{\pm}) = \begin{cases} \mp\frac{v_\beta}{c}\sqrt{\frac{I+1}{3I}} & \text{if } I_f = I_i - 1 \\ \pm\frac{v_\beta}{c}\sqrt{\frac{I}{3(I+1)}} & \text{if } I_f = I_i + 1 \end{cases} \tag{1.18}$$

with $I = I_i$. The upper (lower) sign applies for $\beta^+$-decay ($\beta^-$-decay).

If, finally, $I_f = I_i \neq 0$ there is interference between the Fermi matrix element $M_F$ and the Gamow-Teller matrix element $M_{GT}$. In this case:

$$A_1(\beta^{\pm}) = \frac{v_\beta/c}{1+y^2}\left[\frac{\mp 1}{\sqrt{3I(I+1)}} + \frac{2}{\sqrt{3}}y\right] \tag{1.19}$$

with $y = \frac{C_V M_F}{C_A M_{GT}}$ the Fermi/Gamow-Teller mixing ratio with $C_V = 1.00$, $C_A = -1.27$ being the vector, respectively the axial-vector coupling constants. The $A_1$-parameter is generally called the $\beta$-asymmetry parameter.

### 1.2.5 The solid angle correction factors $Q_\lambda$

In the discussion so far it was assumed that the source and the detector were geometrical points such that the emission angle could be uniquely defined. In a

real experiment the detector as well as the source have finite solid angles. The anisotropy that is observed by a detector placed at an angle $\theta$ (with respect to the detector axis) is in fact an average over all possible emission angles that connect the source with the detector. When the detection system has axial symmetry, one can define the response function of a detector $\varepsilon(\zeta, E)$. This function describes the efficiency of the detector for radiation emitted with energy $E$ under an angle $\zeta$ relative to the detector axis.

- $\gamma$-radiation: $\varepsilon(\zeta, E) = 1 - e^{-\tau(E_\gamma)x(\zeta)}$ where $\tau(E_\gamma)$ is the $\gamma$-ray absorption coefficient and $x(\zeta)$ the distance the $\gamma$-ray travels in the detector material. In the absorption coefficient only the photo-peak efficiency is taken into account.
- $\beta$-radiation: $\varepsilon(\zeta, E) \approx 1$ which is true for all particle detectors used here since these were made made from highly purified germanium (HPGe) and have a thickness[1] of at least 3 mm.

For an axially symmetric detector $Q_\lambda$ can be calculated using Rose (1953):

$$Q_\lambda = \frac{\int_0^\xi P_\lambda(\cos\zeta)\varepsilon(\zeta, E)\sin\zeta\, d\zeta}{\int_0^\xi \varepsilon(\zeta, E)\sin\zeta\, d\zeta} \tag{1.20}$$

with $\xi = \arctan(\rho/d)$, where $d$ is the source to detector distance while $\rho$ is the radius of the active part of the detector. In Heighway and MacArthur (1970) it was shown that with good accuracy the solid angle corrections $Q_\lambda$ in Eq. 1.20 could be approximated as:

$$Q_\lambda = Q_\lambda^{\text{source}} \cdot Q_\lambda^{\text{detector}} \tag{1.21}$$

where $Q_\lambda^{\text{source}}$ is the finite solid angle correction coefficient for a realistic source and point detector, and $Q_\lambda^{\text{detector}}$ is the finite solid angle correction coefficient for a realistic detector and a point source. Schuurmans (1996) showed that evaluation of the integral in Eq. 1.20 then yields a simple analytic expression for $Q_\lambda$:

$$Q_\lambda^{\text{source,detector}} = \frac{P_{\lambda-1}(\cos\xi) - \cos\xi P_\lambda(\cos\xi)}{(\lambda+1)(1-\cos\xi)} \tag{1.22}$$

[1] The thickness of the detectors was chosen for each experiment in such a way that it was just sufficient to completely stop $\beta$-particles up to the endpoint energy of the radioactive isotope under study.

It should be noted that in Eq. 1.22 the effect of the applied magnetic field on the emission direction of the $\beta$-particle, as well as any possible scattering effects were neglected. These effects will be discussed in the following paragraphs.

### The applied magnetic field and the emission direction of charged particles

The path of charged particles, like $\beta$-particles emitted by radioactive nuclei, is influenced by a magnetic field if the particles have a velocity component perpendicular to the field. The influence may distort the observed anisotropy since in principle the direction in which the $\beta$-particle is detected is not the direction in which it was emitted. To estimate the effect of the external field on the angular distribution we will assume that the applied magnetic field is homogeneous in the region the $\beta$-particle travels through. A charged particle having a velocity vector that has a component parallel to a uniform magnetic field moves in a helical path. For a relativistic particle like a $\beta$-particle the radius $r$ of the path is proportional to the relativistic momentum $m_\beta \gamma v_\beta$ of the $\beta$-particle and inversely proportional to the magnitude of the magnetic field $B$ and the charge of the $\beta$-particle:

$$r = \frac{m_{\beta_0} \gamma v_\beta}{qB}, \tag{1.23}$$

where

$$\gamma = \frac{1}{\sqrt{1 - \left(\frac{v_\beta}{c}\right)^2}} \tag{1.24}$$

is a relativistic correction factor, and $m_{\beta_0}$ is the rest energy of the electron. For an electron the velocity can be expressed relative to the speed of light as:

$$\frac{v_\beta}{c} = \sqrt{1 - \frac{(m_{\beta_0} c^2)^2}{(E_{\text{kin}} + m_{\beta_0} c^2)^2}} \tag{1.25}$$

For a typical $E_{\text{kin}} = 1$ MeV electron one has $\frac{v_\beta}{c} = 0.9411$ (here we used $m_{\beta_0} c^2$ = 511 keV in Eq. 1.25). Substituting $\frac{v_\beta}{c}$ in Eq. 1.23 one then finds for an external field $B = 0.1$ T[2] that the helical radius is $r \approx 47$ mm. This illustrates

[2]This is the typical value of the external magnetic field that we used during our experiments.

the importance of corrections related to the effect of the external magnetic field on the $\beta$-particles.

#### Scattering effects

Another possible cause of distortion of the radiation's emission pattern, as observed by the detectors, are scattering effects. In this respect one can distinguish three different sources: scattering in the host lattice, scattering on the walls of the vacuum chamber and the magnet, and finally (back)scattering on the detector itself. The interaction of the $\beta$-particle with the different materials can cause a loss of energy and a change (sometimes significant) in the travelling direction of the particle. The latter has its evident effect on the angular distribution pattern. The former makes that the particle is detected at lower energies and possibly (if the energy loss is large enough) that it does not contribute to the observed spectrum. To investigate various scattering effects and their contributions into finite solid angle corrections GEANT4 calculations were performed. The results of these calculations will be discussed latter.

## 1.3 Experimental set-up

All radioactive nuclei used here were produced at the ISOLDE facility at CERN (see Kugler et al. (1992) and Kugler (2000)). Here we describe only the general principle and layout of the experimental set-up used in this work. More relevant details about each experiment (target material, particle detectors, and so on) are given later in the chapters dedicated to the particular experiments. The layout of the ISOLDE facility is displayed in Fig. 1.1.

Typically a 1.2 or 1.4 GeV proton beam from the CERN PS-Booster accelerator is used for production of the radioactive species. This beam hits a target near the ion source set-up. Because of the very high beam energies at ISOLDE, very thick targets can be used. This leads to production yields which are often considerably higher than those obtained with mass separators at heavy ion accelerators where typically less than $10^6$ atoms/s are produced. The isotopes produced in the target are ionized and then extracted from the

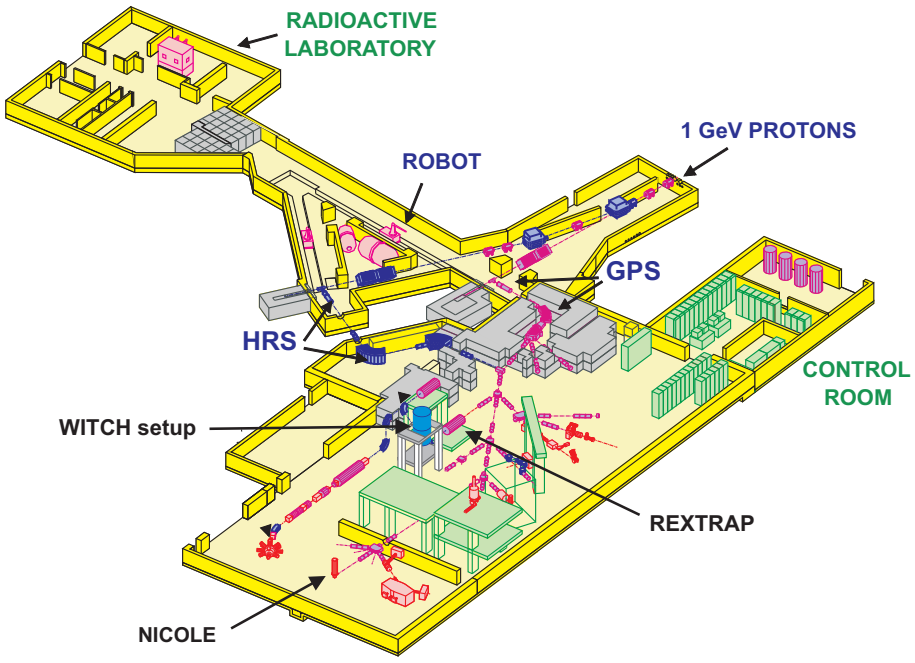


**Figure 1.1:** Layout of the ISOLDE facility

ion source, accelerated to 60 keV and separated according to $A/q$ in a dipole magnet. In practice, at ISOLDE it is possible to use two different on-line mass separators: the General Purpose Separator (GPS, with mass resolving power $M/\Delta M \simeq 2600$) and the High Resolution Separator (HRS, with mass resolving power $M/\Delta M \simeq 6000$). In this work we used both machines for different isotopes. A particular mass is selected and then transported electrostatically, via a beam transport line of several tens of meters, to our cryogenic equipment. There the isotopes are implanted continuously in the host material (99.99 % high purity Fe foils were used), which is soldered to the cold finger of a $^3$He-$^4$He dilution refrigerator (with cooling power of 400 $\mu$W at 100 mK) with top-loading facility (see Berkes et al. (1985)). The latter makes it possible to access the sample during operation. The NICOLE (Nuclear Implantation into Cold On-Line Equipment) refrigerator (see Fig. 1.2) is supplied with a side access facility of approximately 1 m length that connects the refrigerator

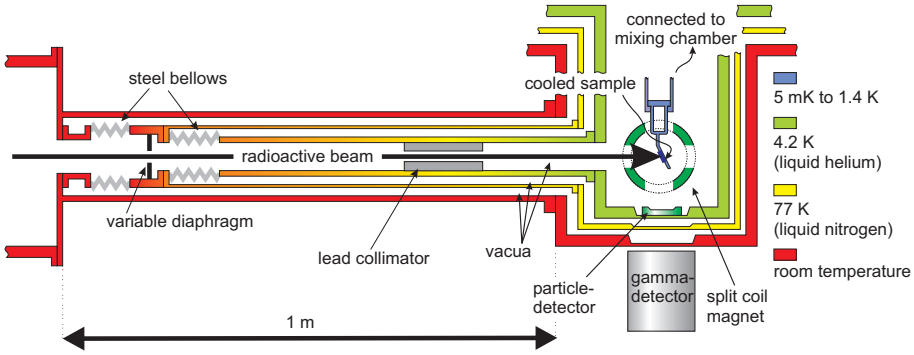


**Figure 1.2:** Cross section through the lower part of the NICOLE refrigerator (Wouters et al. (1990); Schlösser et al. (1988)) and the side access tube. The orientation axis coincides with the direction of the magnetic field, which is perpendicular to the plane of the figure. A multistage shielding serves to reduce the heat load from room temperature onto the sample. As a result, temperatures around 8 to 10 mK can be achieved in on-line conditions with continuous implantation of the radioactive source.

with the beam distribution system of ISOLDE by means of three concentric tubes, the inner two connected to the helium bath (4 K) and the nitrogen bath (77 K), and the outer one forming the eventual vacuum insulation at room temperature. In addition a movable diaphragm at the entrance of the 77 K cooled tube and 5 cm long lead collimator with 5 mm diameter inside the 4 K tube reduce the heat load on the sample from radiation from the beam line.

With this configuration the total heat load is reduced by about a factor $10^4$, which enables to maintain low temperatures of about 8 to 10 mK while continuously implanting a radioactive beam. This beam access tube can in addition be closed with a 4 K radiation baffle at the entrance of the refrigerator to obtain lowest temperatures around 5 mK in measurements with longer lived isotopes. This 4 K baffle is equipped with a Faraday cup and four 90° sectors are mounted on the entrance surface of the lead collimator for reasons of beam diagnostics. Stable beams are used to adjust and check the separator beam focusing and transmission to the refrigerator[3]. A superconducting split-coil

[3]We can estimate the bending of an radioactive ions in the presence of the strong external magnetic field $B_{\text{ext}} = 0.1$ T. First, we must calculate the speed of the ions using the fact that the increase in their kinetic energy must equal the change in their potential energy, i.e.

magnet is used to produce a magnetic field to polarize the Fe host foils and the nuclear orientation thermometer. The refrigerator and side access components are constructed by Oxford Instruments Ltd.

Fig. 1.3 shows the NICOLE set-up surrounded with three $\gamma$-detectors with approximately 5 cm diameter high purity germanium (HPGe) crystals, installed at a distance of about 9 cm from the sample at angles of 0° (horizontal), 90° (vertical) and 180° (horizontal) with respect to the orientation axis (i.e. external magnetic field). In addition, three HPGe particle detectors (see Zákoucký et al. (2004), Vénos et al. (2000) and Fig. 1.4) were installed inside the refrigerator for detection of $\beta$-particles. For NMR/ON experiments (Nuclear Magnetic Resonance on Oriented Nuclei, i.e. Matthias and Holliday (1966)) a two-windings copper coil mounted on a plastic frame is installed in the 0.6 K radiation shield that is situated around the sample. Fig. 1.2 from Chapter 4 shows the cross section of the lower part of the NICOLE refrigerator with the position of the NMR coil and of the HPGe particle detectors relative to the sample indicated as well.

## 1.4 Nuclear Magnetic Resonance on Oriented Nuclei (NMR/ON)

LTNO involves the detection of a difference in nuclear substate populations through the consequent anisotropy in emission of decay products from the oriented ensemble. The temperature dependence of this anisotropy allows determination of the level splittings with a precision, at best, of a few percent and with little sensitivity. As early as 1953 it was pointed out by Bloembergen and Temmer (1953) that resonant absorption by the nuclear ensemble would produce changes in substate population detectable as changes in the anisotropy and hence the precision of substate splitting measurements could be greatly improved whilst the high sensitivity of the emission signal was re-

$\frac{1}{2}mv^2 = qU$, where $m$ is the ion mass, $v$ is the ions speed, $q$ is the ions charge, and $U$ is a potential difference of 60 kV. For $^{59}$Cu ions we have $v \approx 4.4 \cdot 10^5$ m/s. Then, we use Eq. 1.23 (assuming non-relativistic case) to find the radius of the helical path, i.e. $r \approx 3$ m. Thus, we can neglect the bending of the implanted radioactive ions.

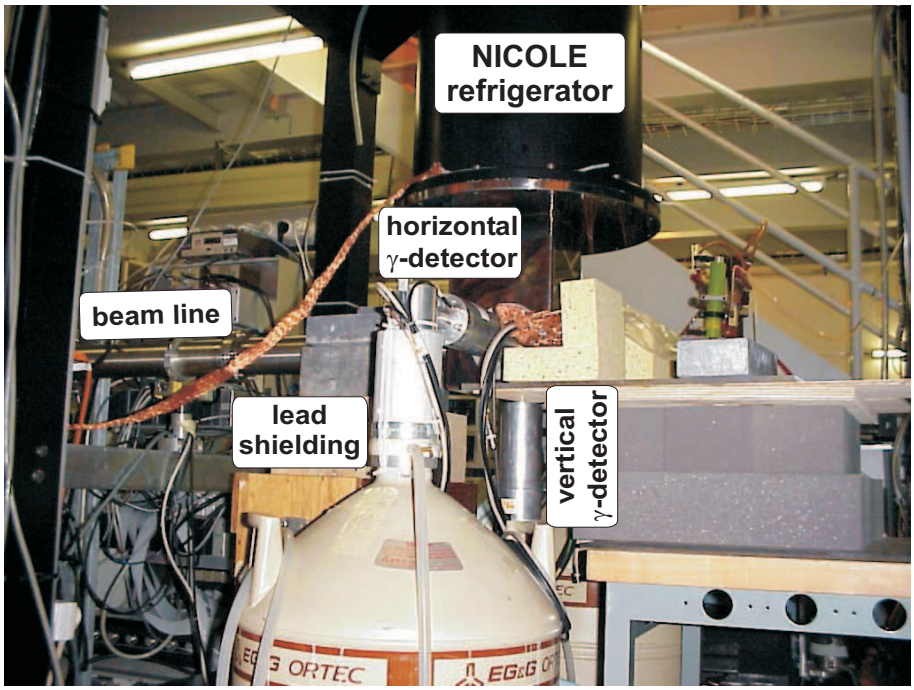


**Figure 1.3:** Lower part of the NICOLE set-up installed at ISOLDE/CERN. A cross section view of the lower part is shown in Fig. 1.2, with the position of the NMR coil and of the HPGe particle detectors relative to the sample indicated as well.

tained. NMR/ON yields a precision that is typically about a few orders of magnitude better then what can be achieved with LTNO.

All that is required to adapt a NO system for NMR/ON is the introduction of a radiofrequency (rf) generator feeding a simple loop coil positioned to give an oscillating field at the oriented nuclear sample which is perpendicular to the orientation axis. A schematic arrangement is given in Fig. 1.5. The parameters which govern the choice of oscillator are its available power, frequency range and modulation characteristics, while they depend on the choice of nuclei. These details will be provided for each NMR/ON experiment separately, later. Here we discuss some common conditions for observing NMR/ON.

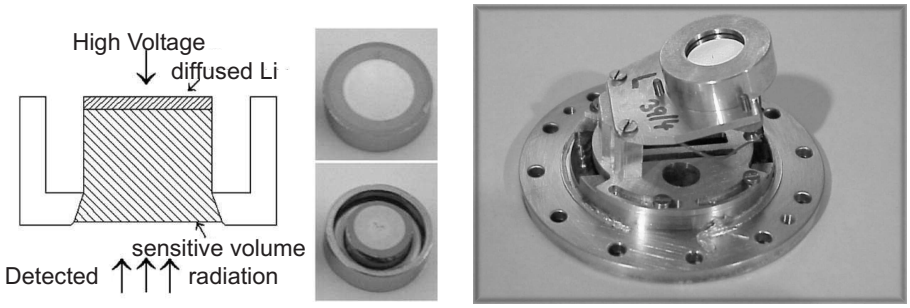


(a) (b)

**Figure 1.4:** (a): Drawing and pictures of the HPGe detector (see Zákoucký et al. (2004) and Vénos et al. (2000)). (b): HPGe detector mounted on 4 K radiation shield.

To detect NMR/ON, a measurable perturbation of the radiation anisotropy must occur and be clearly identified as being caused by direct nuclear absorption of applied rf-power. This involves, in all cases, consideration of

- the rate at which power can be absorbed by the cooling system,
- the available rf-field at the nuclei,
- the nuclear spin lattice relaxation time (it is discussed in more details in Chapter 4),
- the width of the nuclear resonance.

The specific features associated with each item in this list are given in Stone (1986). To determine the magnetic moments reported in this work NMR/ON was combined with $\beta$-detection in the NICOLE set-up. The first $\beta$-NMR/ON experiment performed with the LNTO NICOLE set-up was reported by Rikovska et al. (2000). However, for that measurement particle detectors were installed outside the refrigerator, thereby causing additional scattering of $\beta$ particles. In this work we performed $\beta$-NMR/ON with HPGe particle detectors mounted on the 4 K radiation shield, thereby reducing scattering of $\beta$-particles. The $\gamma$-rays were detected with large volume HPGe detectors placed outside the refrigera-

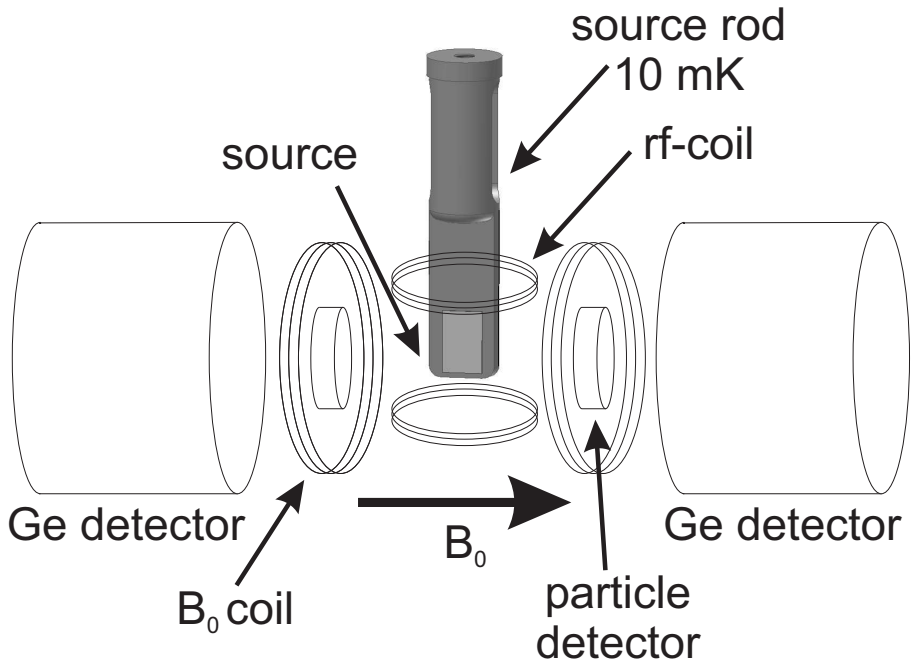


**Figure 1.5:** Arrangement of rf coils for NMR/ON. The radioactive source is implanted in Fe foil on the cold finger. A polarizing field $B_0$ created by split-coil superconducting magnet, which is perpendicular to rf-field from the loop coil.

tor (see Chapter 5). The detectors arrangement for each particular NMR/ON experiment will be discussed later.

The rf oscillating field is applied perpendicular to the external magnetic field. The NMR coil producing this field in our experiment consisted of a pair of two-turn coils mounted on a plastic frame and fixed inside the 1.2 K shield around the sample. It is fed from the top of the refrigerator by miniature coaxial cables and connected to a Marconi frequency generator with a range from 10 kHz to 3.3 GHz. In addition to the NMR-coil a pick-up coil for monitoring the rf signal was installed too. The level of the rf signal was always adjusted such that a small change of anisotropy of the $\beta$-particles could be observed.

The resonance frequency $\nu_{\mathrm{res}}$, which corresponds to the energy difference between the Zeeman splitted nuclear sublevels and is probed by scanning the

radio frequency while observing the destruction of the anisotropy of the emitted radiation, is related to the nuclear magnetic moment through the relation

$$\nu_{res} = \frac{\mu}{Ih} \left[ B_{\mathrm{hf}} + B_{\mathrm{ext}} \left(1 + K\right) - B_{\mathrm{dem}} \right] \tag{1.26}$$

with $K$ the Knight shift, $B_{\mathrm{hf}}$ the hyperfine magnetic field, $B_{\mathrm{ext}}$ the external magnetic field, and $B_{\mathrm{dem}}$ the demagnetization field. However, from a practical point of view it is more easy to use

$$\nu_{\mathrm{res}}(\mathrm{MHz}) = \frac{7.623 \cdot \mu(\mu_{\mathrm{N}})\mathrm{B_{tot}(Tesla)}}{\mathrm{I}(\hbar)} \tag{1.27}$$

with $B_{\mathrm{tot}} = B_{\mathrm{hf}} + B_{\mathrm{ext}} \left(1 + K\right) - B_{\mathrm{dem}}$.

The calculation of the demagnetization field is not straightforward and analytical expressions can be obtained only for very simple shapes. For polycrystalline samples of a regular shape the demagnetization field can be written as (see Chikazumi (1964)):

$$B_{\mathrm{dem}} = -\mu_0 \hat{\mathbf{D}} \mathbf{M} \tag{1.28}$$

in which $\mu_0$ is the permeability of vacuum while $\hat{\mathbf{D}}$ is the demagnetization tensor. Only the diagonal elements of $\hat{\mathbf{D}}$ are nonzero because of the magnetic isotropy of the sample. For a thin foil with length $a$, width $b$ and thickness $c$ with the condition that $a > b \gg c$, the diagonal elements of $\hat{\mathbf{D}}$ are approximately given by:

$$\begin{aligned} D_a &\approx \frac{\pi c}{4a} \left[ 1 - \frac{a-b}{4a} - \frac{3}{16} \left( \frac{a-b}{a} \right)^2 \right] \\ D_b &\approx \frac{\pi c}{4a} \left[ 1 + \frac{5(a-b)}{4a} - \frac{21}{16} \left( \frac{a-b}{a} \right)^2 \right] \\ D_c &= 1 - D_a - D_b. \end{aligned} \tag{1.29}$$

Substituting typical values for the dimensions of the iron foils used for the experiments of this work (i.e. $a \approx 14$ mm, $b \approx 9$ mm, $c \approx 0.125$ mm) and using the magnetization value for iron $\mu_0 \mathbf{M} = 2.29$ T we get for the demagnetization field in each direction: $B_{\mathrm{dem}}(a : b : c) = (14.2;\ 25.9;\ 2249.8)$ mT. This shows that in our thin foil the external field applied along the $b$-direction will be reduced by $B_{\mathrm{dem}} = 0.0259(52)$ T. In order to account for approximations made to get to Eq. 1.29 we have adopted a 20 % error to this value.

It is found experimentally that the hyperfine field does not have a sharp value but a certain distribution (Leuthold et al. (1980)). Assuming a Gaussian shape, which is a good approximation in most NMR/ON experiments, the distribution of the resonance[4] around the center frequency $\nu_{\mathrm{res}}$ is given by

$$G(\nu) = f_{\mathrm{res}} \left( \frac{\ln 2}{\pi} \right)^{1/2} \exp \left[ - \ln 2 \frac{(\nu - \nu_{\mathrm{res}})^2}{\Gamma_0^2} \right], \tag{1.30}$$

where $\Gamma_0$ is the inhomogeneous linewidth and $f_{\mathrm{res}}$ is the fraction of nuclei which can be affected by the rf. The normalization is chosen in such a way that

$$\int G(\nu) d\nu = f_{\mathrm{res}} \tag{1.31}$$

is given. In the ideal case, $f_{\mathrm{res}} = 1$ is expected. To get a reasonable effect, the rf-field has to be frequency modulated. Assuming that all time-dependent effects can be neglected the observed resonance effect at a frequency $\nu$ is then given by

$$S_a(\nu) = \int_{\nu - \nu_m}^{\nu + \nu_m} G(\nu') d\nu', \tag{1.32}$$

where $\nu_m$ is the half of the modulation width, and $a$ stands for adiabatic approximation. If $\nu_m$ is small in comparison to $\Gamma_0$ the shape of $S_a(\nu)$ is approximately Gaussian again, the linewidth and the amplitude being dependent on the value of $\nu_m$. For a precise determination of $\nu_{\mathrm{res}}$, the half of the modulation width $\nu_m$ has to be chosen properly as a compromise between a large resonance effect and a small resonance linewidth.

When relaxation can not be neglected in observing the destruction of asymmetry in a NMR/ON signal one can not use a simple Gaussian-like form to fit the resonance curve. It is then more appropriate to use the following formula

[4] At resonance, rf induced transitions partially randomize the Boltzmann distribution, which is set up by the low temperature and the large hyperfine field for implanted radioactive nuclei in iron host. The randomization has a destructive effect on the angular distribution of the emitted $\beta(\gamma)$-rays, which can be detected by observing the count rate at a specific angle as a function of rf-frequency.

to fit the data (see e.g. Leuthold et al. (1980); Stone (1986))

$$S_n(\nu) = \int_{\nu-\nu_m}^{\nu+\nu_m} \frac{A}{a\sqrt{\pi}} \exp\left[-\left(\frac{\nu'-\nu_{\mathrm{res}}}{a}\right)^2\right] d\nu' + \left[\sum_{k=1}^{n} \exp\left[-\frac{(k-1)\tau}{T_1}\right] \times \right.$$
$$\left. \times \int_{\nu-\nu_m-k\Delta}^{\nu+\nu_m-k\Delta} \frac{A}{a\sqrt{\pi}} \exp\left[-\left(\frac{\nu'-\nu_{\mathrm{res}}}{a}\right)^2\right] d\nu' \right] \times \tag{1.33}$$
$$\times \frac{T_1}{\tau}\left(1 - \exp\left[-\frac{\tau}{T_1}\right]\right)$$

where $\tau$ is the measuring time at each frequency, $\Delta$ is the frequency step interval, $S_n(\nu)$ is the measured NMR signal. From the programming point of view, it is more easy to work with a modified version of Eq. 1.33. Indeed, using the definition of the "error function"

$$\frac{2}{\sqrt{\pi}} \int_0^z \mathrm{e}^{-\mathrm{t}^2}\,\mathrm{dt} \equiv \mathrm{erf}\,(z) \tag{1.34}$$

one can show that

$$\int_{\nu-\nu_m}^{\nu+\nu_m} \frac{A}{a\sqrt{\pi}} \exp\left[-\left(\frac{\nu'-\nu_{\mathrm{res}}}{a}\right)^2\right] d\nu' =$$
$$\frac{A}{2}\left\{\mathrm{erf}\left(\frac{\nu+\nu_m-\nu_{\mathrm{res}}}{a}\right) - \mathrm{erf}\left(\frac{\nu-\nu_m-\nu_{\mathrm{res}}}{a}\right)\right\} \tag{1.35}$$

such that the fitting formula Eq. 1.33 can be simplified.

Eq. 1.33 shows that an asymmetry of $S_n(\nu)$ is introduced, depending on the sweep direction. In the slow-sweep limit $\tau/T_1 \gg 1$, $S_n(\nu)$ reduces to the "adiabatic" case $S_a(\nu)$ (see Eq. 1.32). In the ultrafast limit $\tau/T_1 \ll 1$, the structure of $S_n(\nu)$ would be that of the error function. In this case all information on $T_1$ would be lost, too. If the relaxation time is comparable to the measuring time at each frequency $\tau/T_1 \approx 1$, the measured resonance effect $S_n(\nu)$ has an asymmetric shape, with an exponential decay in sweep direction. This causes a "tail" structure in the observed NMR signal (as an example of such a "tail"-structure in an NMR signal see i.e. Hagn et al. (1981); Herzog et al. (1989)). In other words, the maxima of the observed resonances are clearly shifted in sweep direction because of the finite spin-lattice relaxation time.

# Chapter 2

# GEANT4 simulations

## 2.1 Introduction

In the last two decades large-scale, accurate and comprehensive simulations of the detector set-ups used in experiments in modern particle and nuclear physics have gained significant importance. The GEANT4 code (see Agostinelliae et al. (2003)) is a new-generation toolkit for full and fast Monte Carlo simulations, intended for a wide range of applications. These include high energy physics, space and cosmic ray simulations, nuclear and radiation analysis, and medical applications. GEANT4 is based on the Object Oriented technology, has been developed using the C++ computer language, and provides the transparency of the physics implementation. The toolkit provides a diverse, wide-ranging and yet cohesive set of software components which can be employed in a variety of settings. These range from simple studies of basic phenomena and geometries to full-scale detector simulations.

In defining and implementing the software components, all aspects of the simulation process have been included:

- the geometry of the system,
- the materials involved,

- the fundamental particles of interest,
- the generation of the primary particles of events,
- the tracking of particles through materials and external electromagnetic fields,
- the physics processes governing particle interactions,
- the response of sensitive detector components,
- the generation of event data,
- the storage of events and tracks,
- the visualization of the detector and of particle trajectories,
- the capture for the subsequent analysis of simulation data at different levels of detail and refinement.

At the heart of this software system is an abundant set of physics models to handle the interactions of particles with matter across a very wide energy range. Data and expertise have been drawn from many sources around the world and in this respect GEANT4 acts as a repository that incorporates a large part of all that is known about particle interactions. Moreover, it continuous to be refined, expanded and developed.

## 2.2 Calculations of the solid angle correction factors $Q_\lambda$

In subsection 1.2.5 the importance of the solid angle corrections for $\beta$-particles was shown, especially in the presence of an external magnetic field that effects their trajectories. In addition various scattering effects also contribute to the $Q_\lambda$ correction factors. The GEANT4 toolkit allows us to take these corrections into account. Fig. 2.1 shows a modelled geometry that has been used in the GEANT4 simulations for the data presented here.

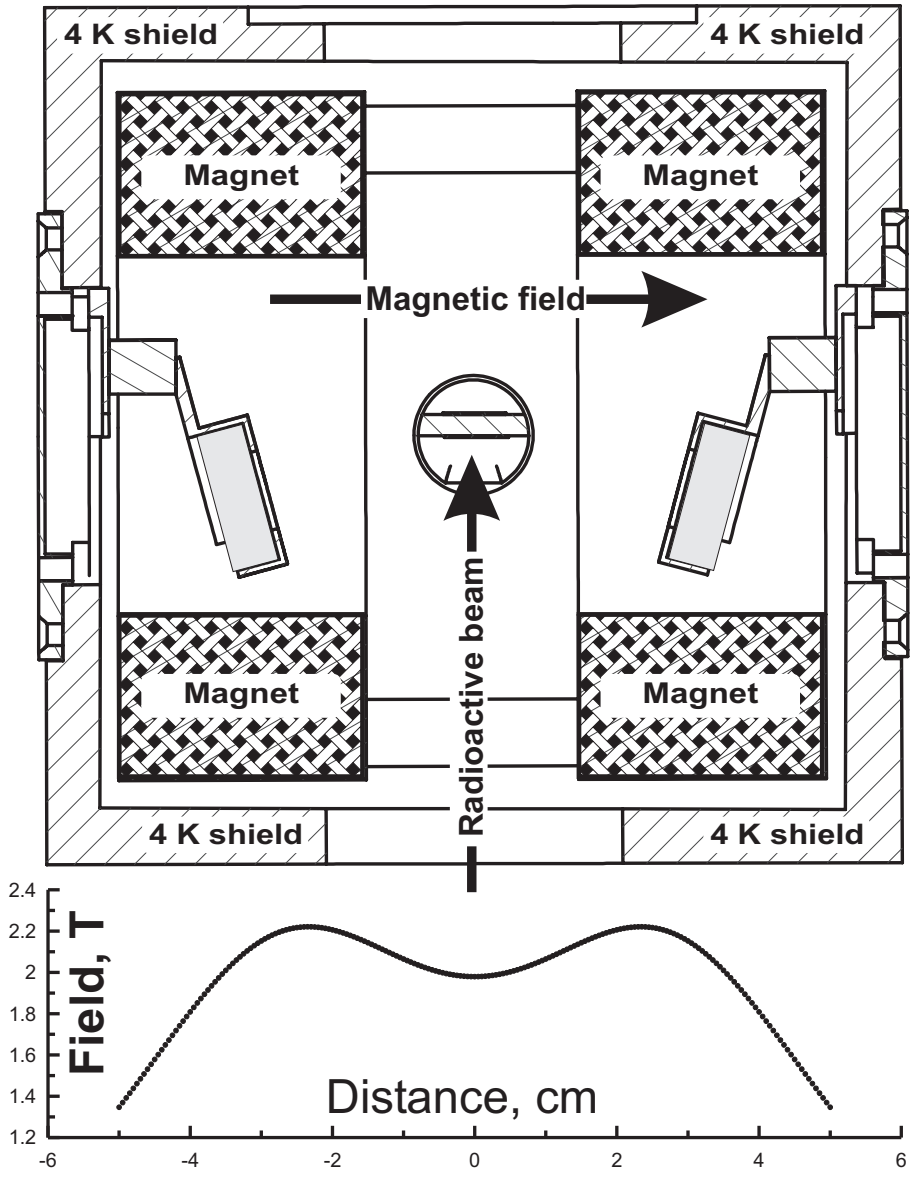


**Figure 2.1:** Horizontal cross-section of the lower part of the NICOLE refrigerator. Only the horizontal, i.e. "left" and "right" (15° and 165°) $\beta$-particle detectors are shown. The bottom detector is not shown to simplify the drawing. Also shown are the direction of the incident radioactive ion beam and the direction of the external magnetic field. The magnet coils are indicated by the cross hatched areas.

### 2.2.1 Model of the inner part of the NICOLE refrigerator

The inner part of the NICOLE refrigerator was modelled using the technical dimensions supplied by the manufacturer Oxford Instruments Ltd$^{TM}$ (see Fig. 2.1) as well as measured geometrical data obtained during experiment. The geometry of the set-up was easily described using a variety of geometrical elements available in GEANT4. $\beta$-detectors were simulated with a simple cylindrically shaped object made from germanium, although in reality they have more complicated geometry and material composition (see Zákoucký et al. (2004), Vénos et al. (2000) and Fig. 1.4(b)). In addition the detector holders were modelled in order to take these into account when simulating scattering processes of the particles on the inner parts of the refrigerator. Moreover, the inner part of the 4 K shield and 4 K flanges (holding the $\beta$-particles) as well as the superconducting magnet were modelled too. The inner structure of the magnet was not described in detail. It was modelled only as a cubic shape of stainless steel with holes for inserting a cold finger and particle detectors with their mountings. The thin plastic NMR coil was not taken into account. The positioning of the particle detectors relative to the cold finger and magnet was the same as in experiment. The accuracy with which the actual geometry was measured is typically $\pm 1$ mm.

The lower part of Fig. 2.1 shows the profile of the total magnetic field on the magnetic field axis which runs through the center of the particle detectors. The central magnetic field (i.e. in the center of the magnet and therefore at the place where the radioactive ions are implanted) in this case was 2 Tesla. In a real experiment the amplitude of the central external magnetic field is typically 0.1 Tesla. For this field however the axial and radial profile of the magnetic field are exactly the same but the amplitude of the field is to be adjusted according to the central value, which is usually measured by the current through the superconducting coils of the magnet. The precision of such measurement is typically of the order of less then 0.1 %. The axial and radial profile of the magnetic field were provided by the manufacturer with a resolution of 0.5 mm in radial and axial directions. The $\beta$-detectors are installed at about 30 mm from the center of the magnet. The detectors are installed off the magnetic field axis, at an angle of 15° with respect to the plane of the Fe foil to reduce the effect of scattering of the $\beta$-particles in the Fe foil. Although the magnetic field in the

magnet is not uniform, for our simulation we will assume a uniform distribution of the magnetic field inside the refrigerator. This is possible because the values of the magnetic field in the center of the magnet and at the position of the detectors differ only by about 6 % (see Fig. 2.1, lower part), which corresponds to an error of $\pm 3$ mm for the radius of curvature of about 47 mm for a $\beta$-particle with a typical energy of about 1 MeV (see Eq. 1.23 and Eq. 1.25). A few mm is also the typical accuracy of the position measurement of the particle detectors.

### 2.2.2 Monte Carlo simulation

In GEANT4, the following electro-magnetic processes are included: Compton scattering, photo-electric effect, Rayleigh effect, pair production, multiple scattering, annihilation, absorption, bremsstrahlung and ionization. For GEANT4 a new code for the electro-magnetic interactions of low energy particles has been developed (see Ivanchenko et al. (1999a,b); Giani et al. (1999); Apostolakis et al. (1999)) which extends the energy range downward to 250 eV. This enhancement is based on experimental data parameterizations using the following databases developed by the Lawrence Liwermore National Laboratory: EPDL97 (Evaluated Photon Data Library), EEDL (Evaluated Electron Data Library) and EADL (Evaluated Atomic Data Library). This low energy threshold, together with the physical processes available and the possibility to describe a magnetic field, allows us to use the GEANT4 for simulating the $Q$-factors in this work. In appendix A general formulas for the calculation of the $\beta$-spectrum are given.

The recorded information during simulations with GEANT4 are: position of emission, emission energy, momentum vector at emission, position when stopped, deposited energy in particle detectors, seed number of random generator, event number. This information allows one to determine the $Q$-factor for the NICOLE refrigerator. To obtain a reliable output the input parameters need to be accurate. It is a GEANT4 user's responsibility to provide an accurate geometrical description of the set-up, including the magnetic field (of course to the precision that the user would like to get reliable information).

Fig. 2.2 and Fig. 2.3 show the results of GEANT4 simulations. Here we show the distribution of the emission angles of $\beta$-particles detected in the 15°-degree

(Fig. 2.2) and 165° (Fig. 2.3) particle detectors. From these graphs it is clear that the $\beta$-particles emitted at certain angles have better chances to be detected, while for others, due to the screening effect there is no chance for being detected. The 'band' structure in the upper and lower parts of the figure is due to scattering on the surroundings parts of the set-up.

Other simulated results are shown in Fig. 2.4. Here the distribution of the deposited energy as a function of emitted energy is shown for the $\beta^+$-spectrum of $^{59}$Cu with endpoint energy of 3778 keV. For an *ideal* detector we would have only a diagonal line, with the deposited energy being equal to the emitted energy. However, in reality this is not the case, mostly due to scattering and due to the annihilation process. When an emitted positron is scattered on the surrounding materials and annihilates it creates two 511 keV $\gamma$-quanta that could be detected in a particle detector. Therefore we see a horizontal line around 511 keV. When the emitted positron is scattered inside the particle detector 511 keV $\gamma$-quanta can be created. Summing of the $\beta$-signal with this annihilation radiation included in the detector can occur, such that the deposited energy for a single event can exceed the endpoint energy. Again, this is a consequence of the not *ideal* detection of monoenergetic positrons. In other words, the distortion of the emitted $\beta^+$-spectra is due to backscattering, side-scattering and pileup of the $\beta$-particles with 511 keV $\gamma$-quants. To better understand the detection mechanism one could look at the beta-ray response function that is discussed in Rehfield and Moore (1978). Recently, a semi-empirical response function for positrons recorded with HPGe detectors was discussed in detail in Severijns et al. (2005).

In order to estimate the uncertainties associated to the calculated $Q$-factors, we made five independent ($m = 5$) Monte Carlo simulations (tracking each time around $10^6$ $\beta$ particles) for each radioactive isotope. The final calculated $Q$-factor is then given by the average of the calculated $Q_k$-factors for each simulation run for a particular isotope:

$$Q = \frac{1}{m}\sum_{k=1}^{m} Q_k \tag{2.1}$$

and an estimation of the variance of the $Q$-factor is given by the expression:

$$\sigma_Q^2 = \frac{1}{m-1}\sum_{k=1}^{m}(Q_k - Q)^2. \tag{2.2}$$

**Table 2.1:** $Q$-factor corrections calculated with GEANT4 for the 15° particle detector in eight energy bins in the $\beta$-spectrum of $^{59}$Cu, in the region from 1602 keV to 2847 keV.

| | $E$-energy, keV | | | | | | | |
|---|---|---|---|---|---|---|---|---|
| | $E_1$ | $E_2$ | $E_3$ | $E_4$ | $E_5$ | $E_6$ | $E_7$ | $E_8$ |
| | 1602-1758 | 1758-1914 | 1914-2069 | 2069-2225 | 2225-2381 | 2381-2566 | 2566-2692 | 2692-2847 |
| | $Q$-factors | | | | | | | |
| $m$ | $Q_{E_1}$ | $Q_{E_2}$ | $Q_{E_3}$ | $Q_{E_4}$ | $Q_{E_5}$ | $Q_{E_6}$ | $Q_{E_7}$ | $Q_{E_8}$ |
| 1 | 0.9267 | 0.9334 | 0.9410 | 0.9526 | 0.9600 | 0.9765 | 0.9872 | 0.9851 |
| 2 | 0.8827 | 0.9014 | 0.9258 | 0.9649 | 0.9692 | 0.9770 | 0.9796 | 0.9789 |
| 3 | 0.9158 | 0.9232 | 0.9521 | 0.9390 | 0.9671 | 0.9549 | 0.9730 | 0.9757 |
| 4 | 0.9278 | 0.9338 | 0.9434 | 0.9625 | 0.9381 | 0.9703 | 0.9648 | 0.9696 |
| 5 | 0.9013 | 0.9332 | 0.9264 | 0.9564 | 0.9661 | 0.9819 | 0.9622 | 0.9782 |
| $\overline{Q}$ | 0.9109 | 0.9250 | 0.9377 | 0.9551 | 0.9601 | 0.9728 | 0.9734 | 0.9815 |
| $\Delta\overline{Q}$ | 0.0190 | 0.0139 | 0.0114 | 0.0102 | 0.0128 | 0.0105 | 0.0103 | 0.0057 |

Tables 2.1 and 2.2 list the $Q$-factors calculated with GEANT4 for a few energy bins for $^{59}$Cu in the region from 1602 keV to 2847 keV for two particle detectors at opposite sides of the sample (i.e. 15° and 165°). In this calculation we assumed only positrons coming from the most important branch in the $\beta^+$-decay of the ground state of $^{59}$Cu to the ground state of $^{59}$Ni, with endpoint energy 3778 keV. We neglected other branches in the $\beta$-spectra (see Fig. 3.1). The $\beta$-particles were uniformly distributed from a distance of 200 Å inside the Fe foil, corresponding to the implantation energy of 60 keV, up to the foil surface. Taking into account the lead collimator inside the access part of the NICOLE refrigerator, the simulated spot from where the $\beta$-particles appear has a radius of about 2.5 mm.

In Chapter 1 it was shown that the solid angle corrections can be calculated (with some assumptions) using Eq. 1.21 and Eq. 1.22. For the geometry that we use in the GEANT4 calculations one can then estimate the solid angle corrections due to the finite size of source and detector to be $Q_1 = 0.9693 \pm 0.0029$, where the error is due to the uncertainty in the measured angles. Comparing this value with the values obtained from the GEANT4 calculations we see that this estimation could be used as a first order approximation of the solid angle correction for a *rough* analysis. However, for a more precise analysis the

**Table 2.2:** $Q$-factor corrections calculated with GEANT4 for the 165° particle detector in eight energy bins in the $\beta$-spectraum of $^{59}$Cu, in the region from 1602 keV to 2847 keV.

| | $Q$-factors | | | | | | | |
|---|---|---|---|---|---|---|---|---|
| $m$ | $Q_{E_1}$ | $Q_{E_2}$ | $Q_{E_3}$ | $Q_{E_4}$ | $Q_{E_5}$ | $Q_{E_6}$ | $Q_{E_7}$ | $Q_{E_8}$ |
| 1 | 0.9178 | 0.9337 | 0.9476 | 0.9654 | 0.9653 | 0.9774 | 0.9882 | 0.9893 |
| 2 | 0.9200 | 0.9310 | 0.9380 | 0.9529 | 0.9602 | 0.9863 | 0.9855 | 0.9948 |
| 3 | 0.9015 | 0.9484 | 0.9677 | 0.9800 | 0.9803 | 0.9820 | 0.9760 | 0.9982 |
| 4 | 0.9153 | 0.9545 | 0.9134 | 0.9624 | 0.9588 | 0.9721 | 0.9541 | 0.9916 |
| 5 | 0.9169 | 0.9501 | 0.9613 | 0.9808 | 0.9713 | 0.9656 | 0.9849 | 0.9887 |
| $\overline{Q}$ | 0.9143 | 0.9435 | 0.9456 | 0.9683 | 0.9672 | 0.9767 | 0.9777 | 0.9925 |
| $\Delta\overline{Q}$ | 0.0074 | 0.0105 | 0.0214 | 0.0120 | 0.0088 | 0.0081 | 0.0140 | 0.0040 |

GEANT4 calculations are needed.

On the other hand, one could average the $Q$-factor values calculated with GEANT4 over the whole energy region, thus cancelling out the dependence on the energy due to scattering, the magnetic field and so on. This leads to the value of $Q = 0.9564 \pm 0.0246$ (assuming it is the same for both particle detectors, i.e. for the 15° and 165°), which is within the error in agreement with the value above that was calculated using Eq. 1.21 and Eq. 1.22.

## 2.3 Conclusion and Outlook

GEANT4 can be used to calculate the solid angle correction factors $Q_\lambda$. The results are in a good agreement with the results obtained with approximated formulas (see Eq. 1.21 and Eq. 1.22). However, more reliable results are obtained since GEANT4 takes into account scattering processes as well as the effects of the magnetic field.

Because of the importance of scattering of the $\beta$-particles on the surrounding materials, it would be interesting to add in the model an NMR coil, which is sitting most closely to the cold finger. In addition, we did not include in our model the thin layer of solder between the cold finger and the Fe foil. Since, this contains a large amount of tin it will also affect scattering processes.

The next step would now be to test the dependence of the solid angle corrections on the form and diameter of the sample spot (in our case it was a simple circle). In addition, in our calculations we assumed that the implanted ions are sitting exactly in the center of the magnet, however during the experiment some of the values of electrostatic settings of the beam controls could drift with time, and, therefore the spot could drift from the center of the magnet. It would be interesting to investigate the effect of this on the solid angle corrections too.

Besides of the geometrical effects that could influence the solid angle corrections, a good knowledge of the material composition of the detectors is also important for the $Q$-factor calculations. Hurtado et al. (2004) showed how important it is to know the manufacturing details of the germanium crystals used for the detection of the radiation. In particular, the composition of the p+ and n+ contacts and the presence of contaminating elements in the pure germanium (i.e. boron and lithium) is important.

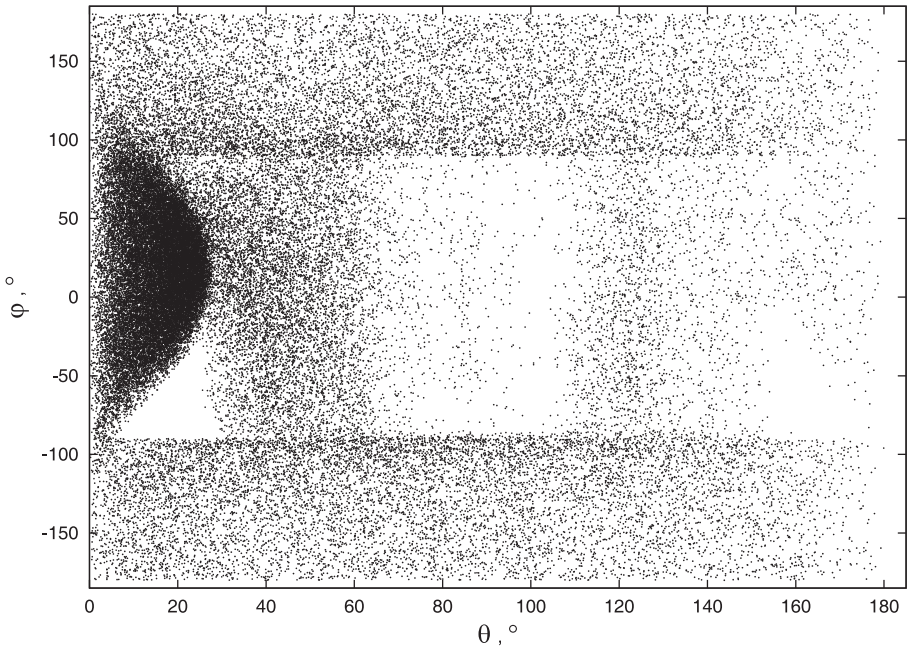


**Figure 2.2:** Distribution of the emission angles of $\beta$-particles detected in the 15°-degree particle detector. It is clear that $\beta$-particles emitted in a certain direction have a better chance to be detected.

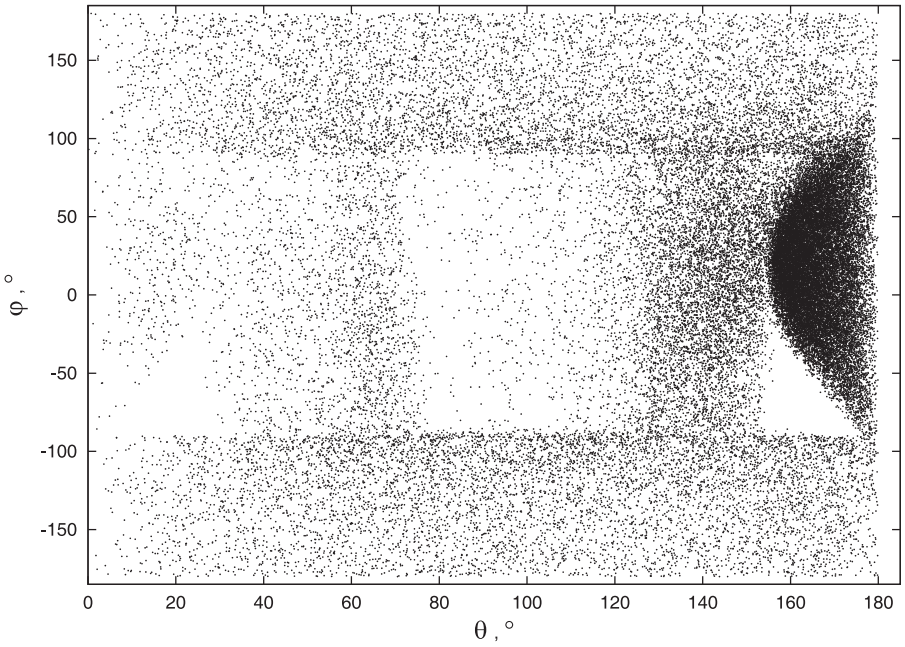


**Figure 2.3:** Distribution of the emission angles of $\beta$-particles detected in the 165°-degree particle detector.

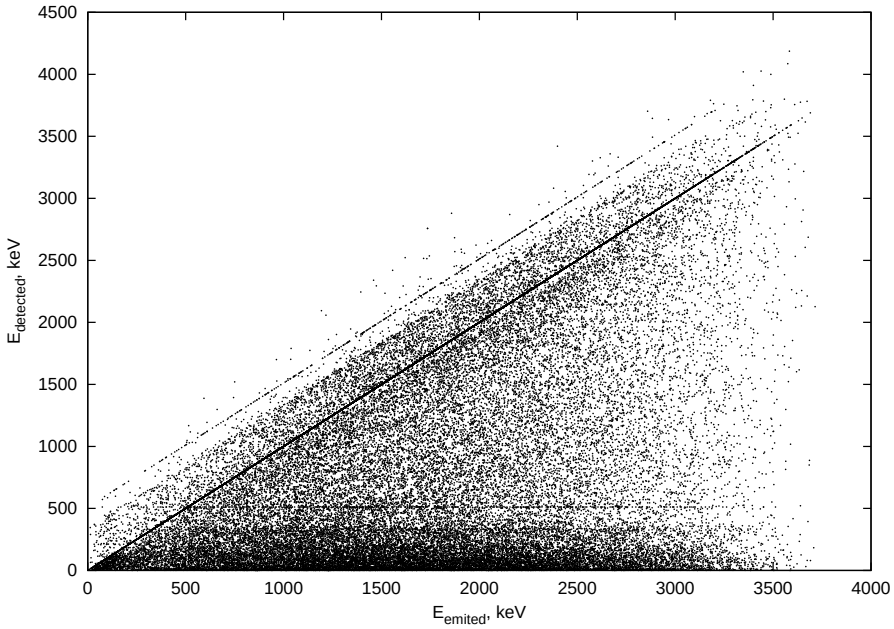


**Figure 2.4:** Deposited (i.e. detected) energy as a function of emitted energy. For an *ideal* detector we would have $E_{emitted} = E_{deposited}$, however due to scattering and annihilation the deposited energy is not always exactly equal to the emitted energy. The horizontal line around 511 keV represent cases when the emitted positron was scattered somewhere on the magnet surrounding, and due to annihilation created 511 keV $\gamma$-quanta that have been detected in the particle detector. The cases when the deposited energy exceeds the emitted energy represent detection of positrons inside the particle detector with creation of the 511 kev $\gamma$-quanta.

# Chapter 3

# Nuclear Magnetic Moment of $^{59}$Cu

## 3.1 Introduction

Close to neutron and proton shell closures the structure of odd-A nuclei may be well approximated by the single-particle behavior of the particle (hole) outside (inside) the closed shell. The most basic single-particle shell model then predicts the so-called Schmidt values for the nuclear magnetic dipole moments. It is well known that for nuclei farther away from closed shells the magnetic moment differs from the Schmidt value (Bohr and Mottelson (1998)). These deviations are caused by configuration mixing (Core Polarization) and meson exchange currents (MEC) (Towner (1987)). The first is related to the fact that the wavefunctions of the basic shell model assume that the odd nucleon is in a single particle state, while even small configuration admixtures can already appreciably change the magnetic moment. The second correction takes into account the effects of interaction with the electromagnetic field when two nucleons are interacting.

In case of the odd-A Cu isotopes the $29^{th}$ proton is in the $p_{3/2}$ orbital with a Schmidt moment $\mu_{\text{Schmidt}} = 3.79\mu_N$. Below $N = 40$, the neutrons occupy

the $p_{3/2}$, $f_{5/2}$ and $p_{1/2}$ orbitals. Recently, the development of the RILIS resonance ionization laser ion source (Kudryavtsev et al. (1996); Köster et al. (2000); Fedosseev et al. (2003)) has allowed the measurement of several new magnetic moments for copper isotopes (Rikovska et al. (2000); Rikovska and Stone (2000); Weissman et al. (2002)) with the ISOLDE facility at CERN . With experimental magnetic moments being available for the odd-A isotopes from $^{61}$Cu up to $^{69}$Cu one can now investigate the neutron number dependence of the moments of the odd-A Cu nuclei below $N = 40$ and especially towards the $N = 28$ shell closure at $^{57}$Cu. In this respect the magnetic moment of $^{59}$Cu, with 30 neutrons, is of special interest as it paves the way for the measurement of the moment of the $N = 28$ isotope $^{57}$Cu ($^{56}$Ni core plus one proton) and at the same time indicates how the systematic trend of odd-Cu moments develops as $N = 28$ is approached.

We have therefore measured the magnetic moment of $^{59}$Cu at the ISOLDE facility (Golovko et al. (2004)). In addition, shell model calculations were performed using perturbation theory to correct for core polarization and meson exchange currents. Finally, since $^{59}$Cu is the mirror nucleus of $^{59}$Zn, the decay of which is known, our result can also be compared to the value predicted from the correlation between ground state gyromagnetic ratios and superallowed $\beta$-decay transition strengths of mirror nuclei that was established by Buck and Merchant (2001).

## 3.2 Experiment

The magnetic moment of $^{59}$Cu was measured with the LTNO technique combined with Nuclear Magnetic Resonance on Oriented Nuclei where the destruction of the $\beta$-asymmetry by the radio frequency signal ($\beta$-NMR/ON) was observed with particle detectors operating at a temperature of about 10 K inside the NICOLE $^3$He-$^4$He dilution refrigerator. The combination of these techniques has several advantages for measuring nuclear magnetic moments. Firstly, beta asymmetries are significantly larger then gamma asymmetries at relatively small values of $\mu B/T$, with $T$ the sample temperature. Therefore, with $\beta$-detection, even for isotopes with rather small magnetic moments a measurable resonance signal can be obtained at the temperatures accessible with an

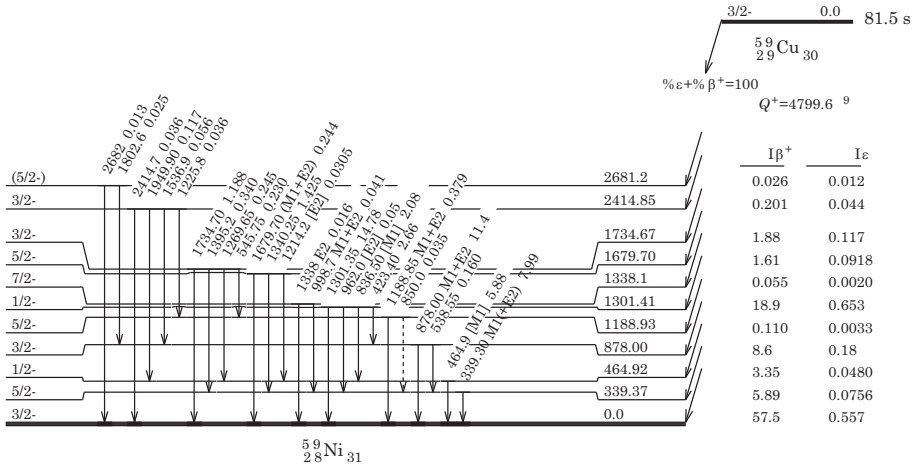


**Figure 3.1:** Partial scheme of low lying levels in $^{59}$Ni populated in the $EC/\beta^+$-decay of $^{59}$Cu (adopted from Firestone (1996); Andreoiu et al. (2002)). The strongest $\beta^+$-branch of $^{59}$Cu is an allowed $I^\pi = 3/2^- \rightarrow I^\pi = 3/2^-$ ground state to ground state Gamow-Teller transition with endpoint energy $E_0 = 3778$ keV and an intensity of 57.5 %. The rest of the $\beta^+$-intensity is spread over at least ten other branches.

on-line refrigerator. Secondly, since one can in principle integrate the complete beta spectrum the energy resolution of the beta detectors is less important. Furthermore, in this experiment the particle detectors were placed inside the 4 K radiation shield of the dilution refrigerator, thereby minimizing scattering or absorption of the $\beta$-particles on their way to the detectors.

Detailed information on the $EC/\beta^+$-decay of $^{59}$Cu ($t_{1/2} = 81.5$ s, $I^\pi = 3/2^-$) can be found in Firestone (1996); Andreoiu et al. (2002). The strongest $\beta^+$-branch of $^{59}$Cu is an allowed $I^\pi = 3/2^- \rightarrow I^\pi = 3/2^-$ ground state to ground state Gamow-Teller transition with endpoint energy $E_0 = 3778$ keV and an intensity of 57.5%. The rest of the $\beta^+$-intensity is spread over at least ten other branches. Fig. 3.1 shows the partial decay scheme for $^{59}$Cu.

The magnitude of the hyperfine magnetic field of Cu in an iron host lattice is known, but unfortunately not with very high precision: $B_{\mathrm{hf}} = -21.8(1)$ T (Khoi et al. (1975)). In fact, the error of the hyperfine magnetic field will turn out to give the largest contribution to the total error of the nuclear magnetic

moment of $^{59}$Cu, as will become clear later.

The radioactive $^{59}$Cu was produced at ISOLDE (CERN) with a 1.4 GeV proton beam from the Proton Synchrotron Booster, bombarding a $ZrO_2$ felt target (6.3 g Zr/cm$^2$) (Köster et al. (2003)) connected to the RILIS (Köster et al. (2000); Weissman et al. (2002); Fedosseev et al. (2003)) which provided the required element selectivity for the separation of $^{59}$Cu. After ionization and acceleration to 60 keV, the $^{59}$Cu beam with an intensity of about $3 \times 10^6$ ions/s was mass-separated by the General Purpose Separator, transported through the beam distribution system, and implanted into a polished and annealed 99.99% pure Fe foil (thickness 250 $\mu$m) that was soldered onto the cold finger of the NICOLE $^3$He-$^4$He dilution refrigerator. The implantation depth of the $^{59}$Cu-ions is around 200 Å. The corresponding energy loss for the $\beta$-particles leaving the sample is then of the order of 100 eV, which is negligible in comparison to the $\beta$-endpoint energy of $^{59}$Cu. The iron foil in which the radioactive $^{59}$Cu ions were implanted was magnetized by an external magnetic field generated by a superconducting split-coil magnet. During the measurements a horizontal external magnetic field $B_{\text{ext}} = 0.10(2)$ T, produced by the superconducting magnet, was used. Firstly, a field of 0.5 T was applied, in order to magnetically saturate the iron foil. Thereafter, the field was reduced to 0.1 T so as to minimize its influence on the trajectories of the $\beta$-particles. For the 250 $\mu$m thick Fe foil that was used a demagnetization field $B_{\text{dem}} = 0.025(5)$ T (see section 1.4) was calculated. The temperature of the sample was maintained in the region between 10 and 100 mK and measured by a $^{57}$Co<u>Fe</u> nuclear orientation thermometer.

The angular distribution of the positrons emitted during the $\beta^+$-decay of $^{59}$Cu was observed with three high purity Ge (HPGe) particle detectors that were installed inside the 4 K thermal shield of the dilution refrigerator. These detectors with a sensitive diameter of about 12 mm and a thickness of 5 mm were positioned at angles of 15°, 75° and 165° with respect to the orientation axis defined by the magnetization of the iron foil in the external magnetic field. The thickness of the detectors was chosen such that the endpoint of the $\beta$ spectrum could be observed with maximal efficiency while at the same time minimizing the sensitivity to $\gamma$-rays. Installing these detectors inside the thermal shields means that they have to be able to operate at temperatures close to the tem-

perature of liquid He (i.e. around 10 K). The detectors used were produced and tested in the Nuclear Physics Institute in Řež (Vénos et al. (2000); Zákoucký et al. (2004)). Apart from these particle detectors large-volume HPGe detectors for detection of the $\gamma$ radiation were installed outside the refrigerator. The data were corrected for the "dead-time" of the data acquisition system using a precision pulse generator.

## 3.3 Data collection and Analysis

In order to reduce the search region for the $\beta$-NMR/ON measurement, the $^{59}$Cu magnetic moment was first determined by scanning the first of the two lasers used to selectively ionize Cu atoms in the RILIS ion source. The on-line analysis of this measurement yielded $|\mu[^{59}\mathrm{Cu}]| = 1.90(7)$, corresponding to a resonance frequency $\nu_{res} = 209 \pm 8$ MHz, which determined the search region for the $\beta$-NMR/ON experiment. In the $\beta$-NMR/ON measurement about 200 spectra of 150 s each were recorded. The rf-signal was generated by a Marconi generator with a range from 10 kHz to 3.3 GHz. The rf-power level was tuned in order to see its effect on the sublevel populations through a small but clear change in the $\beta$-anisotropy[1]. This anisotropy was defined as the double ratio of the 15° and 165° $\beta$-detector count rates $N(\theta)$ at millikelvin temperatures (polarized sample) and at 1 K (unpolarized sample) [see also section 1.2]:

$$\frac{W_\beta(15°)}{W_\beta(165°)} = \left[\frac{N(15°)}{N(165°)}\right]_{mK} / \left[\frac{N(15°)}{N(165°)}\right]_{1K} \tag{3.1}$$

The resonance experiment was performed at a sample temperature of about 10 mK. Since in a $\beta$-NMR/ON experiment one is observing just the destruction of asymmetry in the angular distribution of the beta particles we used the complete energy region from 550 keV to 3778 keV in order to increase statistics (Fig. 3.2). The energy region below 550 keV was not used as it suffered from background of Compton scattered 511 keV gamma rays.

[1] First, the maximum polarization of the implanted nuclei in on-line condition was achieved by cooling the sample till 10 mK (so-called "base temperature"). Then the rf-power level was applied to see the sample temperature rice by a few mK. This rf-power level was kept during the whole NMR/ON experiment.

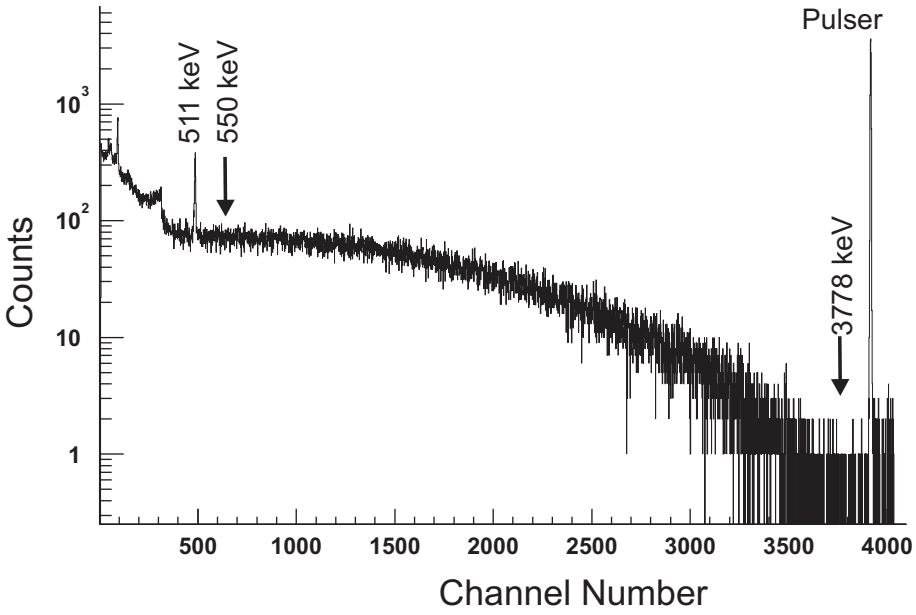


**Figure 3.2:** Typical $\beta$-spectrum for $^{59}$Cu recorded within one 150 s measurement cycle. The 511 keV positron annihilation line and the pulser peak are indicated. For the $\beta$-NMR/ON experiment discussed here the spectrum was integrated between 550 keV and 3778 keV (endpoint).

The NMR/ON measurements were performed at a sample temperature of about 10 mK, corresponding to a $\beta$-anisotropy effect $R = 1 - [W_\beta(15°)/W_\beta(165°)]$ of about 14 %.

At first the frequency was varied from 200 to 220 MHz, both in upward and in downward directions, in 1 MHz steps with 1 MHz modulation amplitude and 0.1 kHz modulation frequency, and sent to the NMR coil that was installed around the sample. In these two scans a clear resonance signal was immediately found. Statistics was subsequently improved by three frequency sweeps in upward direction and two sweeps downwards in the region from 203 to 213 MHz. In addition a scan was carried out in the frequency region from 204 to 215 MHz in 0.5 MHz steps with 0.5 MHz modulation amplitude and 0.1 kHz modulation frequency.

All scans were separately analyzed in order to check for possible systematic

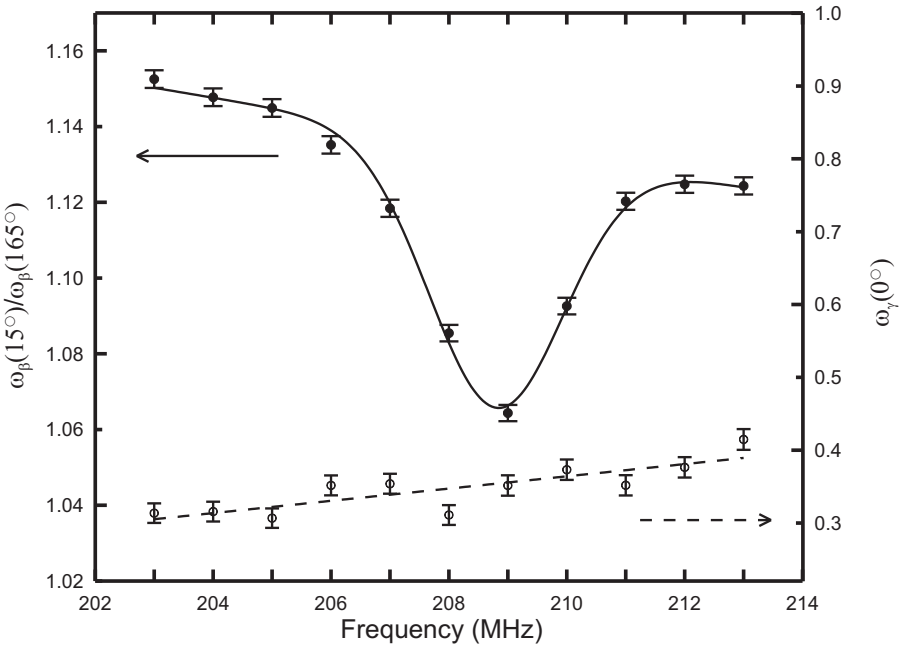


**Figure 3.3:** On-line nuclear magnetic resonance on oriented nuclei curve for $^{59}$Cu (sum of five scans: three in upward and two in downward direction). Plotted is the ratio of the pulser normalized count rates for the 15° (L) and 165° (R) $\beta$-particle detectors as a function of rf-frequency. The integrated destruction of anisotropy is 46 %. At the bottom the anisotropy at 0° for the 136 keV $\gamma$-ray of the $^{57}$Co<u>Fe</u> thermometer ($W_\gamma(0°)$, corresponding to a sample temperature of about 10 mK) is displayed for the same frequency region, showing no resonant effect at the position of the $^{59}$Cu resonance. The slope in the anisotropy versus frequency that is visible for both isotopes is caused by a small heating due to an increase in the power absorption by the system with increasing *rf* frequency. The amplitude of the signal observed by the pick-up coil that was installed around the sample holder indeed increased from 49 mV at 200 MHz to 95 mV at 210 MHz and 210 mV at 220 MHz.

**Table 3.1:** Overview of the frequency ($\nu$) scans for $^{59}$Cu.

| scan | $\nu$, MHz | step, MHz | $\nu_{\rm res}$, MHz |
|---|---|---|---|
| 1 | 200→220 | 1.0 | 208.71 ± 0.08 |
| 2 | 220→200 | 1.0 | 208.57 ± 0.09 |
| 3 | 203→213 | 1.0 | 208.84 ± 0.09 |
| 4 | 213→203 | 1.0 | 208.49 ± 0.13 |
| 5 | 203→213 | 1.0 | 208.73 ± 0.08 |
| 6 | 213→203 | 1.0 | 208.90 ± 0.07 |
| 7 | 203→213 | 1.0 | 208.85 ± 0.07 |
| 8 | 204→215 | 0.5 | 208.86 ± 0.06 |
| weighted average | | | 208.79 ± 0.03 |

errors. No hints for such errors were found. An evaluation of all available data with due regard to relaxation effects gave for the center frequency the final result $\nu = 208.79(4)$ MHz. To illustrate the quality of the data the resonance curve obtained after summing all scans in the frequency region from 203 to 213 MHz in 1 MHz steps is shown in Fig. 3.3. The data points were fitted with a straight line in addition to the resonance function to account for the slope in the on-line data. From the resonance frequency, the spin ($I$) of the ground state of $^{59}$Cu , the Plank constant $h$, and the total magnetic field ($\mathbf{B}_{\rm tot} = \mathbf{B}_{\rm hf} + \mathbf{B}_{\rm ext} - \mathbf{B}_{\rm dem}$), the nuclear magnetic moment of $^{59}$Cu is obtained as:

$$\mu = \left| \frac{I\,\nu_{\rm res}\,h}{B_{\rm tot}} \right| \tag{3.2}$$

yielding

$$\mu[^{59}\mathrm{Cu}] = +1.891(9)\mu_N \tag{3.3}$$

where most of the error is due to the uncertainty of the hyperfine field. The center frequency at hyperfine field value is $\nu(B_{ext} = 0) = 209.51(22)$ MHz. The sign of $\mu$ was obtained from the observed $\beta$-asymmetry and agrees with the systematics for the odd-A $p_{3/2}$ copper isotopes. The difference between our experimental result and the Schmidt value is $\Delta\mu(^{59}\mathrm{Cu})$ = -1.90(1).

## 3.4 Shell-model results with perturbation theory

Full details about the shell-model calculations that were performed to interpret our experimental result are given in Golovko et al. (2004). Here we would like to give a small overview of these.

The copper-isotopes ground-state wave functions are characterized by having 28 protons occupying closed-shell orbitals and the $29th$ proton occupying the $\pi p_{3/2}$ orbital. Explicit calculations were made for the magnetic moments of $^{57}$Cu and $^{69}$Cu. In the first case, the neutron number is $N = 28$; in the second it is $N = 40$. In both these instances the neutrons also may be considered to be occupying closed-shell orbitals. Thus for $^{57}$Cu and $^{69}$Cu the zeroth-order approximation in the model calculations is to write the ground-state wave function as that of fully occupied closed shells plus a single proton in the $\pi p_{3/2}$ orbital. This zeroth approximation is then corrected in perturbation theory. In these calculations contributions from core polarization, meson exchange, $\delta$-isobar excitations as well as relativistic effects were included.

For the $p_{3/2}$ proton in $^{69}$Cu, the calculated correction to the single-particle magnetic moment (i.e. $\mu_{\text{Schmidt}} = 3.79\ \mu_N$) is $\Delta\mu(^{69}\text{Cu}) = -0.91\ \mu_N$ in good agreement with the experimental value of $-0.95(1)\ \mu_N$ (Rikovska et al. (2000)). For $^{57}$Cu, the calculated correction is $\Delta\mu(^{57}\text{Cu}) = -1.39\ \mu_N$. There is no experimental measurement for $^{57}$Cu, but it is clear from Fig. 3.4 that any reasonable extrapolation from the known data on the odd-mass copper isotopes will produce a result significantly different from this calculated value.

The isotope $^{59}$Cu has two valence neutrons outside the $N = 28$ closed shells as well as the $p_{3/2}$ proton. So we have to estimate the impact of these two extra valence neutrons on the calculation of the magnetic moment. The difference between the calculations for $^{57}$Cu (with $N = 28$) and $^{69}$Cu (with $N = 40$) is that in $^{57}$Cu the neutron orbits $1p_{3/2}$, $0f_{5/2}$, $1p_{1/2}$ are empty, while at $^{69}$Cu they are taken to be full. This impacts on the calculation of the core-polarization and meson-exchange corrections in that these neutron orbits are part of the sum over particle orbits for $^{57}$Cu, but part of the sum over hole orbits for $^{69}$Cu. This effect alone is responsible for most of the difference between $\Delta\mu(^{57}\text{Cu})$

**Table 3.2:** Experimental and theoretically calculated magnetic moments (in units of nuclear magneton $\mu_N$) for odd-A copper-isotopes in the $N \approx Z$ region.

| A | N | $\mu^1_{\text{th}}$ | $\mu^2_{\text{mir}}$ | $\mu_{\text{fit}}$ | $\mu^3_{\text{exp}}$ |
|---|---|---|---|---|---|
| 57 | 28 | 2.40 | 2.49(3) | | |
| 59 | 30 | 2.48 | 2.24(11) | 1.91[4] | +1.891(9)[5] |
| 61 | 32 | | | | +2.14(4) |
| 63 | 34 | | | | +2.22329(18)<br>2.2272057(31)<br>2.2273456(14) |
| 65 | 36 | | | | +2.38167(25)<br>2.38161(19) |
| 67 | 38 | | | | +2.54(2)[6] |
| 69 | 40 | 2.87 | | | +2.84(1)[7] |

[1] Theoretical predictions from the shell-model; see Sec. 3.4.
[2] Predictions from systematics of mirror nuclei Buck and Merchant (2001)
[3] From the Table of Nuclear Moments Raghavan (1989)
[4] Extrapolation based on a straight line fit to the experimental data for $^{61-69}$Cu
[5] This work
[6] From ref. Rikovska and Stone (2000)
[7] From ref. Rikovska et al. (2000)

and $\Delta\mu(^{69}\text{Cu})$. If we make the reasonable assumption that the contribution of these neutron orbitals for the odd-mass copper isotopes lying between these two extremes is proportional to the neutron population, then we can get an estimate for the change $\Delta\mu(^{59}\text{Cu})$ of the magnetic moment with respect to the Schmidt value as

$$\begin{aligned} \Delta\mu(^{59}\text{Cu}) &= \Delta\mu(^{57}\text{Cu}) + \tfrac{2}{12}\left(\Delta\mu(^{69}\text{Cu}) - \Delta\mu(^{57}\text{Cu})\right) \\ &= -1.31\ \mu_N, \end{aligned} \tag{3.4}$$

corresponding to $\mu_{th}(^{59}\text{Cu}) = 2.48\ \mu_N$.

## 3.5 Discussion and conclusion

Table 3.2 and Fig. 3.4 summarize all presently available experimental magnetic moments for the odd-A copper isotopes, as well as the results from the shell model calculations described in the previous section and predictions for the

moments of $^{57,59}$Cu deduced from the correlation between the ground state gyromagnetic ratios and superallowed $\beta$-decay transition strengths of the mirror nuclei established by Buck and Merchant (2001). Also listed is the extrapolated value obtained from fitting a straight line to the available experimental data for $^{61-69}$Cu.

The estimate $\mu(^{59}\mathrm{Cu}) = 2.48\ \mu_N$ that is obtained from the shell model calculations stands at considerable distance from the experimental value of $+1.891(9)\ \mu_N$. It is doubtful, however, that a shell-model calculation based on a $N = 28$ closed-shells core will produce a result significantly different from Eqn. 3.4. The real problem is that the calculated magnetic moment in the closed-shell-plus-one nucleus $^{57}$Cu stands so far from the extrapolation of known data on odd-mass copper isotopes shown in Fig. 3.4. Indeed, fitting a straight line through the experimental magnetic moment values for the $3/2^-$ odd-mass $^{61}$Cu to $^{69}$Cu isotopes yields $\mu(^{59}\mathrm{Cu}) = +1.91\ \mu_N$.

In the calculation described in the previous section, it is implicitly assumed that $^{56}$Ni is principally a doubly closed-shell nucleus and any departure from this can be estimated in perturbation theory. In this scheme, the breaking of the closed shells is quite modest. On the other hand, there is significant evidence mainly from large-scale shell-model calculations (Otsuka et al. (1998); Honma et al. (2002); Lisetskiy et al. (2003)) that there is a massive amount of shell breaking at $^{56}$Ni. If this is the case, then the starting hypothesis of our calculations is poor, and hence the poor result in the comparison of theory with experiment for the $^{59}$Cu magnetic moment. Indeed, we could reverse this argument saying the measured magnetic moment for $^{59}$Cu provides further evidence of the massive shell-breaking at $^{56}$Ni. Further, since the measured and calculated magnetic moments for $^{69}$Cu are in good agreement with each other, one could even argue that $^{68}$Ni, with N=40, is a better doubly-magic closed-shell nucleus than $^{56}$Ni. In view of this a measurement of the magnetic moment of the "closed-shell-plus-one" nucleus $^{57}$Cu now becomes even more important. Such a measurement is actually being planned (Mertzimekis et al. (2002)).

Finally, our result can also be compared to the prediction which Buck and Merchant (2001) recently obtained from the linear relation they deduced between the ground state $g$-factors and the superallowed $\beta$-decay strength of mirror

nuclei

$$\mu_{mir}(^{59}Cu) = 2.24(11)\mu_N \tag{3.5}$$

Clearly, this prediction is not in very good agreement with the experimental value either. It is based on the experimental $\log ft$=3.69(2) for the mirror isotope $^{59}$Zn. Inserting our experimental value for the magnetic moment of $^{59}$Cu in the relations deduced by Buck and Merchant (2001) yields $\log ft(^{59}\text{Zn})$=3.75(1), which differs slightly from the experimental value, and in addition provides a new prediction for the magnetic moment of the mirror isotope $^{59}$Zn, i.e. $\mu_{mir}(^{59}Zn) = -0.28(2)\mu_N$.

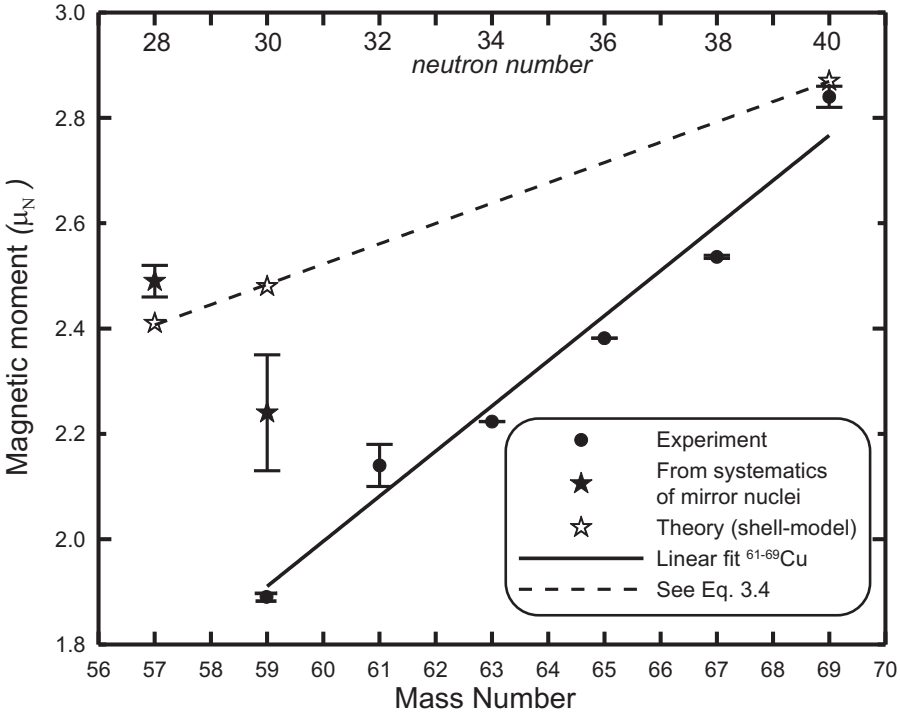


**Figure 3.4:** Experimental magnetic moments for the odd-A $^{59-69}$Cu isotopes (*black dots*) (Refs. Raghavan (1989); Rikovska et al. (2000); Rikovska and Stone (2000) and this work), shell model predictions for $^{57,59}$Cu (*open stars*) (see section 3.4) and predictions for $^{57,59}$Cu based on systematics of the mirror nuclei Buck and Merchant (2001) (*black stars*). The prediction for $^{59}$Cu from a linear fit (*full line*) to the experimental values for $^{61-69}$Cu is shown as well.

# Chapter 4

# Nuclear Magnetic Moment of $^{69}$As

## 4.1 Introduction

The region of nuclei with $A = 70 - 80$ is known as a region with a large diversity of nuclear shapes, ranging from almost purely spherical to extremely deformed. As a whole, the structure of this region is more complex than that of higher mass regions: whereas e.g. the deformation of heavier nuclei changes only slowly when more particles are added, very drastic shape changes are sometimes observed in the $A = 70 - 80$ region when only one or two particles are added.

Shape coexistence in this region was first observed in $^{72}$Se (Ramayya et al. (1975); Hamilton et al. (1974)), which has an almost spherical ground state and a strongly deformed first excited $0^+$ state (at 937 keV, i.e. only 75 keV above the first excited $2^+$ state!). The coexistence of a nearly spherical ground state and a deformed $0_2^+$ state was also reported for $^{74}$Se as well as for several neutron deficient Ge isotopes (e.g. Halbert et al. (1976), Ronningen et al. (1976), Kumar (1978)). The results that were obtained for the Ge isotopes from transfer reactions (see Rotbard et al. (1984) and references therein) and

Coulomb excitation experiments (Lecomte et al. (1980)), could be explained by assuming that not only a shape transition from spherical oblate to spherical prolate takes places between $N = 38$ and $N = 40$ ($^{70}$Ge, $^{72}$Ge), but that moreover also a shape transition from spherical to deformed (with prolate character) takes place between $N = 40$ and $N = 42$ ($^{72}$Ge, $^{74}$Ge).

Later, the other type of shape coexistence, i.e. with a deformed ground state and a spherical $0_2^+$ state was found in the krypton isotopes $^{74}$Kr (Becker et al. (1999)) and $^{76}$Kr (Piercey et al. (1981)).This observation provided the first evidence for large ground state deformations in the region of nuclei with $A = 70$. Almost simultaneously, theoretical ca1culations (Möller and Nix (1981); Möller et al. (1995)) also indicated the existence of large deformations for nuclei with $N = Z = 38$. These were then observed for $^{78}$Sr and $^{80}$Sr (Lister et al. (1982)). The very light Sr isotopes even turned out to be among the most deformed nuclei that were known until then. For the odd-$A$ isotopes in this $A = 70 - 80$ region, experimental studies yielded large prolate deformations for the very light ($N < 41$) Sr and Kr isotopes, while for the somewhat heavier nuclei (with $N = 43$ and 45), oblate and triaxial shapes are present as well. Recently, clear evidence for shape isomers was found in $^{74}$Kr and in the $N = Z$ nucleus $^{72}$Kr (Korten (2001); Bouchez et al. (2003)).

The presence of large deformations as well as of shape coexistence in this region was in Piercey et al. (1981) ascribed to the existence of large voids ('gaps') in the single-particle spectrum (Nilsson diagram) for $N, Z = 40$, deformation parameter $\beta = 0$ and for $N, Z = 38$, $\beta = 0.3$ (Figure 4.1). The mutual reinforcement of the neutron and proton driving forces when both $N$ and $Z$ are at or near shell gaps with the same deformation, i.e. near zero or large, produces spherical or large deformation in the nuclei in this mass region. However, if only $N$ or $Z$ is around 40, a spherical shape is found only when the other particle number is near the strongly-closed-shell values of 28 or 50 (e.g. $^{68}_{28}\mathrm{Ni}_{40}$ and $^{90}_{40}\mathrm{Zr}_{50}$). As $Z$ and $N$ tend to deviate more from 28 or 50, the most stable shape for the nucleus will be more and more deformed. When both $N$ and $Z$ approach 40 from either direction, the $N = Z = 38$ gaps dominate, leading to large prolate deformations (e.g. $^{78}$Sr). Finally, as $N$ and $Z$ move away from both being at or near 38, the coexistence of spherical and deformed shapes starts to play an important role ($^{70,72}$Ge, $^{72,74}$Se, $^{74,76}$Kr). The existence of

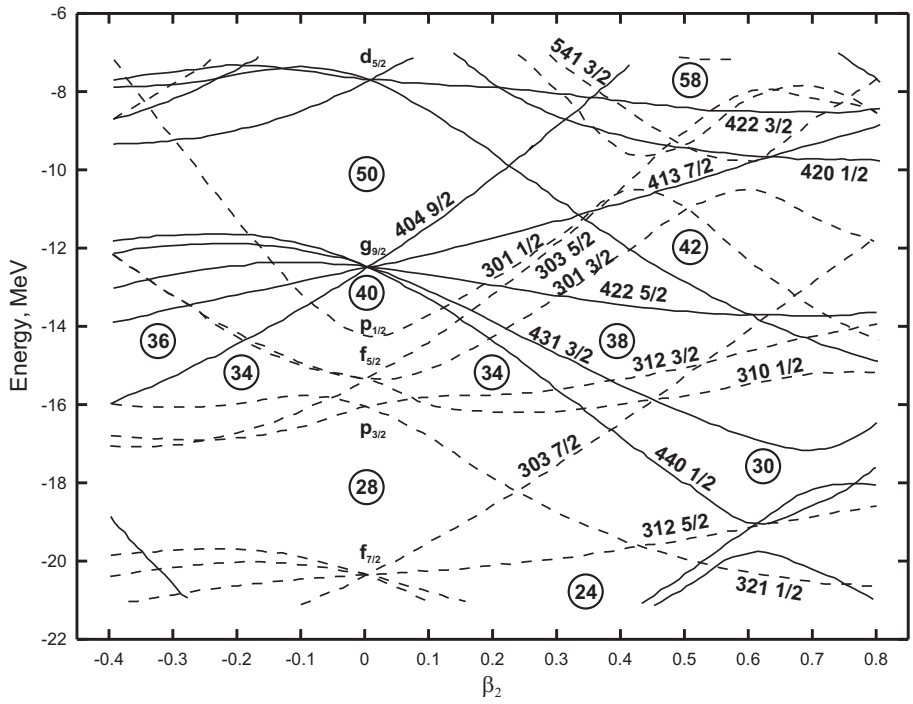


**Figure 4.1:** Nilsson single-particle levels as a function of the quadropole deformation for the region around $N = Z = 38$.

these 'deformed' magic numbers was theoretically predicted already in Brack et al. (1972).

We have determined the magnetic moment of the $5/2^-$ ground state of $^{69}$As ($Z = 33$, $N = 36$) from the anisotropy in the beta decay of this isotope and a subsequent NMR/ON measurement (Golovko et al. (2005b)). This moment will be compared to the magnetic moments of the same state in the other odd-$A$ arsenic isotopes.

Recently a detailed study of the levels in $^{69}$Se, $^{69}$As was carried out in Stefanescu et al. (2004b,a). The structure of odd-mass isotopes of As and Ge and the nuclear magnetic moments of $^{69,71,73}$As and of $^{69,71,73}$Ge were described in the framework of the proton-neutron interacting boson-fermion model by

Brant et al. (2004).

## 4.2 Experimental arrangement

The experiment with $^{69}$As ($T_{1/2} = 15.2$ min) was performed on-line at ISOLDE. The $^{69}$As nuclei were produced with a 1.4 GeV pulsed proton beam ($3 \cdot 10^{13}$ protons per pulse) from the CERN Proton Synchrotron Booster accelerator (PS Booster), using a standard niobium metal foil target (46.2 g/cm$^2$). The reaction products diffused from the target and effused to an ion-source chamber, where ionization by plasma discharge took place in the hot plasma ion source. The ionized nuclei were extracted at 60 keV, mass-separated by the ISOLDE General Purpose Separator (GPS), then transported through the beam distribution system and finally implanted into an iron foil inside the NICOLE $^3$He-$^4$He dilution refrigerator. The $^{69}$As beam intensity was typically about $8 \cdot 10^5$ ions/s. The iron implantation foil had been prepared by mechanically polishing a 99.99 % pure Fe foil (thickness 250 $\mu$m) from "Goodfellow" Company and then annealing it at 800 °C for 6 hours in hydrogen atmosphere, before it was soldered to the cold finger of the dilution refrigerator.

In the NICOLE refrigerator the nuclei were cooled to a temperature of about 10 mK and polarized with the LTNO method. The angular distribution of the $\beta$-particles was observed with HPGe particle detectors (Zákoucký et al. (2004); Vénos et al. (2000)) mounted inside the 4K radiation shield of the refrigerator. There is thus no window between source and detector, avoiding any energy loss as well as scattering of $\beta$ particles in radiation shields. In addition, the thickness of the particle detectors was chosen such that it was just enough to stop $\beta$ particles, thus keeping the sensitivity to $\gamma$-rays to the minimum, in order to minimize background contamination of $\gamma$-rays in the continuous $\beta$-spectra. Moreover, with $\gamma$-absorption in the particle detectors being minimal the detection of $\gamma$ radiation by the normal high-volume HPGe detectors outside the refrigerator is not hindered too much. The sensitive area of the $\beta$ particle detectors was around 110 mm$^2$. Their distance from the center of the sample was about 32 mm. The detectors were mounted slightly tilted with respect to the magnetization axis (angle of about 15°) to minimize scattering effects in the Fe host foil. The energy resolution was about 3 keV for 1 MeV $\beta$ particles. The

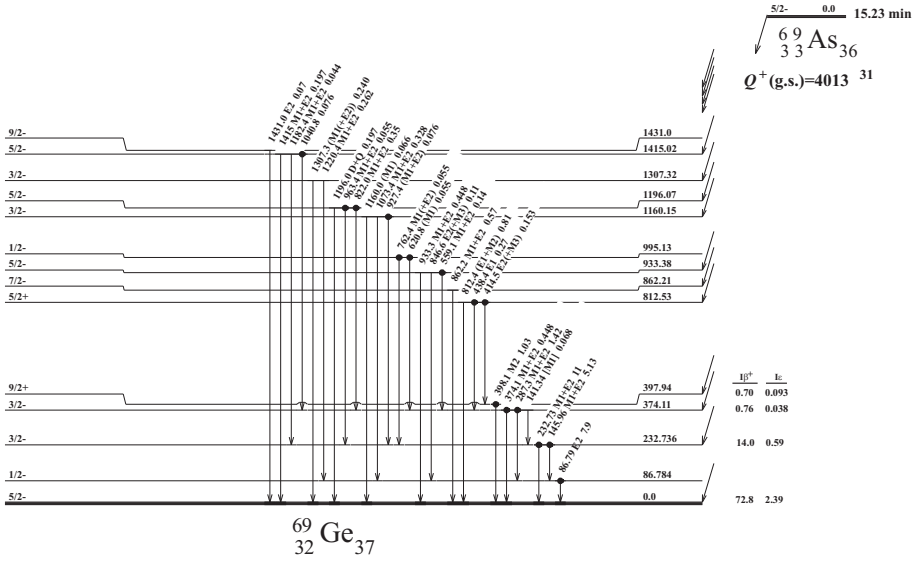


**Figure 4.2:** Low lying levels in $^{69}$Ge populated in the beta decay of $^{69}$As (adopted from Firestone (1996)). The most intense $\beta$-decay branch is from ground state to ground state with a $\beta^+$ intensity of 72.8 %.

detectors were connected with thin isolated copper wires (about 12 cm long) to the preamplifies outside the refrigerator. Thin wires were used in order to minimize the heat load from room temperature to the detector.

In addition, the angular distributions of $\gamma$ particles was observed with three high-volume HPGe detectors placed around the refrigerator, two positioned along the polarization axis and one perpendicular to it. The energy resolution of those detectors ranged from 2.5 to 4.0 keV at 1332 keV with efficiencies between 20 and 25 %. The temperature of the sample was measured using a $^{57}$CoFe nuclear orientation thermometer (Postma and Stone (1986)).

Fig. 4.2 shows the partial decay scheme for $^{69}$As. More detailed information can be found in Firestone (1996). The most intense $\beta$-decay branch is the allowed $I = 5/2^- \rightarrow I = 5/2^-$ ground state to ground state Gamow-Teller transition with endpoint energy $E_0 = 2991$ keV and a $\beta^+$ intensity of 72.8 %. The second most intense branch in the decay feeds the second excited level of $^{69}$Ge with a $\beta^+$ intensity of 14.0 %. The rest of the $\beta^+$ intensity is spread over

various other branches.

## 4.3 Data collection and Analysis

Firstly, the magnetic moment of $^{69}$As was estimated with the LTNO technique. The magnetic moment extracted from an on-line analysis of these data then provided the search region for the NMR/ON experiment. In order to fully saturate the 250 $\mu$m thick iron foil, firstly an external magnetic field of 0.5 T was applied, which was later reduced to $B_{\text{ext}} = 0.0994(10)$ T to minimize its influence on the trajectories of the $\beta$-particles. The two $\beta$ particle detectors were installed at 15° and 165° with respect to the external magnetic field. The $\beta$ anisotropy is defined as

$$\frac{W_\beta(15°)}{W_\beta(165°)} = \frac{\left[\dfrac{N(15°)}{N(165°)}\right]_{\text{mK}}}{\left[\dfrac{N(15°)}{N(165°)}\right]_{1\ \text{K}}} \tag{4.1}$$

For positrons from allowed $\beta$-decay one has

$$W(\theta) = 1 + f\frac{v}{c}B_1(\mu B/kT, I)\, A_1 Q_1 \cos\theta \tag{4.2}$$

where $v/c$ is the electron velocity relative to the speed of light all other parameters as defined in section 1.2. The magnetic moment for the ground state of $^{69}$As ($I = 5/2$) has been measured previously with the LTNO technique to be $\mu = +1.58(16)\mu_{\text{N}}$ (Severijns (1989)). Two values for the hyperfine field of As in Fe host are reported in the literature: $B_{\text{hf}} = +34.29(3)$ T (Kaplan et al. (1972)) and $B_{\text{hf}} = +34.394(27)$ T (Koi et al. (1972)). Apparently, both works refer to the same experiment. However, the latter work takes into account correction for diamagnetism. For our purpose this corrections is not necessary and we can adopt value cited by Kaplan et al. (1972) i.e. $B_{\text{hf}} = +34.29(3)$ T. During the $\beta$-NMR/ON experiment the temperature of the sample varied in the range between 15 and 22 mK.

The observed $\beta^+$ anisotropy depends on the energy of the beta particles (see Eq. 4.2). However, since in a $\beta$-NMR/ON experiment one is interested in

the destruction of the asymmetry pattern in the angular distribution of the $\beta$-particles, the entire energy region from 1205 keV to 2991 keV was used in order to improve statistics (Fig. 4.3). This was possible since the positron velocity relative to the speed of light for 1205 keV ($v/c \simeq 0.95$) is only 4 % smaller than the $v/c \simeq 0.99$ (see Eq. 1.25) for the endpoint energy of $^{69}$As leading to a negligible reduction of the $\beta$-anisotropy at the lower energies. A possible energy dependence of the asymmetry due to scattering and magnetic field effects was neglected. The energy region below 1205 keV was not used as it suffered from a background of Compton scattered 511 keV $\gamma$-rays and was also "contaminated" by positrons coming from the $\beta^+$ decay of the daughter isotope $^{69}$Ge, which has an endpoint energy of 1205 keV.

About 200 spectra of 300 s each were recorded. Firstly, two downward scans were made from 186 to 146 MHz (scans labels "1" and "2" in Table 4.1). Secondly, we made two upwards scans from 146 to 186 MHz (scans labels "3" and "4" in Table 4.1). Frequency steps were chosen to be 2 MHz with 2.8 MHz modulation amplitude and 0.1 kHz modulation frequency. In addition two scans with smaller frequency steps of 1 MHz with 1.1 MHz modulation amplitude and 0.1 kHz modulation frequency were performed in downward direction (one immediately after the other; scans labels "6" and "8" in Table 4.1) from 175 to 165 MHz.

As we already mentioned before, the rather broad initial search region was necessary due to the rather large errors on the nuclear magnetic moment values for $^{69}$As from a previous LTNO experiment, i.e. $\mu = +1.58(16)\mu_N$ (Severijns (1989)) and from the LTNO experiment that was performed just before the $\beta$-NMR/ON experiment discussed here, i.e. $\mu = +1.52(18)\mu_N$. For the first four scans, we later considered the region between 160 and 180 MHz, thus not taking into account points far from the resonance frequency. During the $\beta$-NMR/ON experiment the sample temperature varied between 15 and 22 mK. These changes in temperature were caused by a different power absorption by the system for different rf-frequencies. The data were corrected for the "dead-time" of the data acquisition system using a precision pulse generator.

As a fit function a simple Gaussian with a linear background was chosen. Figure 4.4(a) represents the result for the scan labeled as "4" in the frequency region from 160 to 180 MHz with a frequency step of 2 MHz. Figure 4.4(b) represents

the result for the scan labeled as "8" in the frequency region from 165 to 175 MHz with a frequency step of 1 MHz. Fig. 4.5 and Table 4.1 summarize the results of all single scans, including both the data with a frequency step of 2 MHz as well as of 1 MHz.

From the quality of the $\beta$-NMR/ON data (see Fig. 4.4(a)) and the results of the fits (Table 4.1) it is obvious that the relaxation time should be much smaller than the half-life $T_{1/2} = 15.23$ min of $^{69}$As, i.e. of the order of one minute or less. No experimental value of the relaxation constant $C_K$ is available for an As isotope in Fe. However, our NMR/ON measurements for $^{69}$As were performed in the sweep-mode technique, which is described in detail in section 1.4 of Chapter 1. With this technique the rf-frequency is continuously swept over the resonance region. It is then possible to extract simultaneously the resonance frequency and the spin-lattice relaxation time from the data. Indeed, the common fit[1] of our NMR/ON results using Eq. 1.33 has yielded for the spin-lattice relaxation time of $^{69}$As in iron $T_1(^{69}\text{As}\underline{\text{Fe}}) = 10(25)$ s. From the fit quality we can conclude that our data represents a slow-sweep limit. In other words, the spin-lattice relaxation time is much shorter then the measuring time at each frequency.

In Kaplan et al. (1972) an attempt was made to measure the spin-lattice relaxation time of $^{74}$As in Fe by following the return of the $\gamma$-ray anisotropy after destruction at the centre NMR frequency. Their combined data from ten passes gave a half-time of 85 s, corresponding to a mean time of 122 s, assuming a single exponential decay, at a temperature of 20 mK. This time measurement is probably accurate to 50 %. With $T_1(^{74}\text{As}\underline{\text{Fe}}) = 122$ s at $T_\text{L} = 20$ mK one finds $C_\text{K}(^{74}\text{As}) = 2440$ s $\cdot$ mK. Eq. 1.12 then yields $C_\text{K}(^{69}\text{As}) = 3810$ s $\cdot$ mK, corresponding to $T_1 = 190$ s at 20 mK. Our measurement were performed in $B_\text{ext} = 0.1$ T, while the field was 0.179 T in the experiment with $^{74}$As. Taking into account that relaxation then proceeds faster by a factor of about 1.5 and the fact that Kaplan et al. (1972) state that their result is accurate to about 50 % the agreement between the $T_1$ values observed for $^{69}$As and $^{74}$As is reasonable.

[1] The error represents mainly the statistical error. The statistical error includes the $S$-factor corrections (see appendix B). The fit procedure is outlined in details in Tramm (2004). P. Herzog and Ch. Tramm, private communications.

## 4.4 Results and Discussion

From the obtained resonance frequency $\nu_{\rm res} = 169.98(7)$ MHz, and the spin $I = 5/2$ for the ground state of $^{69}$As, the Plank constant $h$, and the total magnetic field ($B_{\rm tot} = B_{\rm hf} + B_{\rm ext}\,(1+K) - B_{\rm dem}$ with the external magnetic field $B_{\rm ext} = 0.0994(10)$ T, the hyperfine field $B_{\rm hf} = 34.29(3)$ T, the demagnetization [2] field $B_{\rm dem} = 0.025(5)$ T and $K = -0.01(5)$), the nuclear magnetic moment of $^{69}$As is obtained as:

$$\mu[^{69}\mathrm{As}] = +1.623 \pm 0.002\,\mu_{\rm N} \tag{4.3}$$

where most of the error is due to the error of the value for $B_{\rm hf}$. The magnetic moments of the $\pi f_{5/2}$ level in the odd-$A$ As isotopes are listed in Table 4.2.

Mayer (1950a,b) in first postulating the ideas of the shell model made the simple but effective assumption that the internucleon interaction was such that an even number of neutrons or protons in a given level coupled to the spin $j$ of that level. Nuclei with an even number of protons (neutrons) and an odd number of neutrons (protons) should have the spin and parity of the last odd neutron (proton) and this rule is also generally obeyed. Therefore, the nuclear ground-state properties in this extreme single-particle model are vested in a available single particle (hole) state.

The Schmidt (single particle) value for the odd-mass $f_{5/2}$ arsenic isotopes can be calculated from i.e. Bohr and Mottelson (1998); Blin-Stoyle (1956) as

$$\mu_{\rm sp} = j g_j \mu_{\rm N} = j\left(g_l \pm (g_s - g_l)\,\frac{1}{2l+1}\right)\mu_{\rm N};\;\; j = l \pm 1/2 \tag{4.4}$$

where

$$g_l = \begin{cases} 1; & \text{proton } (\pi) \\ 0; & \text{neutron } (\nu) \end{cases} \qquad \mathrm{g_s} = \begin{cases} +5.585; & \pi \\ -3.826; & \nu \end{cases} \tag{4.5}$$

The Schmidt value for the $\pi f_{5/2}$-level is then $\mu_{\rm sp} = +0.864\ \mu_{\rm N}$.

[2] Substituting typical values for the dimensions ($a > b \gg c$) of the iron foil used in the $\beta$-NMR/ON experiments of $^{69}$As (i.e. $a \approx 15$ mm, $b \approx 9.4$ mm, $c \approx 0.250$ mm) in Eq. 1.29 and using the magnetization value for iron $\mu_0\mathbf{M} = 2.29$ T we get from Eq. 1.28 for the demagnetization field in each direction: $B_{\rm dem}(a:b:c) = (26.4;\ 38.5;\ 2225)$ mT. This shows that in our thin foil the external field applied along the $b$-direction will be reduced by $B_{\rm dem} = 0.0385(77)$ T. In order to account for approximations used in Eq. 1.29 we have adopted a 20 % error to this value.

**Table 4.2:** Theoretical and experimental magnetic moments for the lowest $5/2^-$ state in the odd-$A$ As isotopes. For details on the calculation of the theoretical values the reader is referred to the text. The neutron configurations are not given, however they can be found in Herzog et al. (1976).

| N | Isotope | $E_{5/2}$, keV | $\pi$-configuration | $\mu_{\rm th}$, $\mu_{\rm N}$ | $\mu_{\rm exp}$, $\mu_{\rm N}$ |
|---|---|---|---|---|---|
| 36 | $^{69}$As | 0 | $(1f_{5/2})^1$ | 1.59[b] | +1.623(2)[a] |
| | | | | 1.68[c] | |
| | | | | 1.465[d] | |
| 38 | $^{71}$As | 0 | $(2p_{3/2})^2(1g_{9/2})^2(1f_{5/2})^1$ | 1.81[f] | +1.6735(18)[e] |
| | | | | 1.46[d] | |
| 40 | $^{73}$As | 67 | $(2p_{3/2})^2(1g_{9/2})^2(1f_{5/2})^1$ | 1.72[f] | +1.63(10)[g] |
| | | | | 1.43[d] | |
| 42 | $^{75}$As | 280 | $(1f_{5/2})^5$ | 0.96[f] | +0.81(9)[g] |
| 44 | $^{77}$As | 264 | $(1f_{5/2})^5$ | 0.91[f] | +0.83(7)[g] |

[a] This work: $\beta$-NMR/ON result.
[b] This work: strong coupling model with 'effective' $g$-factors.
[c] P. Herzog: core polarization model (see Noya et al. (1959)), private communication.
[d] Brant et al. (2004): IBFM model, $\mu_{\rm th}$ obtained from private communication.
[e] Herzog et al. (1976): $\gamma$-NMR/ON result.
[f] Herzog et al. (1976): core polarization model (see Noya et al. (1959)).
[g] Adopted from Raghavan (1989).

While the moments of $^{75}$As and $^{77}$As are in good agreement with the Schmidt value, those of $^{69,71,73}$As deviate from it by about a factor two. This drastic change in the magnetic moment between $^{73}$As and $^{75}$As was attributed in Bertschat et al. (1973) to a rearrangement of proton pairs while passing the magic neutron number 40. Calculations by Herzog et al. (1976) that were carried out on the basis of the core polarization model of Noya et al. (1958) confirmed this (column 5 in Table 4.2). It is to be noted though that the authors themselves quote their result to be only an estimate for the magnetic moment. The value reported in Severijns (1989) (i.e. $\mu[^{69}\text{As}] = +1.58(16)\,\mu_{\rm N}$)[3] was larger than the one of Hogervorst et al. (1980) (i.e. $\mu[^{69}\text{As}] = +1.2(2)\,\mu_{\rm N}$)[4] and fits well into the systematics.

In a nucleus, the $g$-factors of the proton ($\pi$) and neutron ($\nu$) are obviously

[3] The result was obtained from LTNO experiment.
[4] The result was obtained from atomic beam magnetic resonance experiment.

influenced by the medium (the presence of the other nucleons), and therefore it would be more appropriate to use 'effective' proton and neutron $g$-factors to calculate the single particle moments. A calculation of the single-particle moment for the $f_{5/2}$ state, taking into account the influence of configuration mixing, core polarization and meson exchange (see Kumar (1990)) by using the effective gyromagnetic ratios $g_s^{\mathrm{mod}} = 0.7 g_s^{\mathrm{free}}$, $g_l^{\mathrm{mod}}(\pi) = +1.1$ and $g_l^{\mathrm{mod}}(\nu) = -0.05$ or

$$g_l^{\mathrm{mod}} = \begin{cases} +1.10; & \pi \\ -0.05; & \nu \end{cases} \quad g_s^{\mathrm{mod}} = \begin{cases} +3.906; & \pi \\ -2.674; & \nu \end{cases} \tag{4.6}$$

yields[5] $\mu_{\mathrm{sp}}^{\mathrm{mod}} = +1.748\ \mu_{\mathrm{N}}$, which is in reasonably good agreement with the experimental result. The fact that this value also compares well with the theoretical as well as experimental magnetic moments for $^{71}$As and $^{73}$As, moreover, clearly indicated that there is no change in proton configuration between $^{71}$As and $^{69}$As.

In Reinwater (1950); Bohr (1951b) a nuclear model was discussed in which the individual nucleons are assumed to move in an average nuclear field which deviates from spherical symmetry. This so-called asymmetric model contains many of the characteristic features of the single particle model, and at the same time incorporates such collective types of the nuclear motion as the nuclear magnetic moment.

The asymmetric model implies that the nuclear core possesses rotational degrees of freedom. The character of a nuclear state, and its magnetic moment in particular, is therefore not determined uniquely by the quantum numbers of the single particle motion, but depends also on the coupling of this motion to the asymmetric nuclear core and on rotational state of the nucleus (Bohr (1951a)). In a more detailed classification of the nuclear states it is necessary to compare the strength of the couplings between the various angular momentum vectors of the nucleus (Bohr (1951b)).

Bohr suggested that for a strong coupled system ($I = j > 3/2$) consisting of a single particle and the distorted nuclear core, the magnetic moment is given

[5] We should mention that in calculating the given value $\mu_{\mathrm{sp}}^{\mathrm{mod}} = +1.748\ \mu_{\mathrm{N}}$ no neutron excitation (see Eq. 4.6) were taken into account.

by (Bohr (1951b); Bohr and Mottelson (1953))

$$\mu_{\rm sc} = \mu_{\rm sp} - (g_j - g_R)\,\frac{I}{I+1}\mu_{\rm N} \tag{4.7}$$

where $g_R$ is the angular momentum carried by the core. For a uniformly charged nucleus $g_R = Z/A$. Taking into account the Schmidt value for the magnetic moment of $^{69}$As and Eq. 4.7 one then finds $\mu_{\rm sc} = +0.959\ \mu_{\rm N}$ when using the 'bare', $g$-factors and $\mu_{\rm sc}^{\rm mod} = +1.590\ \mu_{\rm N}$, when taking into account the 'effective' (modified) $g$-factors from Eq. 4.6. Although we used a quite simple approach the obtained value assuming strong coupling and 'effective' $g$-factors (viz. $\mu_{\rm sc}^{\rm mod} = +1.590\ \mu_{\rm N}$) is very close to the experimental one. Our $\beta$-NMR/ON result for the moment of $^{69}$As confirms the value of Severijns (1989) but is more precise.

Recently, Brant et al. (2004) performed calculations in the framework of the proton-neutron interacting boson-fermion model which yielded for the magnetic moment of the $^{69}$As ground state $\mu[^{69}{\rm As}] = +1.465\,\mu_{\rm N}$. Due to the fact that these calculations have not been done for this single nucleus, but for a sequence of even-even, odd-even and even-odd nuclei in the $A = 70$ mass region, the agreement with experiment is rather good.

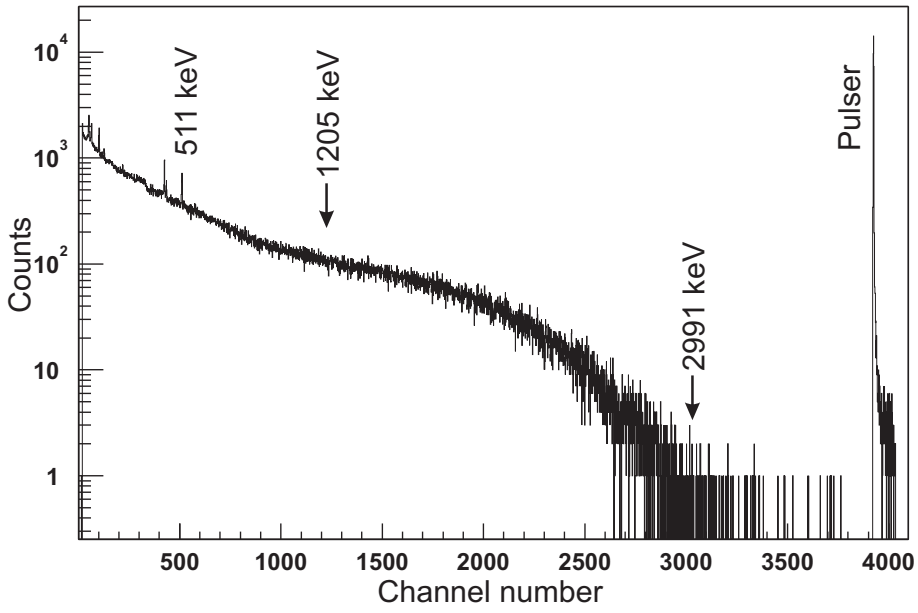


**Figure 4.3:** Typical $\beta$-spectrum for $^{69}$As recorded within one 300 s measurement cycle. The 511 keV positron annihilation line and the pulser peak are indicated. Since in a $\beta$-NMR/ON experiment one is only interested in the destruction of the asymmetry in the angular distribution of the $\beta$-particles, the entire energy region from 1205 keV to the endpoint at 2991 keV was used in order to improve statistics. The energy region below 1205 keV was not used as it suffered from background of Compton scattered 511 keV $\gamma$-rays and was also contaminated by positrons coming from the $\beta^+$-decay of the daughter isotope $^{69}$Zn, which has an endpoint energy of 1205 keV.

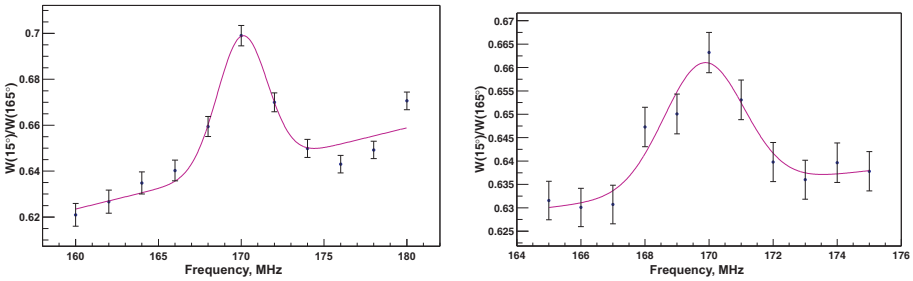


(a) scan '4' (b) scan '8'

**Figure 4.4:** On-line $\beta$-NMR/ON on $^{69}$As curves for the scan labelled as '4' (left) and the scan labelled as '8' (right). The resonance frequency for these scans are given in Table 4.1. Plotted is the ratio of the pulser normalized $\beta$ anisotropies $W(15°)$ and $W(165°)$ $\beta$ detectors as a function of rf frequency.

**Table 4.1:** Overview of the $\beta$-NMR/ON frequency scans for $^{69}$As (see also Fig. 4.5).

| scan | $\nu$, MHz | step, MHz | $\nu_{\mathrm{res}}$, MHz |
|---|---|---|---|
| 1 | 180→160 | 2.0 | 170.19 ± 0.19 |
| 2 | 180→160 | 2.0 | 169.73 ± 0.18 |
| 3 | 160→180 | 2.0 | 170.06 ± 0.14 |
| 4 | 160→180 | 2.0 | 170.06 ± 0.12 |
| 6 | 175→165 | 1.0 | 169.73 ± 0.22 |
| 8 | 175→165 | 1.0 | 169.84 ± 0.20 |
| weighted average (all) | | | 169.98 ± 0.07 |

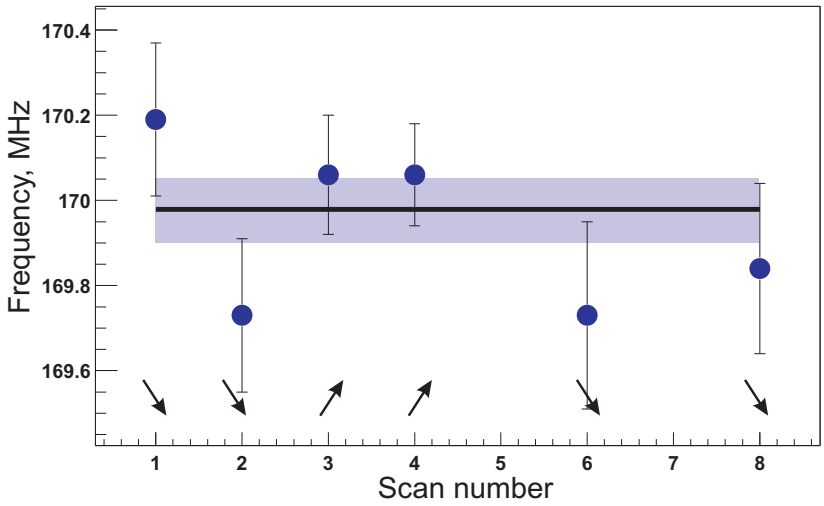


**Figure 4.5:** Overview of the results of all individual $\beta$-NMR/ON scans on $^{69}$AsFe. Arrows indicate the direction in which the frequency region was stepped through. The resonance frequency values and their errors are given in Table 4.1. The band represents the weighted average.

# Chapter 5

# Nuclear Magnetic Moment of $^{104m}$Ag

## 5.1 Introduction

The nucleus $^{104}$Ag has a ground state ($I^\pi = 5^+$, $T_{1/2} = 69$ min) and an isomeric state ($I^\pi = 2^+$, $T_{1/2} = 33.5$ min) at an excitation energy of only 6.9 keV. The nuclear moment of the ground state is known from previous NMR/ON measurements (Vandeplassche et al. (1986)). Although the magnetic moment of the isomeric state was measured previously too already, i.e. with the atomic beam magnetic resonance technique (Ames et al. (1961))[1], the precision of this result was not high enough to extract the isospin mixing amplitude from the $\beta$-asymmetry for this state (see below).

We have therefore carried out a $\beta$-NMR/ON measurement on $^{104m}$Ag in Fe (Golovko et al. (2005a)). A RILIS measurement on $^{104m}$Ag was performed

[1] A careful comparison of the works of Ames et al. (1961), Greenebaum and Phillips (1974), and Van Walle (1985) showed that the value $\mu = 4.12(25)\,\mu_N$ that is listed for $^{104}$Ag in the Table of Magnetic Moments of Raghavan (1989) is in fact the value that was obtained by Greenebaum and Phillips for $^{102m}$Ag which was erroneously listed under $^{104m}$Ag in Van Walle (1985).

first in order to determine the frequency search region. As a consistency check we also performed $\gamma$-NMR/ON on the $^{104}$Ag ground state. The value obtained for the moment of $^{104g}$Ag, i.e. $\mu[^{104g}\mathrm{Ag}] = +3.918 \pm 0.002\,\mu_\mathrm{N}$ is in agreement and more precise than the one that is reported in the literature (i.e. $\mu[^{104g}\mathrm{Ag}] = +3.914(8)\,\mu_\mathrm{N}$ see Vandeplassche et al. (1986)). For the magnetic moment of $^{104m}$Ag we have found $\mu[^{104m}\mathrm{Ag}] = +3.689 \pm 0.003\,\mu_\mathrm{N}$.

## 5.2 Experimental details

The Ag isotopes used for the $\beta$-NMR/ON studies reported here were obtained from the decay of the $^{104}$Cd precursor produced with the ISOLDE facility. The radioactive $^{104}$Cd ($T_{1/2}$=57.7 min) was produced with a proton beam from the PS Booster (intensity of $8 \cdot 10^{12}$ protons per pulse, staggered mode), bombarding a tin liquid metal target. After ionization and acceleration to 60 keV the $^{104}$Cd beam was mass-separated by the GPS, transported through the beam distribution system and implanted into a 125 $\mu$m thick, 99.99 % pure iron foil soldered onto the cold finger of the low-temperature nuclear orientation set-up NICOLE. The iron foil supplied by Goodfellows$^{\mathrm{TM}}$, was polished and annealed in the presence of a hydrogen atmosphere at $\approx 800°$C for about six hours.

In addition to the iron foil, a $^{57}$CoFe nuclear thermometer was soldered to the cold finger of the dilution refrigerator. The samples was cooled down to 8-12 mK. A polarizing magnetic field of 0.5 T was applied by the superconducting split coil magnet in order to fully magnetize the iron foil. This field was then lowered to $B_\mathrm{ext}$ =0.1008(3) T to reduce its influence on the trajectories of the $\beta$-particles.

The $\beta$ and $\gamma$ decay radiations were detected with HPGe particle detectors inside the 4 K radiation shield and three high volume HPGe $\gamma$-rays detectors outside the dilution refrigerator. The geometry of all detectors was about the same as for the other $\beta$-NMR/ON experiments mentioned before (see e.g. Chapter 3). Dead-time correction was achieved by using a precision pulse generator.

In view of the rather long half-life for both isotopes and their respective mag-

**Table 5.1:** Overview of the $\gamma$-NMR/ON resonance frequency ($\nu_{\rm res}$) for different $\gamma$-rays of $^{104g}$Ag.

| Energy, keV | $\nu_{\rm res}$, MHz |
|---|---|
| 555.8 | 266.77 ± 0.13 |
| 767.6 | 266.66 ± 0.06 |
| 941.6 | 266.74 ± 0.09 |
| $\overline{\nu}_{\rm res}$ | 266.70 ± 0.05 |

netic hyperfine interaction strength ($^{104g}$Ag: $T_{1/2} = 69.2$ min, $T_{\rm int} = 12.8$ mK; $^{104m}$Ag: $T_{1/2} = 33.5$ min, $T_{\rm int} = 30.1$ mK) no problems with incomplete spin-lattice relaxation are to be expected here.

### 5.2.1 $\gamma$-NMR/ON on $^{104g}$Ag in Fe

The decay scheme for $^{104m}$Ag is rather complex (see e.g. Firestone (1996)), with the most intense $EC/\beta^+$ branch populating the $2^+$ level at 555.81 keV in $^{104}$Pd. Unlike $^{104m}$Ag, the decay of the $5^+$ $^{104g}$Ag ground state does not populate any particular level in $^{104}$Pd very strongly. The 555.8, 767.8, and 941.6 keV transitions are known to be the three most intense $\gamma$-rays in the decay of $^{104g}$Ag. Of these the 941.6 and 767.8 keV originate from the decay of $^{104g}$Ag only (Guin et al. (1990)). As these three $\gamma$-lines were clearly visible in the spectrum it was decided to perform a $\gamma$-NMR/ON experiment on $^{104g}$Ag in order to check the total magnetic field (hyperfine field, external field and demagnetization field) for our set-up.

The radio frequency field was again applied with the same two-turn rf-coil. The modulation frequency was 0.1 kHz, the modulation bandwidth 0.5 MHz. The center frequency was varied in steps of 0.5 MHz over the resonance search region (from 263.5 MHz to 270 MHz). Two scans were performed: one with increasing and one with decreasing center frequency in order to avoid possible shifts of the (effective) resonance centers due to a finite spin-lattice relaxation time. The level of the rf-signal from the Marconi generator was kept at -32 dBm. A linear rf-amplifier with a constant gain of 46 dBm was installed between the Marconi generator and the rf-coil. $\beta$-particle and $\gamma$-ray spectra were accumulated for

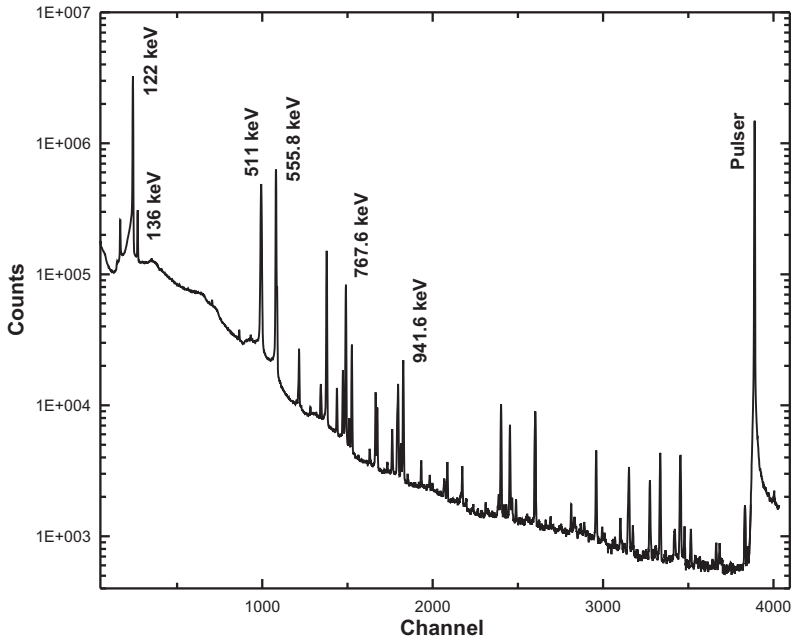


**Figure 5.1:** Typical $\gamma$-spectrum observed for $^{104g,m}$Ag. The 511 keV positron annihilation line, the 122 and 136 keV lines of the $^{57}$CoFe nuclear thermometer, and the 555.8, 767.6, 941.6 keV $\gamma$-ray lines of $^{104g}$Ag that were used for $\gamma$-NMR/ON are indicated. Most of the other $\gamma$-ray lines belong to the decays of $^{104g,m}$Ag (see Firestone (1996)). The strong line between the 555.8 keV and 767.6 keV lines is the 709 keV $\gamma$-ray from the decay of $^{104}$Cd.

300 s at each frequency.

To illustrate the quality of the data Fig. 5.1 shows a typical $\gamma$-ray spectrum. The 122 keV and 136 keV lines are from the decay of the $^{57}$CoFe nuclear thermometer. The $\gamma$-lines 555.8, 767.6 and 941.6 keV were used in the $\gamma$-NMR/ON experiment.

Special care was taken to eliminate the effects of variations in the $^{104}$Cd beam intensity by taking the ratio $W(0)/W(\pi/2)$ as the anisotropy function. A NMR effect was observed on all three above mentioned $\gamma$-rays in the decay of $^{104g}$Ag (Fig. 5.2). Table 5.1 summarizes the result of the fits of the $\gamma$-NMR/ON results for the three different lines. A Gaussian with a linear background was used as

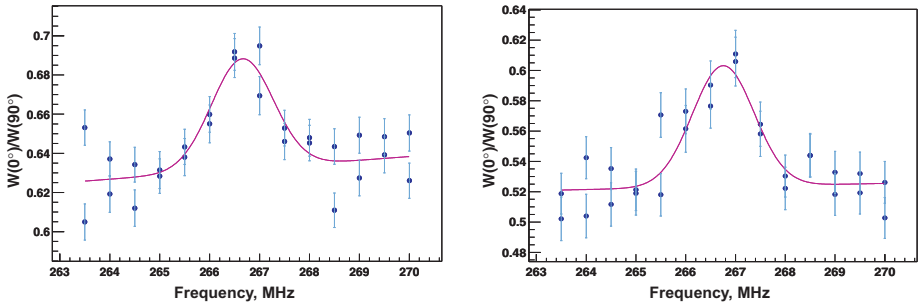


(a) 767.6 keV (b) 941.6 keV

**Figure 5.2:** On-line $\gamma$-NMR/ON curve for the 767.6 keV $\gamma$-line (a) and the 941.6 keV $\gamma$-line (b) of $^{104g}$Ag. The resonance frequencies for these scans are given in Table 5.1. Plotted is the ratio of the pulser normalized $\gamma$-anisotropies $W(0°)/W(90°)$ as a function of rf frequency. The integrated destruction of $\gamma$-anisotropy is 8% for the 767.6 keV $\gamma$-line and 14% for the 941.6 keV $\gamma$-line. The data points for both scans (one in upward and one in downward direction) are superposed.

a fit function. The weighted average of the three central frequencies leads to $\nu_{\rm res} = 266.70(5)$ MHz. This agrees well with the value of $\nu_{\rm res} = 266.3(5)$ MHz that was obtained previously in another NMR/ON experiment (Vandeplassche et al. (1986); Van Walle (1985)).

As was already mentioned in section 1.4 of Chapter 1 the resonance frequency is related to the nuclear magnetic moment through the relation given by Eq. 5.1

$$\nu_{\rm res}({\rm MHz}) = \frac{7.623 \cdot \mu(\mu_{\rm N}){\rm B_{tot}(Tesla)}}{{\rm I}(\hbar)} \tag{5.1}$$

with $B_{\rm tot} = B_{\rm hf} + B_{\rm ext}(1+K) - B_{\rm dem}$. For the hyperfine field of Ag in Fe we used $B_{\rm hf} = -44.716(19)$ T, which is the weighted average of two values cited in the literature, i.e. –44.72(2) T (Fox et al. (1971) and –44.69(5) T (Eder et al. (1984)). Further, $B_{\rm ext} = 0.1008(3)$ T, while the Knight shift for silver in iron has been measured previously by Eder et al. (1984) as $K(^{106}{\rm Ag\underline{Fe}}) = -0.03(2)$.

The demagnetization field for the Fe foils used was calculated to be $B_{\rm dem} = 0.0259(52)$ T (see also section 1.4). The total magnetic field is then $B_{\rm tot} = 44.644(21)$ T. Combining this with the measured resonance frequency yields for the magnetic moment of $^{104g}$Ag: $\mu[^{104g}{\rm Ag}] = +3.918 \pm 0.002\,\mu_{\rm N}$. This

is in agreement and more precise than the value $\mu[^{104g}\mathrm{Ag}] = +3.914(8)\,\mu_\mathrm{N}$ that was previously obtained by Van Walle (1985) with $\gamma$-NMR/ON (see also Vandeplassche et al. (1986)), and with $\mu[^{104g}\mathrm{Ag}] = +3.919(3)\mu_\mathrm{N}$ obtained in an atomic beam magnetic resonance technique (see Dinger et al. (1989)). The good agreement between all values confirms the calibration of our superconducting magnet. The manufacturer's computed homogeneity for the magnet is 0.25 % in a 1 cm diameter spherical volume. In an analogous refrigerator built by the same manufacturer (Oxford Instruments$^{\mathrm{TM}}$) the calibration of the magnet has been checked with $^{60}$CoFe $\gamma$-NMR/ON and found to be in very good agreement with the specifications too (see Hutchison et al. (1992)).

### 5.2.2 $\beta$-NMR/ON on $^{104m}$Ag in Fe

The main goal of the NMR/ON run with $^{104}$Ag was the determination of the magnetic moment of the isomeric state $^{104m}$Ag in order to be able to extract the isospin impurity from the $\beta$-anisotropy. In order to reduce the search region for the $\beta$-NMR/ON the $^{104m}$Ag the magnetic moment was first determined by scanning the first of two lasers used to selectively ionize Ag atoms in the RILIS ion source. The on-line analysis of this measurement yielded $\mu[^{104m}\mathrm{Ag}] = 3.7(1)\mu_\mathrm{N}$ (U. Köster, private communication), corresponding to a resonance frequency $\nu_\mathrm{res} = 630 \pm 17$ MHz which was subsequently used as the search region for the $\beta$-NMR/ON experiment.

An initial search was performed with a triangular modulation signal of 100 Hz frequency and $\pm$1 MHz amplitude, and a nominal rf-power level of -42 dBm. A constant linear rf-amplifier was used as well. A typical $\beta$-spectrum obtained in 300 s is presented in Fig. 5.3. About 350 spectra of 150 s and 300 s collecting time were recorded. In order to increase statistics we monitored the destruction of the asymmetry in the $\beta$-angular distribution for the energy region from 600 keV to the endpoint at 2708 keV. The observed $\beta$ anisotropy effect in this region was $R = 1 - \frac{W(15^\circ)}{W(165^\circ)} \simeq 50$ %. The energy region below 600 keV was not used as it suffered from background of Compton scattered 511 and 555.8 keV $\gamma$-lines. NMR-scans were performed in both frequency directions, but no difference between the center frequencies was found for passes in opposite directions. In addition, we performed this time FM-off/FM-on experiments

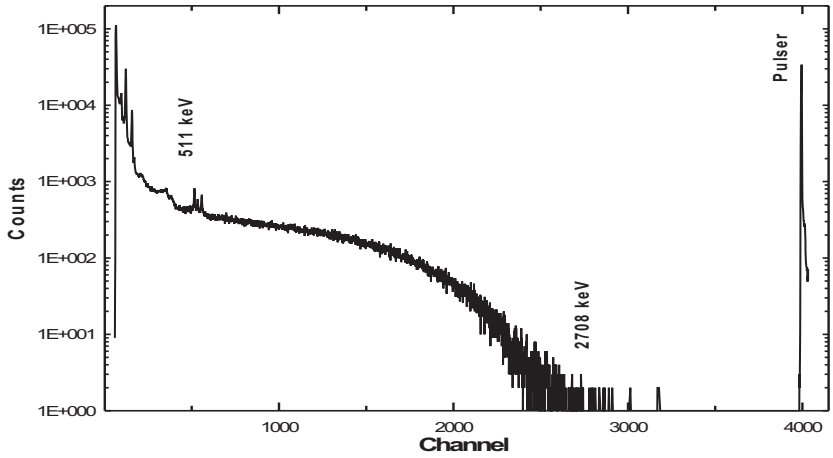


**Figure 5.3:** Typical $\beta$-spectrum for $^{104m}$Ag. The endpoint energy for the decay of $^{104m}$Ag is indicated ($E_{\text{endpoint}} = 2708$ keV). The $\beta^+$ endpoint energy of $^{104g}$Ag is 1933 keV, however we neglected it due to a small contribution to the total $\beta$-spectrum (see Firestone (1996) and Fig. 8.1 in Chapter 8). One also sees the 122, 136, 511, and 555.8 keV $\gamma$-rays peaks. The collection time for this spectrum was 300 s.

which better defines the line shape. This was expected to be helpful since a rather broad resonance line was expected in this high frequency region. Fig 5.4 shows the destruction $S$ of the $\beta$-asymmetry as a function of the frequency. This destruction is defined as the difference between the ratio $W(15°)/W(165°)$ with FM-on and FM-off normalized to the ratio with FM-off (see Fig. 5.4):

$$S = \frac{\left(\left[\frac{W(15°)}{W(165°)}\right]_{\text{FM on}} - \left[\frac{W(15°)}{W(165°)}\right]_{\text{FM off}}\right)}{\left[\frac{W(15°)}{W(165°)}\right]_{\text{FM off}}} \tag{5.2}$$

The total destruction observed was about 4 %. This is much smaller than in the experiments with $^{59}$Cu and $^{69}$As e.g. for $^{59}$Cu a destruction of about 46 % was obtained. Again NMR/ON data were fitted using a simple Gaussian with a constant background. Table 5.2 lists the results of the various independent $\beta$-NMR/ON experiments that were performed.

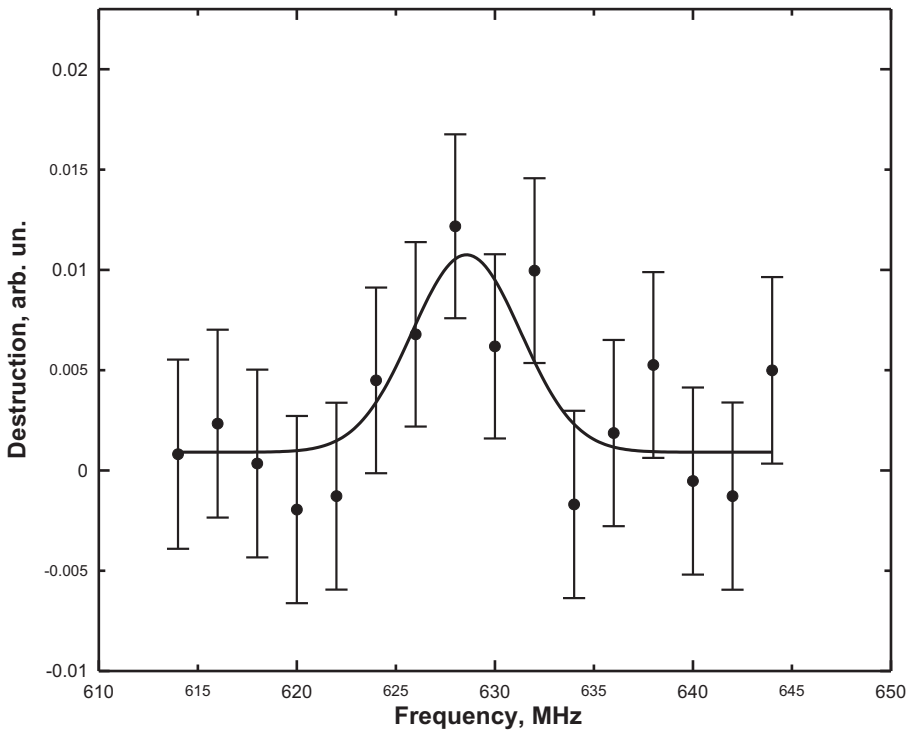


**Figure 5.4:** $\beta$-NMR/ON of $^{104m}$AgFe at applied field of $B_{\text{ext}} = 0.1008(3)$ T. Three passes with opposite frequency stepping directions have been added together, using FM-off/FM-on sequence. The total destruction observed was about 4 %.

## 5.3 Results and discussion

### $^{104g}$Ag

From the resonance frequency for $^{104g}$Ag ($\nu_{\text{res}} = 266.70(5)$ MHz), the spin ($I = 5$) of this ground state, the total magnetic field of silver in iron in our experimental conditions, i.e. $|B_{\text{tot}}| = 44.644(21)$ T, and using Eq. 5.1, the nuclear magnetic moment of the $^{104g}$Ag ground state is obtained as

$$\mu[^{104g}\text{Ag}] = 3.918 \pm 0.002 \mu_{\text{N}}, \tag{5.3}$$

which is in very good agreement with the value from literature ($\mu[^{104g}$Ag] =

**Table 5.2:** Overview of the $\beta$-NMR/ON frequency scans for $^{104m}$Ag (see also Fig. 5.5).

| Scan | Modulation | $\nu_{\mathrm{res}}$, MHz | Step, MHz | Time, s |
|---|---|---|---|---|
| 1 | on | 628.3(8) | 2 | 150 |
| 2 | on | 627.0(8) | 2 | 300 |
| 3 | on | 628.3(9) | 5 | 300 |
| 4 | off/on | 627.2(7) | 2 | 300 |
| 5 | off/on | 628.0(1.1) | 2 | 150 |
| 6 | off/on | 629.1(2.9) | 2 | 150 |
| 7 | off/on | 628.1(1.9) | 2 | 150 |
| $\overline{\nu}_{\mathrm{res}}$ | | 627.7(4) | | |

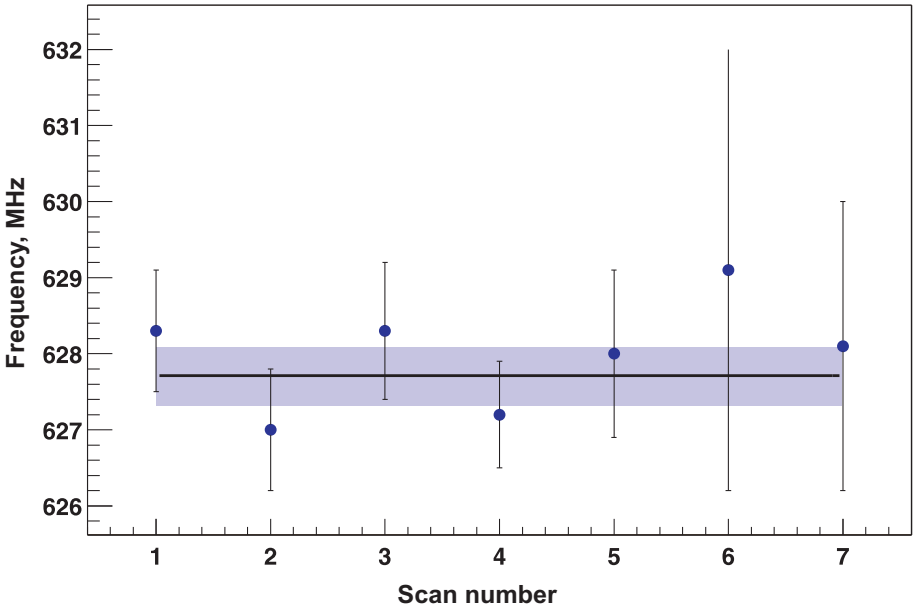


**Figure 5.5:** Overview of the results of all individual $\beta$-NMR/ON scans on $^{104m}$AgFe. The resonance frequency values and their errors are given in Table 5.2. The band represents the weighted average.

$+3.914(8)\mu_N$; see Van Walle (1985); Vandeplassche et al. (1986) and $\mu[^{104g}\text{Ag}] = +3.919(3)\mu_N$; see Dinger et al. (1989)).

**$^{104m}$Ag**

From the resonance frequency for $^{104m}$Ag ($\nu_{res}$ = 627.7(4) MHz), the spin ($I = 2$) of this isomeric state, the total magnetic field $|B_{tot}| = 44.644(21)$ T and using Eq. 5.1, the nuclear magnetic moment of $^{104m}$Ag is obtained as:

$$\mu[^{104m}\text{Ag}] = 3.689 \pm 0.003\mu_N \tag{5.4}$$

This value is much more precise than the results from previous works, i.e. $+3.7(2)$ $\mu_N$ (Ames et al. (1961)) and the result from the RILIS technique (viz. 3.7(1) $\mu_N$) obtained prior to our measurement during the same beam time.

For the heavier neutron deficient Ag isotopes $^{106}$Ag, $^{108}$Ag, and $^{110}$Ag (with a $1^+$ ground state and a $6^+$ isomeric state) the magnetic moment could be explained by the configuration of the form $\pi(g_{9/2}^{-3})_{7/2}\nu(d_{5/2}^{-1})$ (see Van Walle (1985)). However, in $^{104g,m}$Ag and also in $^{102g,m}$Ag (i.e. Vandeplassche et al. (1983)) one has a $2^+$, $5^+$ doublet which does not fit into a unique $\pi - \nu$ configuration, but was suggested to be a mixing of the following two configurations (i.e. Ames et al. (1961) and Van Walle (1985)):

1. $\pi(g_{9/2}^{-3})_{7/2}\ \nu(d_{5/2}^{-1})$,
2. $\pi(g_{9/2}^{-3})_{9/2}\ \nu(d_{5/2}^{-1})$.

Note that this doublet is due to the angular momentum recoupling of single neutron-proton configurations and not to the excitation of the single-particle states.

From the 'additivity' rule the magnetic moment for odd-odd nuclei can be calculated as (see Ames et al. (1961); Heyde (1990); Blin-Stoyle (1956))

$$\mu_I = \frac{1}{2}I(g_n + g_p) + \frac{(g_n - g_p)\left[I_n(I_n+1) - I_p(I_p+1)\right]}{2(I+1)} \tag{5.5}$$

under the assumption of weak coupling between protons and neutrons. One can use either Schmidt[2] (single particle) moments, or modified[3] single particle

[2]The single particle magnetic moment for $\pi(g_{9/2})$ is +6.74 $\mu_N$. The single particle magnetic moment for $\nu(g_{5/2})$ is -1.91 $\mu_N$. See Eq. 4.4 and Eq. 4.5.

[3]The modified gyromagnetic single particle value for $\pi(g_{9/2})$ is +1.412 $\mu_N$. Modified gyromagnetic single particle value for $\nu(g_{5/2})$ is -0.575 $\mu_N$. See Eq. 4.6.

**Table 5.3:** Comparison of calculated and experimental moments for $^{104g,m}$Ag. The nuclear magnetic moment values are given in $\mu_N$.

| Configurations | | $^{104m}$Ag ($I = 2^+$) $\mu_{exp} = +3.689(3)\mu_N$[5] | | | $^{104g}$Ag ($I = 5^+$) $\mu_{exp} = +3.918(2)\mu_N$[6] | | |
|---|---|---|---|---|---|---|---|
| Protons | Neutrons | $\mu_{sp}$ | $\mu_{sp}^{mod}$ | $\mu_{emp}$[7] | $\mu_{sp}$ | $\mu_{sp}^{mod}$ | $\mu_{emp}$[7] |
| $\pi(g_{9/2}^{-3})_{7/2}$ | $\nu(d_{5/2}^{-1})$ | 3.373 | 3.155 | 2.813 | 3.155 | 3.252 | 3.401 |
| $\pi(g_{9/2}^{-3})_{9/2}$ | $\nu(d_{5/2}^{-1})$ | 6.766 | 6.136 | 5.149 | 4.851 | 4.742 | 4.569 |

moments or also experimental values for the $g$-factor of neighboring odd-even nuclei, to determine respectively $\mu_{sp}$, $\mu_{sp}^{mod}$ and $\mu_{emp}$. The use of experimental $g$-factors from neighboring odd-even nuclei takes into account configuration mixing and possible $g$-factor quenching in the odd-$A$ nuclei. For the $g$-factor of the $g_{9/2}$ protons, $^{103}$Ag ($I^\pi = 7/2^+$) was used as this the nearest neighboring isotope, yielding 1.277(14) $\mu_N$ (see Raghavan (1989)). For the $g$-factor of the $d_{5/2}$ neutrons, we used the average value of $^{105}$Pd, $^{105}$Cd, $^{99}$Ru and $^{101}$Ru, i.e. -0.28(2) $\mu_N$. We then calculated the values for the $\mu_I$ listed in Table 5.3. It follows that the experimental magnetic moments for both the $I = 2^+$ and $I = 5^+$ states are in between the values of $\mu_{emp}$ calculated for the $7/2^+$ and the $9/2^+$ proton states coupled to the $5/2^+$ neutron state, with the moment for the $I = 2^+$ isomeric state being closer to the one calculated for the $\pi(g_{9/2}^{-3})_{7/2}\nu(d_{5/2}^{-1})$ configuration.

On the basis of the moment it appears that the $2^+$, $5^+$ doublet can be written in the form (see Noya et al. (1959)):

$$\psi(^{104m,g}\mathrm{Ag}) = \alpha\left[\pi(\mathrm{g}_{9/2}^{-3})_{7/2}\nu(\mathrm{d}_{5/2}^{-1})\right] + \sqrt{(1-\alpha^2)}\left[\pi(\mathrm{g}_{9/2}^{-3})_{9/2}\nu(\mathrm{d}_{5/2}^{-1})\right]. \quad (5.6)$$

The expectation value of the magnetic moment operator then becomes

$$\langle\mu\rangle = \alpha^2\left\langle\pi(g_{9/2}^{-3})_{7/2}\nu(d_{5/2}^{-1})\right\rangle + (1-\alpha^2)\left\langle\pi(g_{9/2}^{-3})_{9/2}\nu(d_{5/2}^{-1})\right\rangle, \quad (5.7)$$

where $\alpha^2$ is the mixing probability of the possible configurations. As a result, we can couple the mixed state to two 'relatively pure' configurations. Table 5.4

[5] $\beta$-NMR/ON, this work.
[6] $\gamma$-NMR/ON, this work.
[7] from values listed in Raghavan (1989) and Eq. 5.5.

**Table 5.4:** Coefficients for a possible configuration mixing of two 'relatively pure' wave function configurations that represent the observed nuclear magnetic moments of the $^{104g,m}$Ag isotopes.

| Isotope | Spin | Decoupling[8] [a] |
|---|---|---|
| $^{104g}$Ag | 5 | $0.75\left[\pi(g_{9/2}^{-3})_{7/2}\nu(d_{5/2}^{-1})\right] + 0.67\left[\pi(g_{9/2}^{-3})_{9/2}\nu(d_{5/2}^{-1})\right]$ |
| $^{104m}$Ag | 2 | $0.79\left[\pi(g_{9/2}^{-3})_{7/2}\nu(d_{5/2}^{-1})\right] + 0.61\left[\pi(g_{9/2}^{-3})_{9/2}\nu(d_{5/2}^{-1})\right]$ |

[a] Coefficients in the table are $\alpha$ and $\sqrt{1-\alpha}$, see Eq. 5.6.

**Table 5.5:** An overview of experimental magnetic moments for ground and isomeric states of $^{102,104}$Ag.

| $N$ | Isotope | Spin | $\mu$, $\mu_N$ | Reference |
|---|---|---|---|---|
| 55 | $^{102g}$Ag | 5 | +4.6(7) | Wannberg et al. (1970); Raghavan (1989)[b] |
| | | | +3.66(24) | Vandeplassche et al. (1983)[e] |
| | $^{102m}$Ag | 2 | +4.14(25) | Greenebaum and Phillips (1974)[b] |
| 57 | $^{104g}$Ag | 5 | +3.918(2) | this work[a] |
| | | | +3.914(8) | Van Walle (1985)[a] |
| | | | +3.919(3) | Dinger et al. (1989)[b] |
| | $^{104m}$Ag | 2 | +3.689(3) | this work[c] |
| | | | +3.7(1) | U. Köster[d] |
| | | | +3.7(2) | Ames et al. (1961)[b] |

[a] $\gamma$–NMR/ON result.
[b] Atomic beam magnetic resonance technique.
[c] $\beta$–NMR/ON result.
[d] Private communication, RILIS technique.
[e] LTNO technique.

presents coefficients for a possible configuration mixing of two 'relatively pure' wave function configurations that represent the observed nuclear magnetic moments of the $^{104g,m}$Ag isotopes. An overview of experimental magnetic moments for ground and isomeric states of $^{102,104}$Ag is given in Table 5.5.

[8] The coefficients presented here are very close to the ones obtained by Ames et al. (1961), who found for both isotopes of $^{104g,m}$Ag $\alpha \approx \frac{1}{\sqrt{2}}$. However, here we used more recent data. For decoupling we used experimental nuclear magnetic moments presented in Table 5.3.

# Chapter 6

# Isospin mixing

## 6.1 Introduction

A fundamental concept in hadron physics is isospin. In nuclear physics the concept of isospin was introduced by W. Heisenberg (Heisenberg (1932)) who considered protons and neutrons as different states of the same particle (the nucleon) because of the approximate charge independence of nuclear forces. Heisenberg introduced a variable $\tau$ which was later called the isotopic spin (and then was shortened to isospin). The value -1 of this variable was assigned to the proton state of the nucleon, the value +1 to the neutron state. The assumption that the forces between all pairs of particles are equal is equivalent, then, to the assumption that they do not depend on $\tau$ or that the Hamiltonian does not involve the isospin. The consequences of this symmetry of the nuclear Hamiltonian for the spectroscopy of nuclei were studied in detail in the work by Wigner (1937); Wigner and Feenberg (1941). However, it was assumed then that the concept of isospin seemed useful only for light nuclei. It was believed that as soon as the number of protons was increased considerably, the Coulomb interaction would break the isospin symmetry. Later, it was realized that the isospin concept can be generalized also for the heavier nuclei.

Ever since, isospin has been an important tool for the classification of nuclear

and hadronic states. Since charge independence is an approximate symmetry only, the isospin quantum numbers are consequently slightly mixed in reality. In general, isospin mixing in nuclei is caused:

- by the electromagnetic interaction,
- by the proton-neutron mass difference,
- and by the charge-dependent parts of the nuclear force.

The electromagnetic interactions are dominated by the Coulomb repulsion of the protons. However there are several other effects associated with the nucleon magnetic moments and the nucleon finite size (see e.g. Auerbach et al. (1972)). The proton-neutron mass difference also contributes to isospin mixing, since the nuclear Hamiltonian depends on the mass difference between protons and neutrons. The effect arises since the Hamiltonian includes a term which represents the total mass of all nucleons in the nucleus.

When discussing the isospin properties of nuclear forces one makes a distinction between *charge symmetry* and *charge independence*. One calls a force charge symmetric if there is no difference between the *p*-*p* and *n*-*n* interactions. A force is charge independent if the *p*-*p* and *n*-*n* interactions are equal to the $T = 1$, *n*-*p* interaction. However, the charge dependence of nuclear forces is well established. That is, the purely nuclear parts of the *p*-*p* force and the $T = 1$, *n*-*p* force differ from each other. The major effects which lead to a charge dependence of the nuclear forces are:

- the mass difference of the mesons exchanged between the nucleons, especially the mass difference between the charged and the neutral $\pi$-meson,
- radiative corrections, especially to the pion-nucleon coupling constant, and
- mixing of the meson states of different isobaric spin but with the same spin and parity, e.g., the $\pi^0$ meson and the $\eta$ meson.

The measurement of the size of isospin mixing in nuclei attracted a lot of interest in recent time. Moreover, additional impetus was given by the fact

that one can test the unitarity of the Cabibbo-Kobayashi-Maskawa (CKM) matrix by measuring super-allowed Fermi $\beta$-decay rates. Combining the average experimental value $\mathcal{F}t$ for the decay rates of these transitions it is possible to extract the mixing amplitude $V_{ud}$ between $u$ and $d$ quarks (Cabibbo (1963); Kobayashi and Maskawa (1973)) with high precision. Available data (Caso et al. (1998); Towner and Hardy (2003, 2002); Hardy and Towner (1975); Towner et al. (1977); Towner and Hardy (1973); Abele et al. (2004); Hardy and Towner (2005)) suggest that the CKM-matrix fails the unitarity test pointing to the existence of physics beyond the standard three-generation quark model for the electroweak interaction. These conclusions depend partly on corrections for nuclear isospin mixing which must be calculated with nuclear theory. In view of the present debate (e.g. Fuchs et al. (2000)) it is important to determine the size of isospin mixing directly from experiment.

## 6.2 Simple estimates of isospin impurities

The literature dealing with various theoretical models for isospin mixing is extensive. Here we would like to present only the final results of these calculations. Details can be found in the references cited below. In this section we deal with isospin impurities mainly in ground (or low-lying) states of nuclei. We are not concerned here with the total effect of charge symmetry violating forces $V_{\mathrm{CV}}$ on the properties of the ground state, but only with the admixture of isospin $T' \neq T_0$ where $T_0$ is the isospin quantum number of the ground state in the limit of $V_{\mathrm{CV}} \to 0$. (Clearly, the $V_{\mathrm{CV}}$ interaction also will change other properties of the ground state in addition to the quantum number $T$.)

The expression for the isospin admixture in first-order perturbation theory is

$$\alpha^2 = \sum_{\epsilon \neq 0} \frac{|\langle 0|V_{\mathrm{CV}}|\epsilon\rangle|^2}{(E_\epsilon - E_0)^2}, \tag{6.1}$$

where $|0\rangle$ denotes the $T = T_0$, $T_Z = T_0$ unperturbed ground state and the summation extends over all states $|\epsilon\rangle$ with $T' \neq T_0$. The Coulomb interaction is the dominant part of $V_{\mathrm{CV}}$, therefore, expression 6.1 is simplified by keeping only the isovector part of $V_{\mathrm{CV}}$ and hence only states with $T' = T_0 + 1$.

### 6.2.1 The Hydrodynamical Estimate

The estimate for the isospin impurity $\alpha_{T_0+1}$ given by Bohr and Mottelson (1998) is based on a hydrodynamical description of the isovector monopole state. The isovector monopole state is described as an oscillation of the neutrons fluid density against that of the protons. This is analogous to the Steinwedel-Jensen model (Steinwedel et al. (1950)) for a giant dipole. The boundary condition imposed is that the relative velocity of the proton and neutron fluids vanishes at the surface of the nucleus. For the $N = Z$ nuclei Bohr and Motelson obtained

$$\alpha^2_{T_0+1} = 5.5 \times 10^{-7} Z^{8/3}. \tag{6.2}$$

For nuclei with $N - Z = 2T > 0$, one has to multiply this expression by $(T_0 + 1)^{-1}$ and also introduce a correction due to the splitting of the two isospin components $(T_0, T_0 + 1)$ of the isovector monopole.

### 6.2.2 Sum-Rule Estimate

Assuming that the Coulomb strength is concentrated in a narrow energy region, and that the proton and neutron have homogeneous density distribution, one can use the closure approximation in Eq. 6.1 (a detailed explanation of the application of the sum rule and the closure approximation for the analog state can be found in Auerbach et al. (1972)) to write

$$\alpha^2_{T_0+1} = \frac{1}{T_0 + 1} \frac{5.3 \times 10^{-3} Z^3 A^{-2/3}}{(E_0 - E_M)^2}, \tag{6.3}$$

where the factor $(T_0 + 1)$ indicates that only $T + 1$ admixtures into the state with isospin $T_0$ are considered and $E_0$, resp. $E_M$ is the energy of the state with isospin $T_0$, resp. $T_0 + 1$. Using the hydrodynamical-model estimate and neglecting the symmetry energy correction (see details in Auerbach (1972))

$$E_0 - E_M \approx 170 A^{-1/3} \text{MeV}. \tag{6.4}$$

Eq. 6.3 then becomes

$$\alpha^2_{T_0+1} = \frac{1.8 \times 10^{-7} Z^3}{T_0 + 1}. \tag{6.5}$$

The ratio between this result and the one from the hydrodynamical model is $\frac{1}{3}Z^{1/3}$. The function $Z^{1/3}$ is slowly varying for medium- and heavy-mass nuclei and its range is 3 to 4.5. Therefore, this model is in fair agreement with the hydrodynamical-model predictions.

### 6.2.3 Energy Weighted Sum Rule (EWSR) estimate

The normal Random Phase Approximation (RPA) energy weighted distributions of strength of isobaric analogue states are related through the sum rule (see i.e. Liu and Brown (1976); Auerbach and Klein (1983) and references therein) to Hartree-Fock (HF) expectation values of double commutators of the relevant operators and the total hamiltonian. Auerbach (1983) utilize the linearly EWSR to calculate the isospin impurity. For $N > Z$ nuclei he estimated, within about 30% of accuracy, that

$$\alpha^2_{T_0+1} \simeq \frac{Z^2 A^{2/3}}{T_0 + 1} 6.8 \times 10^{-7}. \tag{6.6}$$

Again this isospin impurity dependence agrees well with the hydrodynamical model, but the coefficient is about a factor of two larger.

### 6.2.4 Estimate from the Model of Colò *et.al.*

Theoretical predictions for isospin mixing using HF calculations with Skyrme forces as well as RPA were carried out for a number of proton-rich $N \approx Z$ nuclei (e.g. Saw and Yap (1989); Sagawa et al. (1995, 1996); Dobaczewski and Hamamoto (1995); Hamamoto and Sagawa (1993); Ormand and Brown (1985, 1995)). They all give similar results, yielding isospin mixing that are a factor 2 to 3 larger than the values that were estimated by Bohr and Mottelson (1998), who used a spherical hydrodynamical model (see Eq. 6.2) and employed the polarization effect due to isovector monopole modes to extract the isospin mixing. In Dobaczewski and Hamamoto (1995) it was shown that the non-smooth dependence on $Z$ that was obtained for the ground states of the $N = Z$ nuclei when assuming spherical shell structure, is smoothed out when the deformation degree of freedom was induced in the HF calculations (see Fig. 6.1).

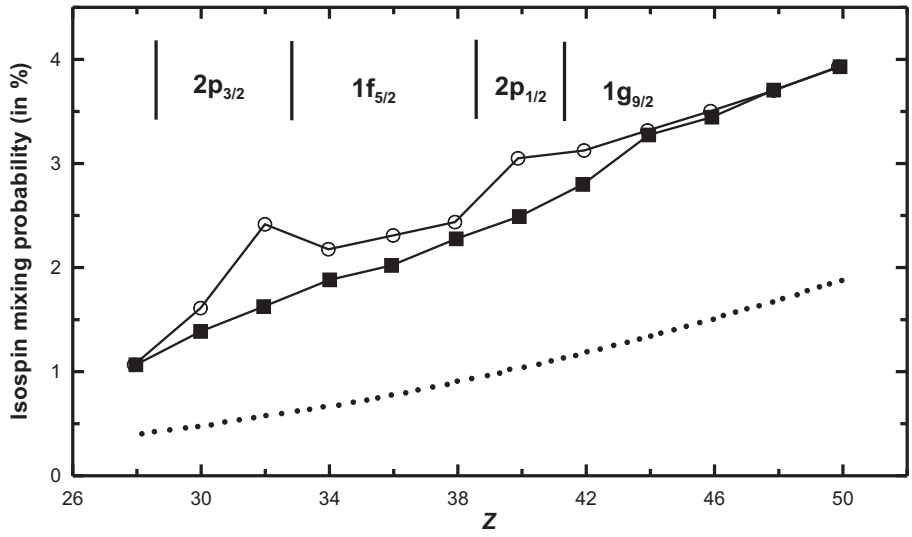


**Figure 6.1:** Isospin mixing probabilities $\alpha^2$ calculated using the HF approximation with the Skyrme SIII interaction for the $N = Z$ even-even nuclei from $^{56}$Ni to $^{100}$Sn. Values obtained from deformed HF solutions are shown by squares, while those from HF calculations constrained to spherical shapes are shown by open circles. The spherical one-particle orbitals, which are being filled in the constrained HF calculations as $N = Z$ increases, are indicated in the upper part of the figure. The dotted curve shows the result of Bohr and Mottelson (1998), where a spherical hydrodynamical model (see Eq. 6.2) is used and polarization effects due to the isovector monopole modes are employed to estimate the isospin mixing. Adopted from Dobaczewski and Hamamoto (1995).

In ref. Colò et al. (1995); Nagarajan et al. (1995) the admixture of states with isospin $T = T_0 + 1$ into the ground state with isospin $T_0$ was written as

$$\alpha^2_{T_0+1} = \frac{16.09}{T_0+1}\frac{N\cdot Z^3}{A^{7/3}}\frac{1}{\left[(E_0 - E_M) + \frac{4V_1(T_0+1)}{A}\right]^3} \tag{6.7}$$

with $(E_0 - E_M)$ the energy of the isovector giant monopole resonance (see Eq. 6.4), while $V_1 \approx 25$ MeV represents the neutron-proton exchange potential, and $E_0$ is the excitation energy (in MeV) of the state with isospin $T_0$. It is assumed that the admixture of components with $T > T_0 + 1$ can be neglected. Along the line of beta stability this isospin mixing probability $P$ is small due

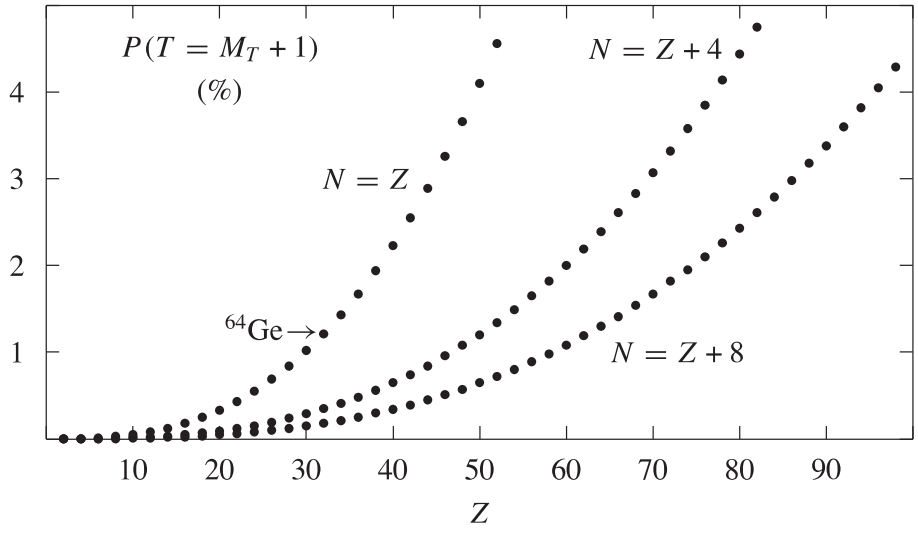


**Figure 6.2:** Calculated isospin mixing $P(T = M_T+1)$ (viz. $P(T = T_z+1)$ in our notation) in the ground state of even-even nuclei as a function of nuclear charge $Z$ for neutron numbers $N = Z, Z + 4$ and $Z + 8$ (adopted from Van Isaker (1999)).

to

1. the isospin factor $(T_0 + 1)^{-1}$, which is sometimes also called the geometrical quenching factor, and
2. the so-called analogue quenching factor $4V_1(T_0 + 1)/A$.

Both effects drastically quench the isospin mixing in nuclei with a neutron excess.

One way to look for isospin-mixing effects is to study the pairs of mirror nuclei, in which the number of proton and neutrons are interchanged. This leads to shifts between the excitations energies of a mirror pair, the so-called mirror energy differences, which are known to be precise and challenging probes of nuclear structure (Ekman et al. (2004)).

As it has been shown above, isospin mixing can be estimated in a variety

of nuclear models. They all show that the mixing is maximal in $Z = N$ nuclei and rapidly decreases with proton or neutron excess; in addition, the mixing increases with nuclear mass. This is illustrated in Fig. 6.2 (adopted from Van Isaker (1999)) where a simple estimate (see Colò et al. (1995); Nagarajan et al. (1995) and Eq. 6.7) of the admixture $P(T = T_z + 1) = \alpha^2$ in the ground state of even-even nuclei is plotted as a function of nuclear charge $Z$ for neutron numbers $N = Z, Z + 4$ and $Z + 8$. This quantity gives the square of the component with isospin $T = T_z + 1$ in the ground state of a nucleus with isospin projection $T_z$ . Isospin mixing effects, caused mainly by the Coulomb interaction, should thus be looked for in heavy $Z = N$ nuclei where they are largest.

## 6.3 Experimental Signature

In this work we search for isospin mixing by searching for a non-zero Fermi matrix element $M_F$ in isospin-forbidden beta-transitions between states of the same spin but different isospin i.e. $I^\pi \rightarrow I^\pi$ ($\Delta T \neq 0$). In the case of $0^+ \rightarrow 0^+$ ($\Delta T \neq 0$) beta-transitions the Fermi matrix element can be deduced from the log-$ft$ value alone. In the case of $I^\pi \rightarrow I^\pi$ ($I \neq 0$, $\Delta T \neq 0$) beta transitions, two measurements are needed to separate $M_F$ and $M_{GT}$, where $M_{GT}$ refers to the Gamow-Teller matrix element. These are usually the log-$ft$ value and either the $\beta - \gamma$ (circular polarization) correlation or the angular distribution of $\beta$-particles emitted from polarized nuclei. The early experiments were carried out mostly using the $\beta - \gamma$ (circular polarization) technique. An overview is given in Raman et al. (1975). However, this method often led to conflicting results for a single transition, mostly owing to the low efficiency of the method and large systematic errors that were not accounted for. Instead of the $\beta - \gamma$ (circular polarization) technique, the method of low temperature nuclear orientation now allows to determine the angular distribution of $\beta$-particles emitted from polarized nuclei with good precision and reliability (Schuurmans et al. (2000); Severijns et al. (2005)).

Recently, it has been demonstrated that the measurement of $E2/M1$ multipole mixing ratios of $\gamma$ transitions between exited states of heavy odd-odd $N = Z$ nuclei can be used as a source of information on the isospin mixing between

basis states of a chosen configurations space of valence nucleons (i.e. Lisetskiy et al. (2002); von Brentano et al. (2004)). However, this measurement depends on the minimal and robust theoretical input from the nuclear shell model calculations that were used to estimate Coulomb correction factors for super-allowed Fermi decays.

In recent times, the $N = Z$ nucleus $^{64}$Ge has been investigated in two experiments using the EUROBOLL III and EUROBALL IV spectrometers coupled to ancillary devices (Farnea et al. (2003)). Multipole mixing ratios, linear polarization and picosecond lifetimes for various transitions have been measured. The linear polarization results allowed to investigate the amount of isospin mixing implied by the presence of a forbidden $E1$ transition. This value is of the same order of magnitude as predicted by various theoretical calculations of isospin mixing in the ground states of even-even nuclei, i.e. Colò et al. (1995); Nagarajan et al. (1995) (see Fig. 6.2). However, we should stress here that in this work the total isospin mixing from all states with $T = T_0 + 1$ has been measured.

The formalism for isospin-forbidden $I^\pi \rightarrow I^\pi$ Fermi transitions was explained in detail in Raman et al. (1975). Here, we will briefly outline the main parts of it and, moreover, limit to $\beta^+$-transitions with $T_3 \equiv (N - Z)/2 > 0$.

The general decay scheme for isospin-forbidden $\beta^+$-transition is given in Fig. 6.3. According to this figure the wave function of the initial and final state connected by the $\beta^+$-transition may be written as

$$\begin{aligned} |i\rangle &= |I : I^\pi, T = T_0, T_3 = T_0\rangle + \\ &+ \alpha_{T_0+1}|A : I^\pi, T = T_0 + 1, T_3 = T_0\rangle + \\ &+ \sum_{n>1} \beta_n |I^\pi, T = T_0 + n, T_3 = T_0\rangle \\ |f\rangle &= |F : I^\pi, T = T_0 + 1, T_3 = T_0 + 1\rangle \end{aligned} \tag{6.8}$$

where $T = T_3$ was used for nuclear ground states and the analog state with $T = T_0 + 1$ is mixed with small mixing amplitude $\alpha_{T_0+1}$ into the initial state $I$. The terms with coefficient $\beta_n$ represent admixtures of states with $T = T_0+n$ $(n > 1)$. Note that $\alpha_{T_0+1}$ in Eq. 6.8 is the mixing amplitude of the analog state only. Thus, $\alpha^2_{T_0+1}$ does not represent in this case the total isospin impurity of the initial state, but only a fraction of it, i.e. the isospin admixture of the

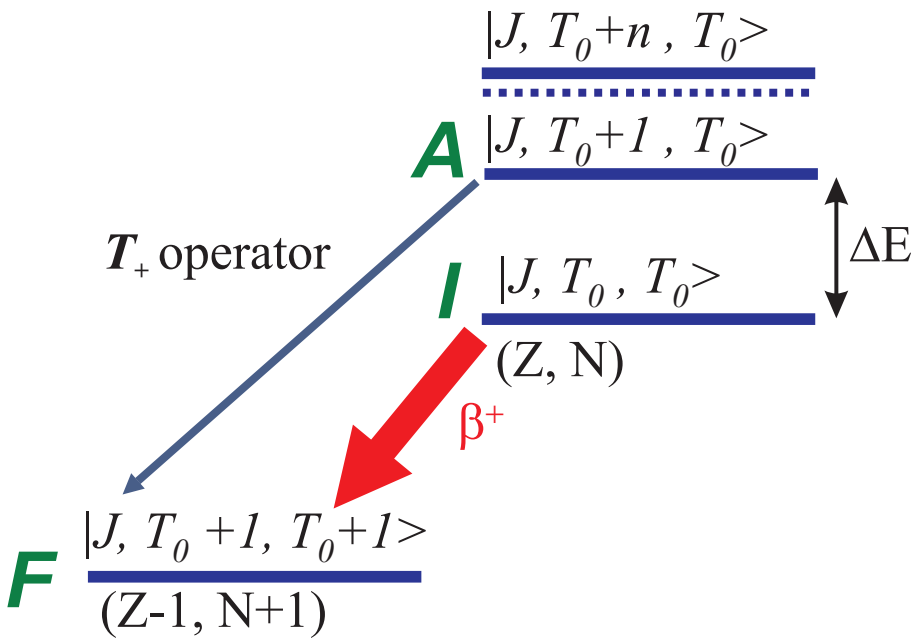


**Figure 6.3:** General decay scheme for a isospin-forbidden $\beta^+$- transition with given spin and isospin for the initial ($I$), final ($F$) and analog ($A$) levels.

analog state of the daughter state of the $\beta^+$-decay (see Fig. 6.3). However, it is believed that it has the biggest contribution into the initial state, since the other states (with isospin $T \neq T_0$) lie much higher and therefore have less probability to be mixed in it. The total isospin impurity must be obtained by considering the admixtures of all $T \neq T_0$ states into the $T_0$ state. In addition, we do not consider possible isospin mixing in the final state, because it can only come from states with isospin $T_0 + 2$ which cannot be probed by Fermi $\beta$-decay.

The Fermi matrix element is given by

$$\begin{aligned} M_F \equiv \langle f|T_+|i\rangle &= \alpha_{T_0+1}\sqrt{T^{(A)}(T^{(A)}+1) - T_3^{(A)}(T_3^{(A)}+1)} \\ &= \alpha_{T_0+1}\sqrt{(T_0+1)(T_0+2) - T_0(T_0+1)} = \alpha_{T_0+1}\sqrt{2(T_0+1)} \end{aligned} \tag{6.9}$$

where the superscript $(A)$ refers to the analog state. Measuring $M_F$ thus directly yields the isospin mixing amplitude $\alpha_{T_0+1}$. Experimentally this is done by comparing the $ft$-value for the $\beta$-transition investigated ($ft$), to the nucleus independent $ft$-value for the superallowed $0^+ \rightarrow 0^+$ pure Fermi $\beta$-transitions (i.e. $\mathcal{F}t^{0^+\rightarrow 0^+}$=3072.2(9) s (Towner and Hardy (2003, 2002); Hardy and Towner (1975); Towner et al. (1977); Towner and Hardy (1973); Abele et al. (2004); Hardy and Towner (2005))):

$$ft = \frac{2(G_V)^2 \mathcal{F}t^{0^+\rightarrow 0^+}}{(G_V M_F)^2 + (G_A M_{GT})^2} \tag{6.10}$$

and combine this ratio with the Fermi/Gamow-Teller (F/GT) mixing ratio $y$ of the $\beta$-transition investigated

$$y = \frac{G_V M_F}{G_A M_{GT}}. \tag{6.11}$$

Here $G_V$ ($G_A$) is the vector (axial-vector) coupling constant. Using Eqns. 6.9 to 6.11 one then finds the isospin mixing probability

$$\alpha^2_{T_0+1} = \frac{y^2}{(1+y^2)(1+T_0)} \frac{\mathcal{F}t^{0^+\rightarrow 0^+}}{ft}. \tag{6.12}$$

The F/GT-mixing ratio $y$ (assuming only one $\beta$-branch contribute to the decay) can be extracted from the asymmetry parameter[1] $A_1$ that is obtained by observing the $\beta^+$-emission asymmetry from oriented nuclei:

$$A_1 = \frac{1}{1+y^2} \left[ \frac{-1}{\sqrt{3I(I+1)}} + \frac{2}{\sqrt{3}} y \right] \tag{6.13}$$

with $I$ the initial state of the $\beta$-transition. Fig. 6.4 shows the behaviour of the difference between the asymmetry parameter for pure a GT transition and for the case where in addition a Fermi component is present in the $\beta$-decay. It is seen that even a small admixture of a Fermi component considerably changes the asymmetry parameter. The low-temperature nuclear orientation method that allows to measure directly the asymmetry parameter is thus a very sensitive method to investigate isospin impurities.

[1] Here we rewrite Eqn. 1.19 without factor $\frac{v_\beta}{c}$, since we would like to be independent of $\beta$-particle energy.

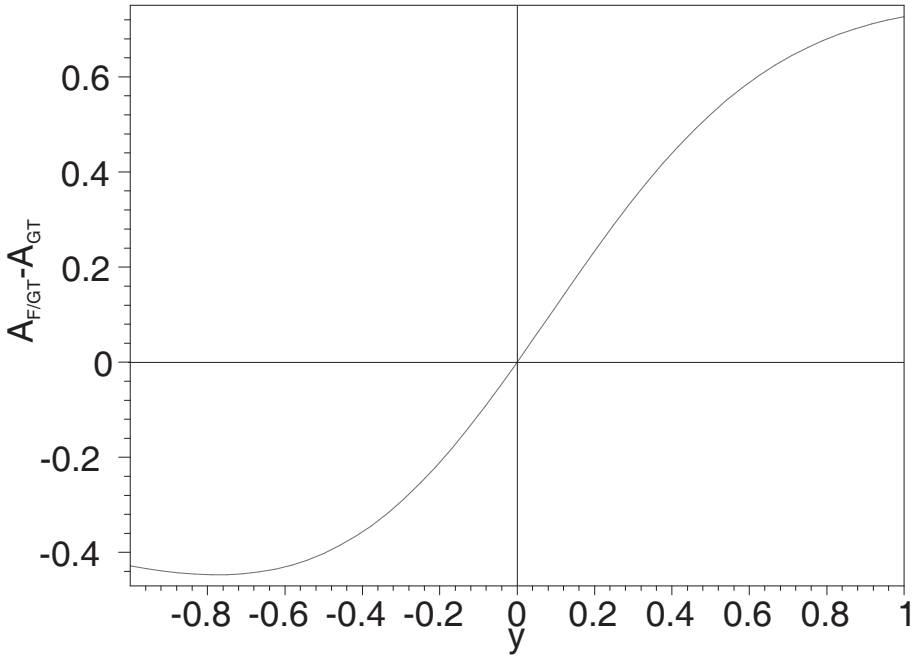


**Figure 6.4:** The difference between the asymmetry parameter with the presence of a Fermi component and the asymmetry parameter for a pure GT transition as a function of the F/GT-mixing ratio $y$, for a nuclear spin $I = 3/2$.

If all charge-dependent terms in the nuclear Hamiltonian are denoted by $V_{CV}$ (see Eq. 6.1), the admixture amplitude $\alpha_{T_0+1}$ can be shown through first-order perturbation theory (Raman et al. (1975)) to be

$$\alpha_{T_0+1} = \frac{\langle i|V_{CV}|A\rangle}{\Delta E}, \tag{6.14}$$

where $\Delta E$ is the energy difference between the initial $i$ and analog $A$ states (see Fig. 6.3). The $\Delta E$ can be expressed in terms of the Coulomb displacement energy $\Delta E_c$, the end-point energy of the $\beta$-transition and the neutron-proton mass difference,

$$\begin{aligned} \Delta E =& \Delta E_c + E_{\beta^-} - 782 \text{ keV} && \beta^-\text{-decay} \\ \Delta E =& \Delta E_c - (E_{\beta^+} + 1022) - 782 \text{ keV} && \beta^+\text{-decay} \end{aligned} \tag{6.15}$$

$\Delta E_c$ could be obtained either from experiment (Courtnay and Fox (1975)) or from the semiempirical formula discussed by Anderson et al. (1965).

# Chapter 7

# Isospin mixing in the $T = 1/2$ ground state of $^{59}$Cu

## 7.1 Experiment

As was mentioned before, the isospin impurity can be obtained by combining the experimental $ft$-value for a $\beta$-transition with a measurement of the asymmetry parameter $A_1$ using the LTNO method. However, in order to extract $A_1$ from the angular distribution of positrons emitted in $\beta$-decay from oriented nuclei the orientation parameter $B_1$ as well as the fraction $f$ should be known very precisely. Therefore, apart from the temperature dependent nuclear orientation measurement, we also performed a $\beta$-NMR/ON experiment in order to deduce a precise value for the nuclear magnetic moment of $^{59}$Cu (see i.e. Golovko et al. (2004)). The details of this experiment were outlined in Chapter 3.

In order to deduce the fraction for Cu implanted in Fe, a nuclear orientation experiment with $^{62}$Cu was carried out. However, during implantation of the $^{62}$Cu ions into the Fe-foil it was found that we also were implanting a stable beam of the same mass (i.e. aluminium chloride $AlCl$) thereby reducing the initial fraction due to a too high implantation dose[1]. We therefore repeated

[1]The fraction $f$ of nuclei in good sites decreases for higher doses (see e.g. Herzog (1986)

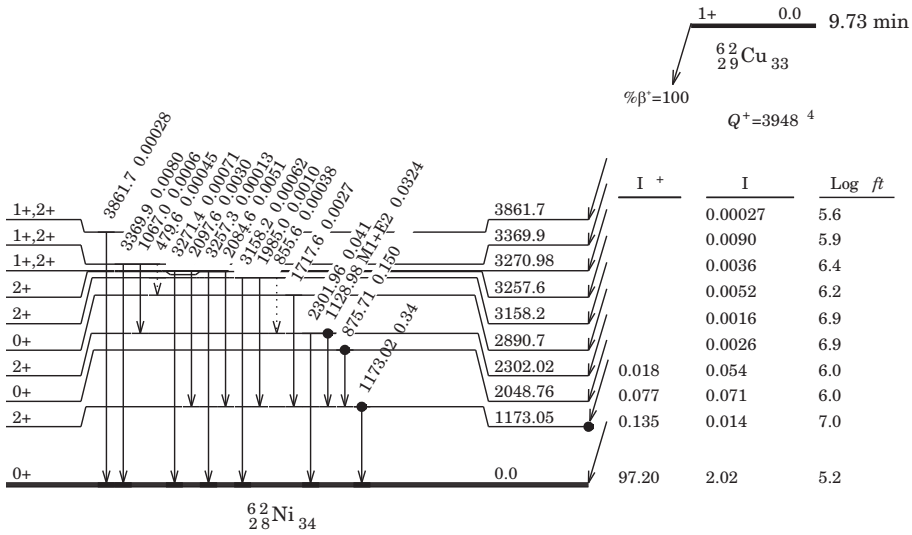


**Figure 7.1:** Levels in $^{62}$Ni populated in the $\beta^+$-decay of $^{62}$Cu (adopted from Firestone (1996)).

the nuclear orientation experiment on $^{59}$Cu and used only the data of this second measurements for analysis. However, the production rate of $^{59}$Cu from the target was much smaller then, compared to the initial experiment. These two facts explain the rather low $f$-value and the rather large error bar on the asymmetry parameter $A_1$ for $^{59}$Cu (see below). Full details on the production of $^{59}$Cu at ISOLDE/CERN and on the detector arrangement can be found in Chapter 3 and in Golovko et al. (2004).

### 7.1.1 $^{62}$Cu experiment: fraction measurement

The $\beta^+$-decay of $^{62}$Cu was used to deduce the fraction $f$ of the nuclei that feel the full orienting interaction. The decay scheme for $^{62}$Cu is presented in Fig. 7.1 (adopted from Firestone (1996)). As can be seen, the $\beta^+$-decay of $^{62}$Cu proceeds almost completely to the ground state of $^{62}$Ni via a $1^+ \rightarrow 0^+$ allowed pure Gamow-Teller $\beta^+$-transition (see Fig. 7.1). The magnetic moment of $^{62}$Cu

and references therein). Since ions of *AlCl* have the same atomic mass as $^{62}$Cu they can be present as a background current in the beam with the isotope of interest, thereby reducing the implantation fraction.

is $\mu = -3.380(4)\ \mu_N$ as has been determined with the atomic-beam magnetic-resonance method by Phillips and Jackson (1968). The hyperfine field for Cu in Fe is $B_{hf} = -21.8(1)$ T (i.e. Khoi et al. (1975)). As all $\gamma$-rays in the decay of $^{62}$Cu are too weak to determine the fraction $f$ with good precision from the anisotropy in their angular distribution, the $\beta^+$-decay was used for this. In the analysis, the low energy part of the $\beta^+$-spectrum, i.e the region below 1241 keV was not taken into account since below this energy the $\beta$-spectrum contained background from Compton scattered 511 keV $\gamma$-rays, while in addition the influence of the external magnetic field on the trajectory of the $\beta$-particles is more important here too, compared to the spectrum endpoint. The part of the $\beta$-spectrum between 2205 keV and the endpoint at $E_{end} = 2926$ keV was also not taken into account since above this energy the number of $\beta$-particles was rather small such that the results turned out to be very sensitive to the way the $\gamma$-background was handled (see Chapter 2 for more details).

Fig. 7.2 shows results of the fits for the fraction in 8 energy bins (see also Fig. 7.3) ranging from about 1000 keV to the endpoint of 2926 keV for different treatments of the $\gamma$-background. It should be mentioned here that in the fits we used a constant value for the solid angle correction $Q_1 = 0.97$ for each energy bin presented in the figure. Moreover, the data were not corrected for relaxation effects. In these fits the three sets of the points indicate data *i*) without $\gamma$-background corrections ("crosses"), *ii*) with $\gamma$-background corrections, where a constant background equal to the average count rate in 25 channels above the endpoint energy was subtracted ("squares"), and *iii*) with the subtracted $\gamma$-background being equal to the average count rate of 30 channels ("diamonds"). It is clear that for the three highest energy bins, with only low $\beta$ count rate, the results depend critically on the amount of $\gamma$-background subtracted. It was therefore decided to continue the analysis using further only the four energy bins ranging from 1241 keV to 2205 keV.

Fig. 7.3 shows the "warm" (i.e. no orientation) sum $\beta^+$-spectrum of $^{62}$Cu obtained with one of three HPGe particle detectors installed inside the 4 K radiation shield of the NICOLE refrigerator. The 511 keV $\gamma$-line, the Compton edge of the 511 keV $\gamma$-line, the $\beta^+$-spectrum endpoint at 2926 keV, and pulser peak are indicated. The part of the $\beta^+$-spectrum that was used for further analysis is indicated as well.

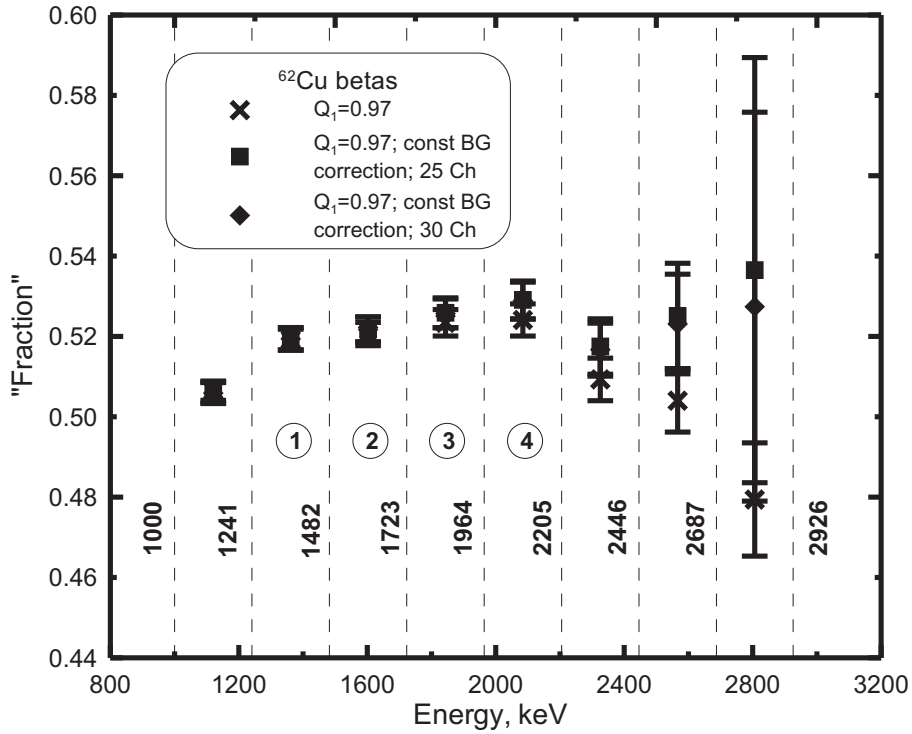


**Figure 7.2:** Results of the fits for the fraction in 8 energy bins (see Fig. 7.3) ranging from about 1000 keV to the endpoint of 2926 keV for different treatments of the $\gamma$-background. Note that "fraction" does not correspond to the fraction $f$ which gives the implantation quality as no correction for spin-lattice relaxation was included here.

Table 7.1 list the $Q_1$-factors, calculated with the GEANT4 code, for the four energy bins in the region from 1241 keV to 2205 keV and for the two particle detectors installed at opposite sides of the sample (i.e. at 15° and 165°). The details of these calculations are outlined in Chapter 2. The uncertainties take into account the precision to which the detector geometry was determined, various scattering effects, the presence of the external magnetic field (taken to be uniform in space) as well as the Monte Carlo statistical error. The largest contribution comes from the statistical error.

In determining the $\beta$-anisotropies for the different energy regions care was taken to subtract the $\gamma$-background under the $\beta$-spectrum. First of all the

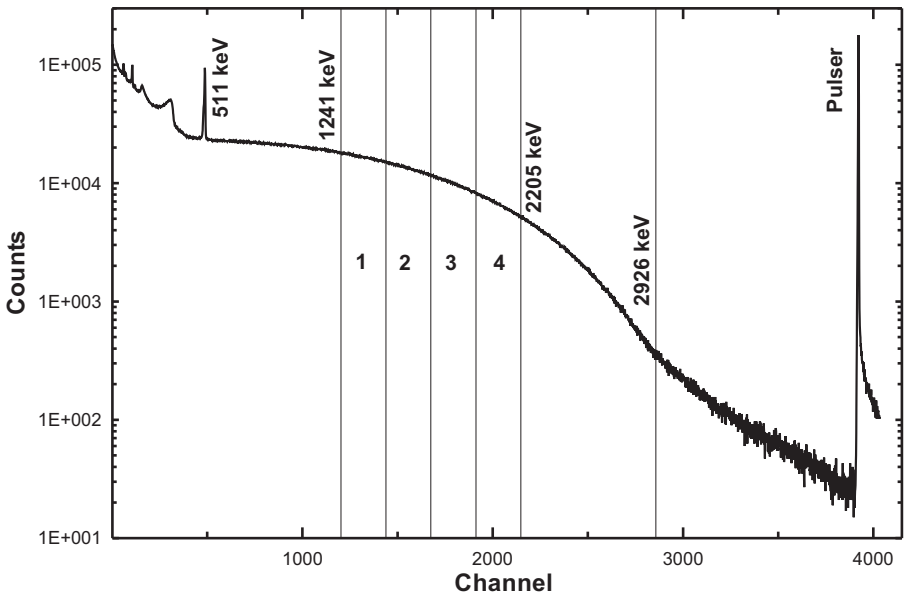


**Figure 7.3:** "Warm" (i.e. no orientation) sum $\beta^+$-spectrum of $^{62}$Cu obtained with one of three HPGe particle detectors installed inside the 4 K radiation shield. The 511 keV $\gamma$-line, the $\beta^+$-spectrum endpoint at 2926 keV and the pulser peak are indicated. The part of the $\beta^+$- spectrum that was used for analysis is the region between 1241 keV and 2205 keV, which was subdivided in four energy bins.

absolute efficiencies for the detection of $\gamma$-rays in the energy region of interest did not exceed a few percent (Severijns et al. (2005)). In addition a constant background substraction was performed for all data files. The subtracted value was deduced from the energy region above the endpoint of the $\beta^+$-spectra. Most of the registered events in this region are due to pile-up of the $\beta^+$-particles with 511 keV $\gamma$-quanta (there were no higher-energy radioactive contaminations in the beam).

The temperature of the sample was measured using nuclear thermometry (see i.e. Marshak (1986)), namely from the anisotropy of 136 kev $\gamma$-line of $^{57}$Co$\underline{\text{Fe}}$. The fraction of this thermometer was deduced from a separate nuclear orientation experiment, where as a calibration source the anisotropy of the 1332 keV $\gamma$-line of $^{60}$Co$\underline{\text{Co}}$ (single crystal) was used. The thermometer fraction was obtained as $f_{^{57}\text{Co}\underline{\text{Fe}}} = 1.00 \pm 0.01$. The solid angle correction factors for the

**Table 7.1:** $Q_1$-factors calculated with GEANT4 for the 15° and 165° particle detectors in four energy bins in the $\beta^+$-spectra of $^{62}$Cu, ranging from 1241 keV to 2205 keV.

| | $E$-energy, keV | | | |
|---|---|---|---|---|
| | $E_1$ | $E_2$ | $E_3$ | $E_4$ |
| | 1241-1482 | 1482-1723 | 1723-1964 | 1964-2205 |
| | $Q$-factors, 15° detector | | | |
| | $Q_{E_1}$ | $Q_{E_2}$ | $Q_{E_3}$ | $Q_{E_4}$ |
| $Q_1$ | 0.8537 | 0.8989 | 0.9279 | 0.9349 |
| $\Delta Q_1$ | 0.0040 | 0.0073 | 0.0098 | 0.0067 |
| | $Q$-factors, 165° detector | | | |
| | $Q_{E_1}$ | $Q_{E_2}$ | $Q_{E_3}$ | $Q_{E_4}$ |
| $Q_1$ | 0.8658 | 0.9182 | 0.9401 | 0.9627 |
| $\Delta Q_1$ | 0.0136 | 0.0029 | 0.0060 | 0.0059 |

136 keV line of the thermometer, $Q_2$ and $Q_4$, were determined according to the procedure outlined in Krane (1972), adopted for Monte Carlo calculations. This yielded $Q_2 = 0.960(3)$ and $Q_4 = 0.872(7)$. Since all other parameters which determine the anisotropy of the 136 keV $\gamma$-line in the decay of $^{57}$Co are well known, the temperature could be determined in a unique way from the measured anisotropy and Eqn. 1.3.

The observed $\beta^+$-asymmetry was fitted for the fraction and the spin-lattice relaxation constant. This was done via the attenuated orientation coefficient[2] $\rho_1$ (which is the ratio of the observed orientation parameter $B_1$(sec) relative to the thermal equilibrium orientation parameter $B_1$(th)). The $\rho_1$ coefficients were determined according to the procedure outlined in Vénos et al. (2003), adopted for **C**++ calculations and fully taking into account the observed temperature for each individual data point. Fig. 7.4(a) shows the fit result for the $W(15°)/W(165°)$ anisotropy as a function of inverse temperature in the

[2] Shaw and Stone (1988); Shaw and Stone (1989) tabulated attenuation coefficients for $B_{2,4}$. Recently, Vénos et al. (2003) extended those tables to include also terms with $B_{1,3,6,8}$.

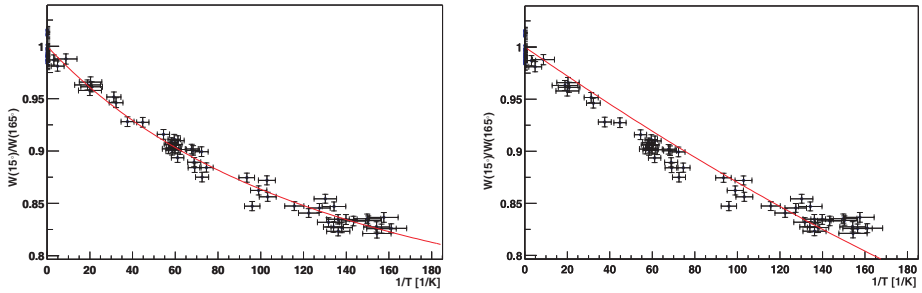


(a) with $C_K$ (b) without $C_K$

**Figure 7.4:** The $W(15^\circ)/W(165^\circ)$ anisotropy as a function of inverse temperature in the $^{62}$CuFe $\beta^+$-decay for the energy region from 1482 keV to 1723 keV (bin 2 in Fig. 7.3). For the left figure (a) the fit was done taking into account $C_K$, while for the right figure (b) it was not taken into account. Correction for incomplete relaxation was clearly required in this case.

$^{62}$CuFe $\beta^+$-decay for one of the energy bins indicated in Fig. 7.3. The results obtained for $C_K$ and $f$ from the four energy bins are listed in Table 7.2. The weighted average value for the relaxation constant $C_K$ in the decay of $^{62}$Cu, is

$$C_K[^{62}\mathrm{Cu}] = 4410 \pm 151\,\mathrm{s}\cdot\mathrm{mK}. \tag{7.1}$$

Using then the relation between the $C_K$ factors and the g-factors for two isotopes of the same element (Eqn. 1.12) and, taking into account the nuclear magnetic moments of $^{62}$Cu (i.e. $\mu(^{62}\mathrm{Cu}) = -0.380(4)\,\mu_\mathrm{N}$, Phillips and Jackson (1968)) and of $^{59}$Cu (i.e. $\mu(^{59}\mathrm{Cu}) = +1.891(9)\,\mu_\mathrm{N}$, Golovko et al. (2004) and Chapter 3 of this work) one finds

$$C_K[^{59}\mathrm{Cu}] = 401 \pm 14\,\mathrm{s}\cdot\mathrm{mK}. \tag{7.2}$$

This value is reasonably close to $C_K[^{59}\mathrm{Cu}] = 576 \pm 48\,\mathrm{s}\cdot\mathrm{mK}$ which one obtains from Eqn. 1.12 using the relaxation constant for $^{63}$Cu in iron ($C_K[^{63}\mathrm{Cu}] = 417 \pm 35\,\mathrm{s}\cdot\mathrm{mK}$) that was measured also in an external field of 0.1 T by Kontani et al. (1972). The same authors showed that the nuclear relaxation constant of the 3*d*- and the 4*d*-series impurities (i.e. V, Co, Cu, and Nb) dissolved in Fe depends on the external field strength. For Fe foil samples they also found that the relaxation constant can change drastically (by about a factor of two) if the external field is raised from 0.05 till 0.2 T. Since their measurements were

**Table 7.2:** Results for the relaxation constant $C_K$ and the $f$-factors when fitting the $W(15°)/W(165°)$ $\beta$-anisotropies of $^{62}$CuFe for the different energy regions. The results are given for four energy bins in the $\beta^+$-spectrum of $^{62}$Cu, in the region from 1241 keV to 2205 keV.

| | $E_1$ | $E_2$ | $E_3$ | $E_4$ |
|---|---|---|---|---|
| $f$ | 0.697(15) | 0.639(15) | 0.675(18) | 0.655(21) |
| $C_K$, s·mK | 4544(266) | 4047(269) | 4840(335) | 4311(374) |

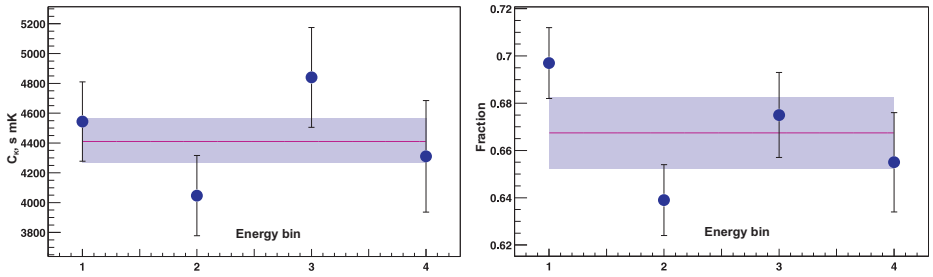


(a) $C_K$ (b) $f$

**Figure 7.5:** Overview of the fit results for $C_K$ (a) and for the fraction $f$ (b) for all four $\beta$ energy bins of $^{62}$CuFe. The values are also listed in Table 7.2. The band represents the weighted average.

made at liquid helium temperature, while our results were obtained in the mK region we will further use our own result for $C_K$, i.e. Eq. 7.1.

The weighted average for the fraction $f_{^{62}\text{CuFe}}$ is

$$f_{^{62}\text{CuFe}} = 0.667 \pm 0.014. \tag{7.3}$$

This value for the fraction will be used for analysis of the data for the $^{59}$Cu.

### 7.1.2 $^{59}$Cu experiment: isospin admixture

After the measurement with $^{62}$Cu we switched again to $^{59}$Cu. However, the production rate of $^{59}$Cu was now much less than in the beginning of the experiment leading to larger statistical error bars, as well as to a larger scattering of

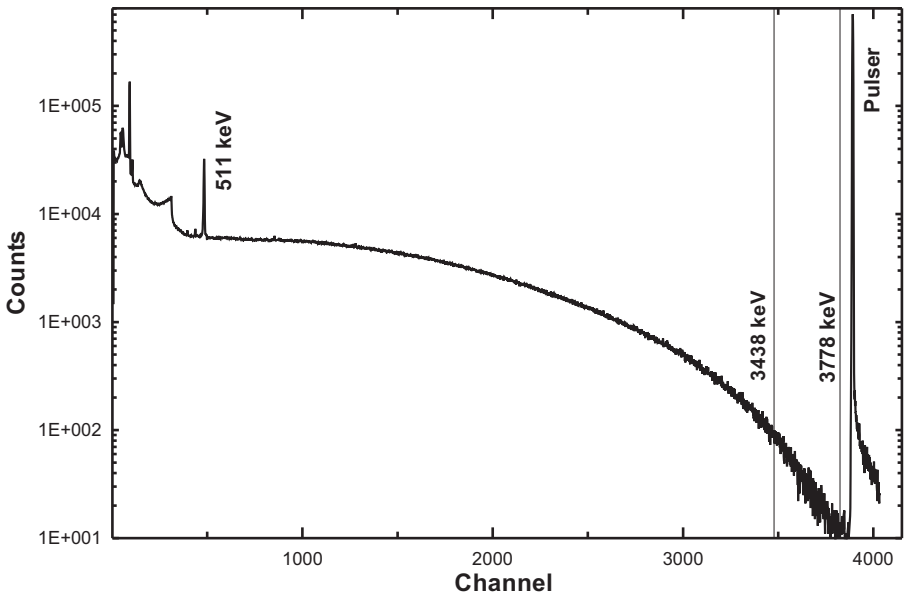


**Figure 7.6:** "Warm" (i.e. no orientation) sum $\beta^+$-spectrum of $^{59}$Cu obtained with the 15° particle detector installed inside the 4 K radiation shield. The parts of the $\beta^+$-spectra used for the determination of the isospin mixture in $^{59}$Cu as well as the endpoint energy are indicated.

the data points around the fitted curve. Fig. 3.2 in Chapter 3 shows a typical $\beta^+$-spectrum for $^{59}$Cu recorded in 150 s. Fig. 7.6 shows the sum spectrum of all 'warm' $\beta^+$spectra of $^{59}$Cu with the energy region that was used for the analysis indicated.

For the analysis of the $\beta^+$-spectra of $^{59}$Cu, we used only the last 339 keV in the $\beta^+$-spectra of $^{59}$Cu. This energy region was chosen since it contains only $\beta^+$-particles from the main decay branch of $^{59}$Cu (see Fig. 3.1) and positrons with energies close to the endpoint energy are scattered less. The $\beta^+$-spectra of $^{59}$Cu were corrected for the presence of Compton $\gamma$-rays, by subtracting a constant background of one count per channel as obtained from the background just above the $\beta^+$-endpoint (see Fig. 7.2). The values for the solid angle correction factors $Q_1$ for the energy bin in the region between 3438 and 3778 keV were calculated with the GEANT4 program. The details of these calculations are given in Chapter 2. The $Q_1$ factors for the 15° and 165° particle detectors

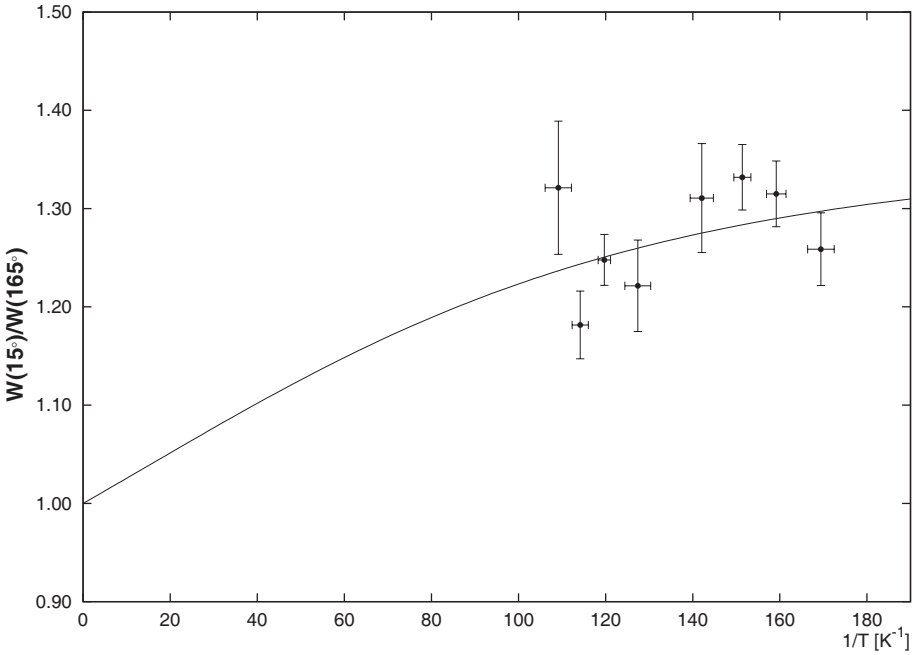


**Figure 7.7:** The $W(15°)/W(165°)$ anisotropy as a function of inverse temperature in the $^{59}$CuFe $\beta^+$-decay for the energy bin from 3438 to 3778 keV.

are found to be 1.0025(57) and 1.0031(70) respectively, where the error is the statistical error.

The $\frac{v}{c}$ factor calculated for the energy bin from 3438 to 3778 keV in the $\beta^+$-spectra of $^{59}$Cu is found to be 0.9920 (see Eq. 1.25). This value corresponds to the $\beta^+$-energy of 3539 keV that represents the weighted average energy for the chosen energy bin in the warm $\beta^+$ sum spectrum of $^{59}$Cu. It was checked that, within the precision of the energy calibration (i.e. a few keV) and the energy resolution (i.e. about 5 keV) for the particle detectors, the $\frac{v}{c}$ factor does not change too much. Indeed, an uncertainty of 16 keV corresponds to a change of $\frac{v}{c}$ in the last digit only (i.e. $\frac{v}{c}|_{3555\,\mathrm{keV}} = 0.9921$ and $\frac{v}{c}|_{3523\,\mathrm{keV}} = 0.9919$).

The evaluation of our nuclear orientation measurement, using the previously determined nuclear magnetic moment value $\mu[^{59}\mathrm{Cu}]$, the $C_K[^{59}\mathrm{Cu}]$ value, the fraction $f$, and the solid angle corrections $Q_1$, yields the value

$$A_1[^{59}\mathrm{Cu}] = -0.228 \pm 0.012. \tag{7.4}$$

**Table 7.3:** Total error account in units of $10^{-4}$ for $A_1[^{59}\mathrm{Cu}]$ including the statistical error, and the different systematic errors related to the fitting procedure. The statistical error includes the $S$-factor (see appendix B).

| source | statistics[a] | $\frac{v}{c}$ | $T_{\mathrm{int}}$ | $C_K$ | $Q_1$ | $f$ | total |
|---|---|---|---|---|---|---|---|
| error | 100 | 1 | 9 | 18 | 20 | 49 | 115 |

[a] See appendix B for the statistical procedure.

Fig. 7.7 shows the fit of the $W(15°)/W(165°)$ anisotropy as a function of inverse temperature in the $^{59}$CuFe $\beta^+$-decay for the selected energy bin. The total systematic error account is given in Table 7.3. The systematic error due to the uncertainty on the interaction temperature $T_{\mathrm{int}} = 10.029(65)$ mK, takes into account the uncertainty on the nuclear magnetic moment of $^{59}$Cu as well as the uncertainty on the hyperfine field of copper in iron. Since we used in the fit only the $\beta^+$-particles close to the endpoint, the largest contribution in the total error comes from statistics. However, in this way we are sure that there are no other contributions in the $\beta$-asymmetry from various $\beta^+$-branches in the decay of $^{59}$Cu.

## 7.2 Conclusion and Discussion

The result for $A_1[^{59}\mathrm{Cu}]$ corresponds to a F/GT mixing ratio of either $y = -5.1(3)$ or $y = 60(10) \cdot 10^{-3}$. The largest value was not considered as it would translate into the presence of a huge Fermi contribution in this supposedly almost pure Gamow-Teller $\beta^+$-decay of $^{59}$Cu. Combining this mixing ratio with the known log $ft$-value of 5.030(4) (see van Patter et al. (1973); Sen et al. (1977)) and using Eqs. 6.13 and 6.9, the isospin mixing amplitude and corresponding Fermi matrix element are found to be $|\alpha_{T_0+1}| = 8.3(13) \cdot 10^{-3}$ ($\alpha^2_{T_0+1} = 70(20) \cdot 10^{-6}$) and $|M_F| = 14(2) \cdot 10^{-3}$. This result is significantly smaller than the total isospin impurity mixing from all states with $T_0 + 1$ that can be estimated with Eq. 6.7 (i.e. $\alpha^2 = P[^{59}\mathrm{Cu}] \approx 6.16 \cdot 10^{-3}$; see Chapter 6). Following the idea of Auerbach (1983) one can estimate the total $T_0 + 1$ isospin mixing also via a fit formula that has been obtained with TDA and

RPA calculations for a series of nuclei through the periodic table, i.e.

$$P_{\mathrm{TDA/RPA}}(T = T_0 + 1) = \frac{4.3 \cdot 10^{-6}}{T_0 + 1} \frac{Z^3}{A^{2/3}}, \tag{7.5}$$

yielding $P_{\mathrm{TDA/RPA}}[^{59}\mathrm{Cu}] \approx 5.77 \cdot 10^{-3}$. Both formulas thus give similar results. It is to be noted though that our method only yields the isospin impurity in the ground state (with $T = T_0$) of this $\beta$-decay, coming from the mixing of the analog state of the final (daughter) state, and not from all states with isospin $T_0 + 1$ .

# Chapter 8

# Isospin mixing in the $T = 5$ isomeric state of $^{104}$Ag

## 8.1 Experiment

This experiment was carried out during the same run in which the NMR/ON experiment to determine the nuclear magnetic moment of of $^{104m}$Ag was performed. The experimental arrangement was thus the same in both experiments (see Chapter 5). Note the main goal of the NMR/ON experiment was to determine the moment of $^{104m}$Ag with sufficiently good accuracy (Golovko et al. (2005a)) that it would not be a limiting factor for the accuracy of the isospin-mixing in $^{104m}$Ag. As it will be shown later the contribution from the nuclear magnetic moment uncertainty into the final error bar for the isospin mixing is almost negligible compared to other sources of systematic errors. The experimental procedure to determine isospin impurities using the LTNO method was outlined in Chapter 6. As was mentioned before, one needs to determine in addition also the fraction of the implanted nuclei at good lattice sites with a good precision. Contrary to the $^{59}$Cu experiment where it was necessary to perform an LTNO experiment on $^{62}$Cu to determine this fraction, the decay of $^{104g}$Ag has suitable $\gamma$-lines that can be used for this. The ISOLDE facility

produces $^{104g,m}$Ag by the decay of $^{104}$Cd. Full details on the production of $^{104g,m}$Ag at ISOLDE/CERN can be found in Chapter 5 and in Münnich et al. (1971).

To deduce the isospin impurity we performed three different experiments (these will further be called *run A*, *run B*, and *run C*). In the next section all aspects to determine the fraction for each run will be discussed. Thereafter the determination of the isospin impurity in $^{104m}$Ag will be explained. Finally, the result and the different systematic errors will be discussed.

## 8.2 $^{104g}$Ag experiment: fraction measurements

The isotope $^{104g}$Ag has a very complex decay scheme with numerous $\gamma$-rays, which is presented in detail by Münnich et al. (1971); Firestone (1996) (see Fig. 8.1). Before proceeding to the determination of the fraction, it is worth to present the general properties of the $\gamma$-rays and the $Q$-factors that we have used in the determination of the fraction. In general, each $\gamma$-ray has a different sensitivity curve reflecting different $U_\lambda A_\lambda$-coefficients. However, for the $\gamma$-rays chosen for this analysis (i.e. 741 keV, 1527 keV, and 1626 keV $\gamma$-rays) these coefficients are the same. In this way, we limit the systematic error in the fraction determination, and at the same time increase statistics. Furthermore, all three lines have good relative intensities and are clearly visible in the $\gamma$-spectra (see Fig. 5.1).

Table 8.1 lists the relevant properties of the $\gamma$-rays of $^{104g}$Ag that have been used for the fraction determination. The solid angle corrections ($Q$-factors) for the 0° and the 90° HPGe $\gamma$-detectors are indicated as well. They were determined according to the procedure outlined in Krane (1972), adopted for Monte Carlo calculations.

To determine $W(\Theta)$ versus temperature for these three $\gamma$-ray the large volume HPGe detectors at 0° and 90° were used. In order to take into account the rather short half-life of $^{104g}$Ag as well as possible beam fluctuations we determined the $W(0°)/W(90°)$. Thus, experimentally the anisotropy function $R$ is

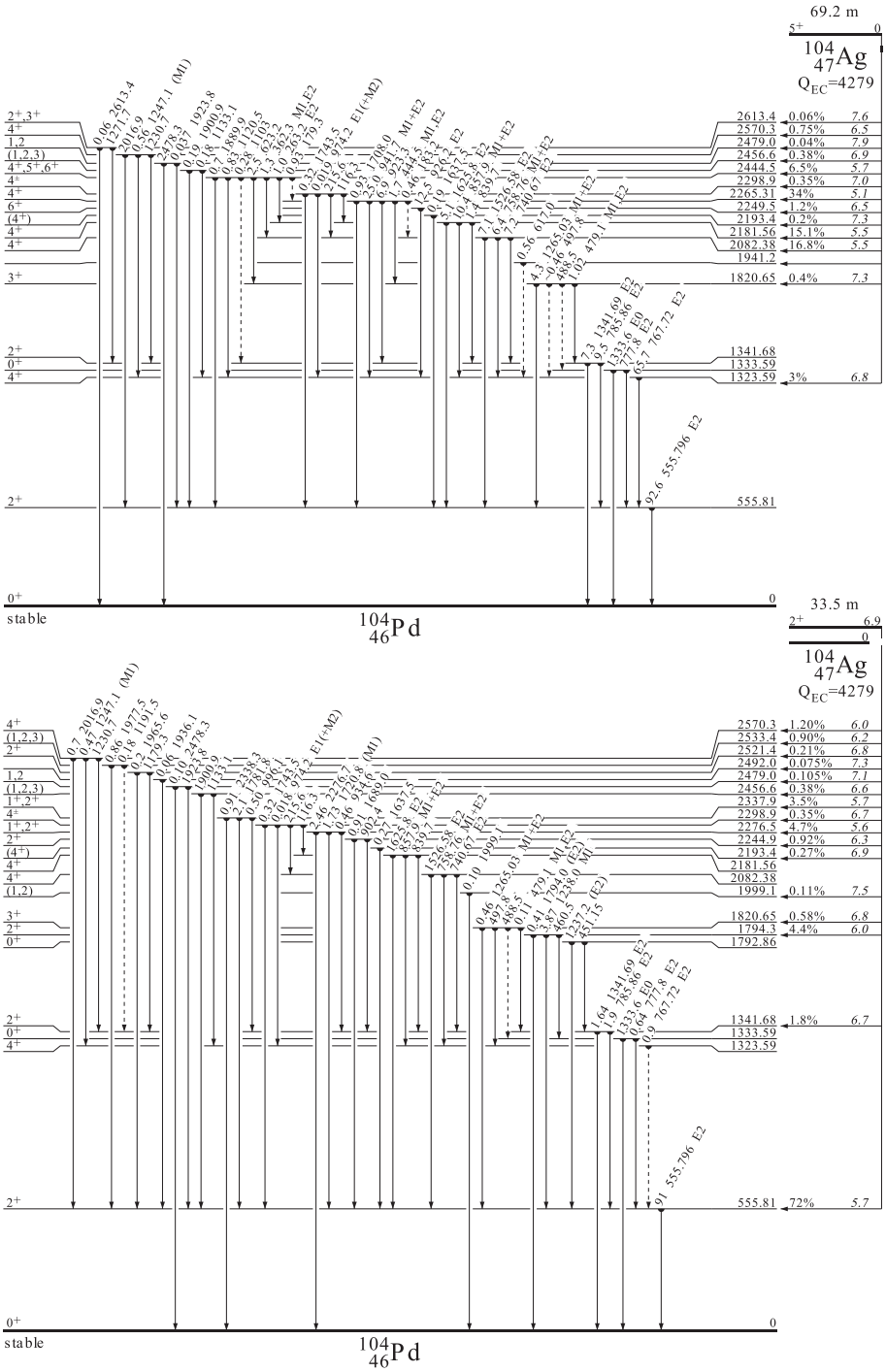


**Figure 8.1:** Partial scheme of low lying levels in $^{104}$Pd populated in the $EC/\beta^+$-decay of $^{104g,m}$Ag (adopted from Firestone (1996)).

**Table 8.1:** Main properties of the $\gamma$-rays in the decay of $^{104}$Ag that have been used for the fraction determination. $Q$-factors for the 0° and the 90° HPGe $\gamma$-detectors are indicated as well.

| $E_\gamma$, keV | $Q_2$ | $Q_4$ | $U_2$ | $U_4$ | $A_2$ | $A_4$ |
|---|---|---|---|---|---|---|
| 741 | 0.9519[1] | 0.8460[1] | 0.9394 | 0.7977 | -0.4477 | -0.3044 |
| | 0.9575[2] | 0.8631[2] | 0.9394 | 0.7977 | -0.4477 | -0.3044 |
| 1527 | 0.9532[1] | 0.8498[1] | 0.9394 | 0.7977 | -0.4477 | -0.3044 |
| | 0.9585[2] | 0.8661[2] | 0.9394 | 0.7977 | -0.4477 | -0.3044 |
| 1626 | 0.9533[1] | 0.8501[1] | 0.9394 | 0.7977 | -0.4477 | -0.3044 |
| | 0.9585[2] | 0.8663[2] | 0.9394 | 0.7977 | -0.4477 | -0.3044 |

[1] 0° $\gamma$-detector; [2] 90° $\gamma$-detector

given by

$$R = \frac{W(0°)}{W(90°)} = \frac{\left[\frac{N(0°)}{N(90°)}\right]_{\text{cold}}}{\left[\frac{N(0°)}{N(90°)}\right]_{\text{warm}}}, \tag{8.1}$$

where $N(\Theta)_{\text{cold}}$ ($N(\Theta)_{\text{warm}}$) is the "cold", i.e. polarized ("warm", i.e. unpolarized) $\gamma$-ray count rate. The sample temperature during these measurements was about 10 mK. This temperature was monitored by observing the anisotropy of the 136 keV $\gamma$ line of a $^{57}$CoFe nuclear thermometer (Marshak (1986)) that was soldered with Woods metal onto the copper sample holder. A superconducting magnet provided an external field capable to magnetically saturate the iron foil in a direction parallel to its surface and perpendicular to the implanted beam direction. The field direction also specified the axis of measurements.

Data were recorded simultaneously at 0°, 90° and 180° with respect to the orientation axis by three large volume HPGe detectors. However, in the analysis we used only data recorded with the 0° and 90° detectors, as the electronics for the 180° detector failed during the experiment. The 0° detector was located at about 85 mm from the sample, the 90° was at about 92 mm from the sample. Typical energy resolution of these HPGe detectors was 2.5 and 4 keV respectively at 1332 keV as was verified with a standard $^{60}$Co calibration source. A typical $\gamma$-ray spectrum obtained in 300 s with these detectors is shown in

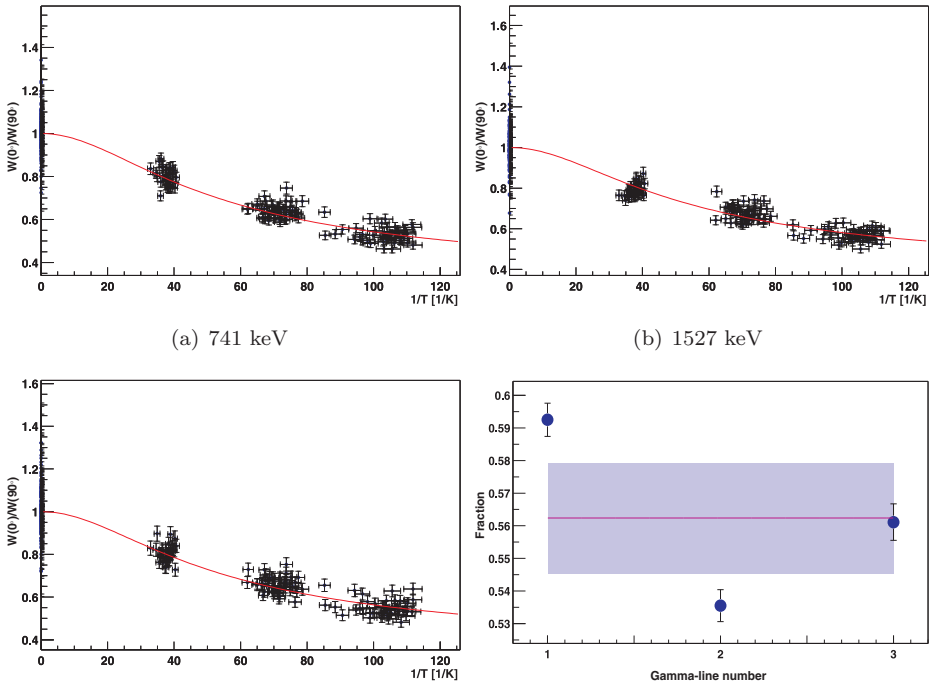


(a) 741 keV (b) 1527 keV

(c) 1626 keV (d) average

**Figure 8.2:** Fits of the anisotropies of the three $\gamma$-rays to determine the fraction of $^{104g}$Ag in *run B*. Figure (d) shows the results. The band represents the weighted average (see appendix B).

Fig. 5.1.

Special care was taken to avoid any movement of the HPGe detectors, as this is quite important when using a tight geometry (it changes the $Q$-factor correction). We verified through measurements of the positions of the $\gamma$-detectors in the beginning and at the end of experiment that no movement has occurred. A precision pulse generator was used to correct for dead time in the counting system.

Initially, we assumed that the sixth-order orientation coefficient is negligibly small and based our analysis only on the $B_2U_2A_2$ and $B_4U_4A_4$ terms (see Eq. 1.3). Using the magnetic moment $\mu[^{104g}\mathrm{Ag}] = 3.918(2)\ \mu_\mathrm{N}$ that was ob-

tained in the NMR/ON experiment (see Chapter 5) and the total magnetic field the implanted nuclei feel, i.e. $|B_{\mathrm{tot}}| = 44.644(21)$ T (see Chapter 5) the implantation fraction could then be determined for each run from the measured $\gamma$-anisotropies and Eq. 1.3. As was already mentioned before, a two-site model is used for this, where $f$ is the fraction of the impurities (i.e. Ag isotopes in the iron foil) occupying undisturbed lattice sites, which contribute to the full $\gamma$-ray anisotropy. The remaining fraction $1 - f$ is assumed to be in disturbed sites given rise to zero anisotropy when averaged over the sample.

About 75 spectra of 300 s each were recorded for *run A*, about 260 of the same time length for *run B*, and 115 spectra for *run C*. In *run A* and *C* only one temperature point has been taken, while in *run B* data were taken at three different temperatures. The production rate of $^{104g}$Ag was not the same in each run due to a problem with the high voltage at the ISOLDE target, leading to different statistical error bars.

As was mentioned in Chapter 5, due to the rather long half-life for both silver isotopes and their rather large magnetic hyperfine interaction strength no problems with incomplete spin-lattice relaxation are to be expected. Also from the quality of the fit results we do not see an indication for the presence of incomplete relaxation (i.e. see Fig. 7.4 in Chapter 7). In our treatment of the data, we considered only measurements with a stable temperature, i.e. all transitional points between two temperatures were rejected.

Fig. 8.2 shows the fit results for the three $\gamma$-rays leading to the implantation fraction for *run B*. As can be seen the three values obtained for $f$ scatter quite a bit, leading to a rather large error bar on the weighted average. As we will see further for the two other runs the spread of the three values was smaller, but statistics was also smaller. Table 8.2 summarizes the fit results for the fraction for each separate run. Two possible explanations for the observed differences in the value of $f$ for the three runs can be suggested:

1. Due to the problems with the high voltage supply for the ISOLDE liquid-tin target that was used in this experiment, the implantation spot of the silver ions on the iron foil was not the same for the three runs. The beam was indeed re-tuned for each run. Since, in addition, the Fe sample foil had a width of only 10 mm, compared to a width of 14 mm for the copper

**Table 8.2:** Overview of the fit results for $f$ in each separate run. The last column in this table shows a weighted average[1] for all three $\gamma$-rays involved.

| | $f_{E_\gamma}$ | | | $\overline{f} \pm \delta\overline{f}$ |
|---|---|---|---|---|
| | 741 keV | 1527 keV | 1626 keV | |
| *run A* | 0.6130±0.0101 | 0.6018±0.0117 | 0.5942±0.0130 | 0.6046±0.0066 |
| *run B* | 0.5925±0.0051 | 0.5355±0.0049 | 0.5611±0.0056 | 0.5624±0.0171 |
| *run C* | 0.6708±0.0088 | 0.6467±0.0089 | 0.6795±0.0103 | 0.6644±0.0053 |

[1] See appendix B for the statistical procedure

sample holder, it could be that in at least two of the three runs part of the $^{104}$Cd beam was implanted not in the same spot in the Fe foil.

2. A possible contamination of the radioactive beam by a different amount of stable beam could possibly also explain differences in the fraction. However, since a too high stable beam contamination causes a reduction of the fraction due to the damage it causes to the lattice structure of the Fe foil, while here the fraction drops from *run A* to *run B*, and then increases in *run C*, this option is to be excluded.

## 8.3 $^{104m}$Ag experiment: isospin admixture

We will now concentrate on the determination of the isospin admixture in $^{104m}$Ag. Fig. 5.3 in Chapter 5 shows a typical $\beta^+$-spectrum recorded in 300 s. Fig. 8.4 shows the sum spectrum of all "warm" $\beta^+$-spectra of $^{104m}$Ag in *run B* with the energy regions that were used for the analysis indicated. The decay scheme for the $2^+$ isomeric state $^{104m}$Ag ($T_{1/2}$ = 33 min) can be found in Münnich et al. (1971); Firestone (1996) (see also Fig. 8.1).

The lower energy limit for the analysis of the $\beta^+$-asymmetry of the $^{104m}$Ag decay was chosen to be 800 keV, to avoid contamination from the most intense $\gamma$-rays in the $^{104g}$Ag decay. Also, the ground state $^{104g}$Ag emits positrons with an energy up to 1933 keV. However, the summed intensity of these positrons

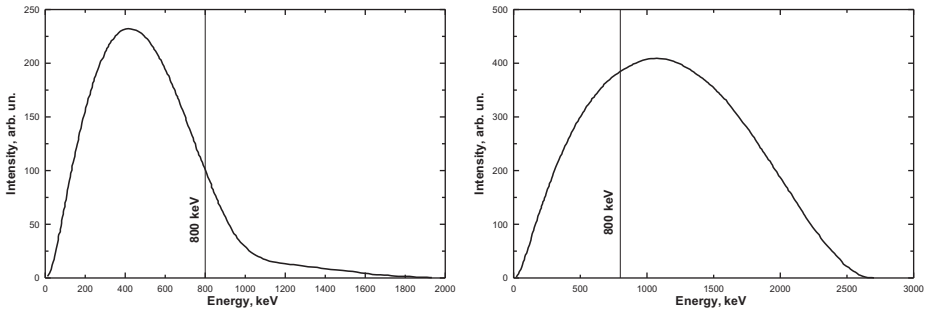


(a) $^{104g}$Ag (b) $^{104m}$Ag

**Figure 8.3:** Simulated $\beta^+$ spectrum for the ground state of $^{104g}$Ag (a) with endpoint energy of 1933 keV, and for the isomeric state of $^{104m}$Ag with endpoint energy of 2708 keV.

in the energy region between 800 and 1933 keV did not give a considerable contribution except for the region from 800 kev to 1 MeV (see Fig. 8.3). This energy region was thus excluded in the analysis. The upper limit for the analysis was chosen to be 2000 keV, as the number of $\beta$ particles above this point gets considerably less and contamination of the spectra due to pile-up of the $\beta$'s with the 511 keV annihilation $\gamma$-ray thus becomes relatively more important.

Tables 8.3 and 8.4 list the $Q$-factors calculated with GEANT4 for the energy bins for $^{104m}$Ag in the region from 800 keV to 2000 keV for two particle detectors at opposite sides of the sample holder (i.e. 15° and 165°). In these calculations we considered only the strongest $\beta^+$-branch, which accounts for 72 % of the total decay strength in the $\beta^+$-decay of $^{104m}$Ag to the ground state of stable $^{104}$Pd, with an endpoint energy of 2708 keV (see Firestone (1996) and Fig. 8.3). Thus, our calculation contains some uncertainties related to the not fully exact modelling of the $\beta$-spectrum. However, as the intensities of all other $\beta$-branches of $^{104m}$Ag with endpoint energy above 800 keV (the lowest energy considered for the analysis here) add up to only 8.1 %, considering only the 72 % branch is a reasonable approximation for our purpose here. The average values for the $Q$-factors and their uncertainties were calculated according to Eqn. 2.1 and 2.2.

The procedure to calculate the $\frac{v}{c}$ factor was outlined already in section 1. The

**Table 8.3:** $Q$-factor corrections calculated with GEANT4 for the 15° particle detector in the six energy bins in the $\beta$-spectrum of $^{104m}$Ag defined in Fig. 8.4, in the region from 800 keV to 2000 keV.

| | $E_\beta$, keV | | | | | |
|---|---|---|---|---|---|---|
| | $E_1$ | $E_2$ | $E_3$ | $E_4$ | $E_5$ | $E_6$ |
| | 800-1000 | 1000-1200 | 1200-1400 | 1400-1600 | 1600-1800 | 1800-2000 |
| | $Q_{15°}$-factors | | | | | |
| $m$ | $Q_{E_1}$ | $Q_{E_2}$ | $Q_{E_3}$ | $Q_{E_4}$ | $Q_{E_5}$ | $Q_{E_6}$ |
| 1 | 0.8032 | 0.8239 | 0.8908 | 0.9039 | 0.8859 | 0.9091 |
| 2 | 0.7691 | 0.8079 | 0.8652 | 0.8850 | 0.8922 | 0.9254 |
| 3 | 0.8077 | 0.8237 | 0.8876 | 0.9060 | 0.8877 | 0.9075 |
| 4 | 0.7671 | 0.8131 | 0.8681 | 0.8840 | 0.8932 | 0.9278 |
| 5 | 0.8040 | 0.8331 | 0.8470 | 0.8709 | 0.9294 | 0.9188 |
| $\overline{Q}$ | 0.7902 | 0.8203 | 0.8717 | 0.8900 | 0.8977 | 0.9177 |
| $\Delta\overline{Q}$ | 0.0203 | 0.0099 | 0.0179 | 0.0148 | 0.0180 | 0.0092 |

**Table 8.4:** $Q$-factor corrections calculated with GEANT4 for the 165° particle detector in the six energy bins in the $\beta$-spectrum of $^{104m}$Ag (Fig. 8.4), in the region from 800 keV to 2000 keV.

| | $Q_{165°}$-factors | | | | | |
|---|---|---|---|---|---|---|
| $m$ | $Q_{E_1}$ | $Q_{E_2}$ | $Q_{E_3}$ | $Q_{E_4}$ | $Q_{E_5}$ | $Q_{E_6}$ |
| 1 | 0.7913 | 0.8507 | 0.8676 | 0.8845 | 0.9217 | 0.9511 |
| 2 | 0.7904 | 0.8380 | 0.8748 | 0.9029 | 0.9252 | 0.9221 |
| 3 | 0.7920 | 0.8925 | 0.8646 | 0.8851 | 0.9236 | 0.9497 |
| 4 | 0.7901 | 0.8545 | 0.8633 | 0.8864 | 0.9241 | 0.9484 |
| 5 | 0.7992 | 0.8457 | 0.8492 | 0.8941 | 0.9664 | 0.9390 |
| $\overline{Q}$ | 0.7926 | 0.8563 | 0.8639 | 0.8906 | 0.9322 | 0.9421 |
| $\Delta\overline{Q}$ | 0.0038 | 0.0212 | 0.0093 | 0.0079 | 0.0192 | 0.0121 |

**Table 8.5:** The $\frac{v}{c}$ factor calculated for each of the six energy bins in the $\beta^+$-spectra of $^{104m}$Ag. The energy represents the average energy for each bin in keV.

| | | | | | | |
|---|---|---|---|---|---|---|
| $\overline{E}$ | 900 | 1100 | 1300 | 1500 | 1700 | 1900 |
| $\frac{v}{c}$[1] | 0.9321 | 0.9484 | 0.9594 | 0.9672 | 0.9729 | 0.9773 |

[1] See Eq. 1.25

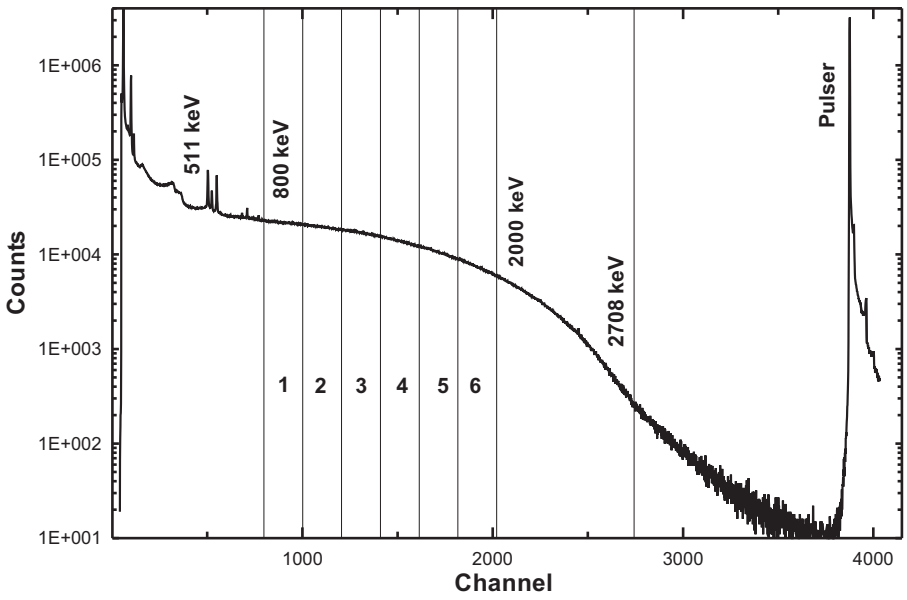


**Figure 8.4:** "Warm" (i.e. no polarization) sum $\beta^+$-spectrum of $^{104m}$Ag obtained with the 15° particle detector installed inside the 4 K radiation shield. The parts of the $\beta^+$-spectra used for the determination of the isospin admixture in $^{104m}$Ag as well as the endpoint energy are indicated. Note that region '1' was later excluded as simulations showed a too large contribution of $\beta$-particles from $^{104g}$Ag in this region (see Fig. 8.3).

results for each energy bin used in our analysis are presented in Table 8.5. As was mentioned before, within the precision of the energy calibration of the particle detectors (i.e. a few keV) and the energy resolution (i.e. about 4 to 5 keV), it was not necessary to take into account the exact shape of the $\beta$ spectrum.

Fig. 8.5 (a,b,c) shows a typical fit of the $W(15°)/W(165°)$ $\beta^+$-anisotropy as a function of inverse temperature in the decay of $^{104m}$Ag for the energy bin from 1200 to 1400 keV for the three runs. The band in Fig. 8.5 (d) represents the weighted average and was determined according to the statistical procedure outlined in appendix B. Although the statistics in *run B* was much better than in the two other runs the scattering of the fitted points around the weighted average resulted in an about 3 times larger error bar compared to *runs A and* C. The fit results for $A_1$ for all energy regions and for the three runs are listed

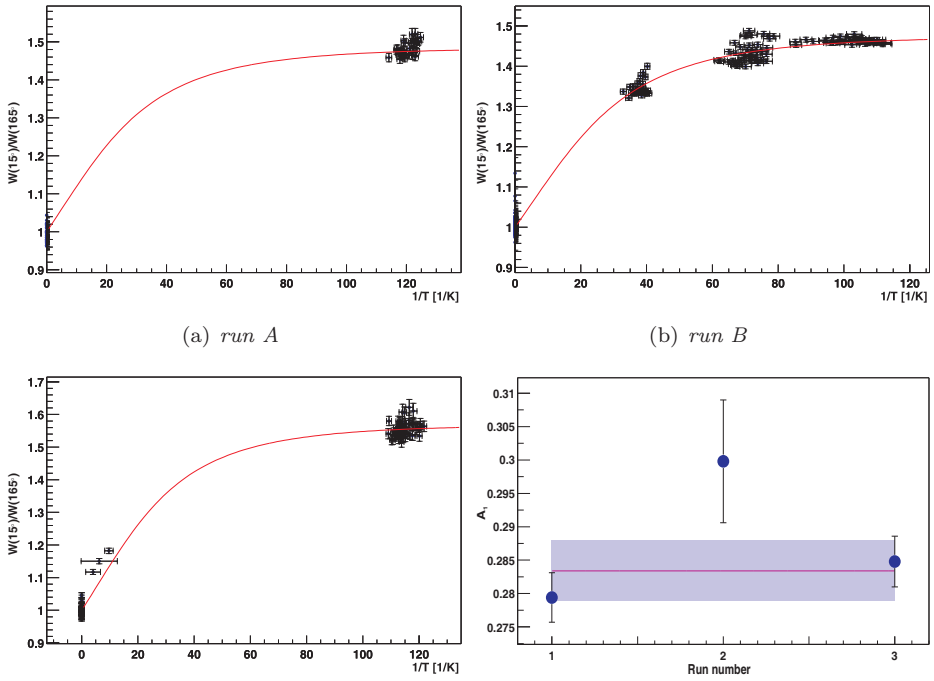


(a) *run A* (b) *run B*

(c) *run C* (d) average

**Figure 8.5:** Fit results for the asymmetry parameter $A_1$ of $^{104m}$Ag for the energy bin from 1200 to 1400 keV (a, b, and c) in the three runs. Figure (d) shows the weighted average value for the asymmetry parameter $A_1$ for all three runs (each individual error includes only the statistical error, and error from the fraction uncertainty). The band represents the statistical and fraction error (see appendix B and Table 8.7) for all three runs.

in Table 8.6. The combined value for the $A_1$ asymmetry parameter for $^{104m}$Ag from all three runs is

$$A_1[^{104m}\mathrm{Ag}] = -0.2842 \pm 0.0068_{\mathrm{tot}} \tag{8.2}$$

The total error account is given in Table 8.7. The systematic error includes the errors due to uncertainties of the nuclear magnetic moment $\mu$, the implantation fraction $f$, the $\frac{v}{c}$, the correction factor $Q_1$, and the hyperfine field $B_{\mathrm{hf}}$. As can be seen, the systematic error due to the uncertainty of the nuclear magnetic moment of $^{104m}$Ag is almost negligible. The largest contributions to the total error come from statistics, the $Q_1$ correction factor and the fraction.

**Table 8.6:** Overview of the fit results for $A_1$ in the $\beta^+$-decay of $^{104m}$Ag in the three runs. The errors indicated are only statistical, including the $S$-factor (see appendix B). The first energy bin was not used in the calculation of the weighted averages, as it contains too much contamination from positrons from the decay of the ground state of $^{104}$Ag (see Fig. 8.3.)

| | $E_1$ | $E_2$ | $E_3$ | $E_4$ | $E_5$ | $E_6$ | weighted average $E_2$ to $E_6$ |
|---|---|---|---|---|---|---|---|
| *Run A* | 0.3028 | 0.2852 | 0.2831 | 0.2800 | 0.2745 | 0.2742 | 0.2794 |
| $\Delta_A$ | 0.0029 | 0.0027 | 0.0026 | 0.0028 | 0.0025 | 0.0029 | 0.0022 |
| *Run B* | 0.3248 | 0.3039 | 0.2995 | 0.2999 | 0.2969 | 0.2983 | 0.2998 |
| $\Delta_B$ | 0.0007 | 0.0007 | 0.0006 | 0.0006 | 0.0008 | 0.0007 | 0.0011 |
| *Run C* | 0.3276 | 0.2995 | 0.2924 | 0.2908 | 0.2832 | 0.2804 | 0.2891 |
| $\Delta_C$ | 0.0019 | 0.0020 | 0.0020 | 0.0018 | 0.0018 | 0.0020 | 0.0035 |

Table 8.6 shows the values of $A_1$ for all six energy bin in the three different runs. The errors indicate only the statistical error for each individual fit, the statistical procedure is outlined in appendix B.

**Table 8.7:** Total error account in units of $10^{-4}$ for $A_1[^{104m}\text{Ag}]$ including the statistical error from the three runs, and the different systematic errors related to the fitting procedure. The statistical error includes the $S$-factor (see appendix B).

| | statistics | $\frac{v}{c}$ | $\mu$ | $B_{\text{hf}}$ | $Q_1$ | $f$ | statistics and $f$ |
|---|---|---|---|---|---|---|---|
| *run A* | 22 | | | | | 30 | $37^b$ |
| *run B* | 11 | 1 | 3 | 1 | 49 | 91 | $92^b$ |
| *run C* | 35 | | | | | 42 | $55^b$ |
| $68^a$ | | 1 | 3 | 1 | 49 | | 47 |

$^a$Total error; $^b$see Fig. 8.5 (d).

## 8.4 Conclusion and Discussion

The result for the asymmetry parameter $A_1[^{104m}\text{Ag}]$ corresponds to a F/GT mixing ratio of $y = -42(6) \cdot 10^{-3}$ (the other, larger value $y = -4.0(1)$ is not considered here as it would translate into the presence of a huge Fermi contri-

bution in this supposedly pure Gamow-Teller $\beta^+$-decay of $^{104m}$Ag). Combining this mixing ratio with the log $ft$-value of 5.67(4) that is known from the literature (see i.e. Münnich et al. (1971)) and using Eqns. 6.13 and 6.9, the isospin mixing amplitude and corresponding Fermi matrix element are found to be $|\alpha_{T_0+1}| = 1.4(2) \cdot 10^{-3}$ ($\alpha^2_{T_0+1} = 2.0(6) \cdot 10^{-6}$) and $|M_F| = 4.8(7) \cdot 10^{-3}$. This results is significantly smaller than the value estimated with Eq. 6.7 from Chapter 6, i.e. $\alpha^2 = P[^{104m}\text{Ag}] \approx 4.24 \cdot 10^{-3}$. It should be stressed though that Eq. 6.7 yields the total isospin impurity while our experiment determines only the contribution from the analog state.

# Chapter 9

# Discussion of isospin impurities

Fig. 9.1, Fig. 9.2, and Table 9.1 (adopted from Raman et al. (1975) and extended with later published results) summarize the situation concerning the admixture amplitude ($\alpha_{T_0+1}$) from the analog state for all nuclei addressed till now using $\beta$-decay experiments. Figures 9.1 and 9.2 show that isospin impurities are small and remain small for heavier nuclei despite the increase of the Coulomb forces. For states with isospin $T > 4$ the isospin impurity from the analog state is found to be typically about one order of magnitude smaller than for states with low isospin. That is what one should expect on theoretical grounds was pointed out by Colò et al. (1995); Nagarajan et al. (1995) (see Chapter 6 and references therein), considering the more general case of the total isospin impurity. The crux of their explanation is that in heavy nuclei the large neutron excess, which by itself has pure isospin since no protons are involved, strongly dilutes the isospin impurity. In addition various theoretical models (see Chapter 6) show that the probability of mixing between $T = T_0$ and $T = T_0 + 1$ states are reduced by a factor of $T_0 + 1$, which is large for heavy nuclei.

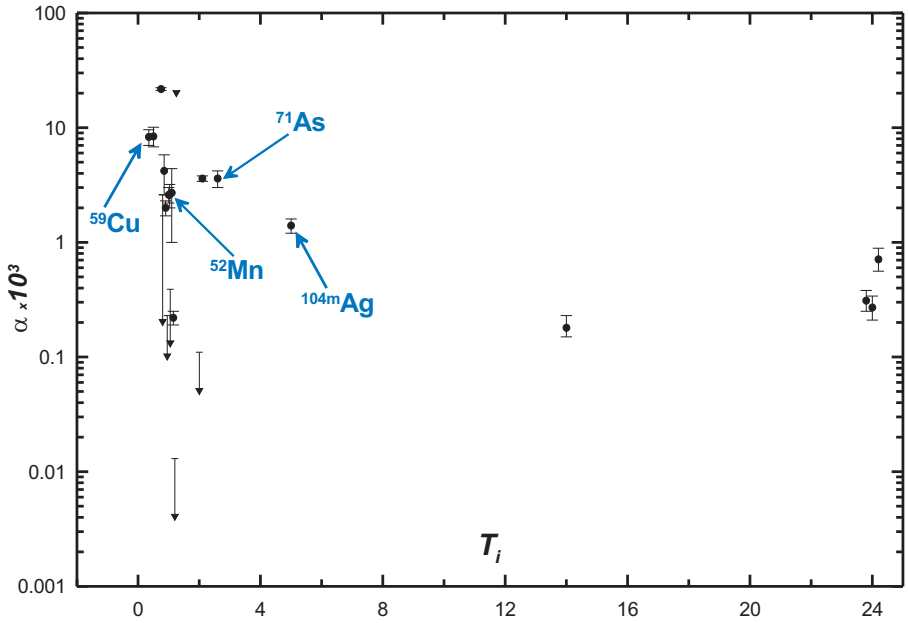


**Figure 9.1:** Isospin impurity amplitudes $|\alpha_{T_0+1}|$ deduced from $\beta^+$-decay experiments as function of isospin number of the decaying state. The values for the mixing amplitudes are adopted from Raman et al. (1975). The results from this and other recent works are also included. The nuclei that were studied by our group are indicated. If only the upper error bar is shown the result is consistent with zero and only upper limit is relevant.

| name | $\beta^{\pm}$ | $T_i$ | $T_f$ | $\lvert\alpha_{T_0+1}\rvert$ $\cdot 10^3$ | $\lvert\Delta\alpha_{T_0+1}\rvert$ $\cdot 10^3$ | $\lvert\alpha^{\text{theo}}_{\text{Colò}}\rvert$ $\cdot 10^3$ | $\frac{\alpha^{\text{theo}}_{\text{Colò}}}{\alpha_{T_0+1}}$ |
|---|---|---|---|---|---|---|---|
| $^{20}$F | $\beta^-$ | 1 | 0 | 1.6 | $^{+3.3}_{-1.6}$ | | |
| $^{24}$Na | $\beta^-$ | 1 | 0 | 0.5 | $\pm 0.4$ | | |
| $^{24}$Al | $\beta^+$ | 1 | 0 | 0.2 | $^{+2.4}_{-0.2}$ | | |
| $^{27}$Mg | $\beta^-$ | 3/2 | 1/2 | 0.6 | $^{+9.5}_{-0.6}$ | | |
| $^{41}$Ar | $\beta^-$ | 5/2 | 3/2 | 2.8 | $\pm 1.1$ | | |
| $^{44}$Sc | $\beta^+$ | 1 | 2 | 4.2 | $\pm 1.6$ | | |
| $^{46}$Sc | $\beta^-$ | 2 | 1 | 0.03 | $^{+0.13}_{-0.03}$ | | |
| | | | | 0.72 | $^{+0.13}_{-0.16}$ | | |
| $^{48}$Sc | $\beta^-$ | 3 | 2 | 0.11 | $^{+0.23}_{-0.11}$ | | |
| $^{48}$V | $\beta^+$ | 1 | 2 | 2.0 | $\pm 0.3$ | | |
| | | | | 0.10 | $^{+0.13}_{-0.10}$ | | |
| $^{49}$Ca | $\beta^-$ | 9/2 | 7/2 | 0.15 | $^{+2.5}_{-0.15}$ | | |

*continued on next page*

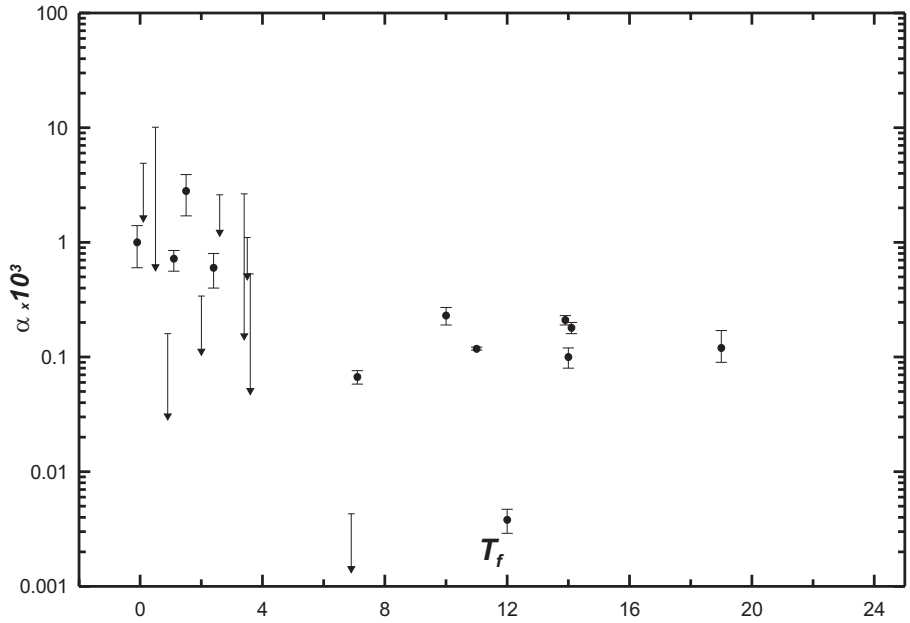


**Figure 9.2:** Isospin impurity amplitudes deduced from $\beta^-$-decay experiments as function of isospin number. The values for the mixing amplitudes are adopted from Raman et al. (1975).

*continued from previous page*

| name | $\beta^{\pm}$ | $T_i$ | $T_f$ | $\lvert\alpha_{T_0+1}\rvert$ $\cdot 10^3$ | $\lvert\Delta\alpha_{T_0+1}\rvert$ $\cdot 10^3$ | $\lvert\alpha^{\text{theo}}_{\text{Colò}}\rvert$ $\cdot 10^3$ | $\frac{\alpha^{\text{theo}}_{\text{Colò}}}{\alpha_{T_0+1}}$ |
|---|---|---|---|---|---|---|---|
| $^{52}$Mn | $\beta^+$ | 1 | 2 | 2.6 | $\pm 0.4$ | | |
| | | | | 0.13 | $^{+0.26}_{-0.13}$ | | |
| $^{52}$Mn[b] | | | | 2.6 | $\pm 0.6$ | 54.8 | 21 |
| $^{52m}$Mn | $\beta^+$ | 1 | 2 | 2.7 | $\pm 1.7$ | | |
| $^{56}$Co | $\beta^+$ | 1 | 2 | 0.22 | $\pm 0.03$ | | |
| $^{56}$Co | $\beta^+$ | 1 | 2 | 0.004 | $^{+0.009}_{-0.004}$ | | |
| $^{57}$Ni | $\beta^+$ | 1/2 | 3/2 | 8.4 | $^{+1.7}_{-1.6}$ | | |
| $^{58}$Co | $\beta^+$ | 2 | 3 | 0.05 | $^{+0.06}_{-0.05}$ | | |
| $^{59}$Fe | $\beta^-$ | 7/2 | 5/2 | 0.6 | $\pm 0.2$ | | |
| | | | | 1.2 | $^{+1.4}_{-1.2}$ | | |
| $^{59}$Cu[d] | $\beta^+$ | 1/2 | 3/2 | 8.3 | $\pm 1.3$ | 78.5 | 9.5 |
| $^{64}$Ga | $\beta^+$ | 1 | 2 | 21.7 | $\pm 0.6$ | | |
| $^{65}$Ni | $\beta^-$ | 9/2 | 7/2 | 0.05 | $^{+0.48}_{-0.05}$ | | |
| | | | | 0.5 | $^{+0.6}_{-0.6}$ | | |
| $^{66}$Ge | $\beta^+$ | 1 | 2 | $<19.8$ | | | |
| $^{66}$Ga | $\beta^+$ | 2 | 3 | 3.6 | $\pm 0.2$ | | |

*continued on next page*

*continued from previous page*

| name | $\beta^{\pm}$ | $T_i$ | $T_f$ | $\lvert\alpha_{T_0+1}\rvert$ $\cdot 10^3$ | $\lvert\Delta\alpha_{T_0+1}\rvert$ $\cdot 10^3$ | $\lvert\alpha^{\text{theo}}_{\text{Colò}}\rvert$ $\cdot 10^3$ | $\frac{\alpha^{\text{theo}}_{\text{Colò}}}{\alpha_{T_0+1}}$ |
|---|---|---|---|---|---|---|---|
| $^{71}$As[a] | $\beta^+$ | 5/2 | 7/2 | 3.6 | $\pm 0.6$ | 55.7 | 15 |
| $^{104m}$Ag[c] | $\beta^+$ | 5 | 6 | 1.4 | $\pm 0.2$ | 65.1 | 47 |
| $^{110m}$Ag | $\beta^-$ | 8 | 7 | 0.0014 | $^{+0.0029}_{-0.0014}$ | | |
| | | | | 0.067 | $\pm 0.009$ | | |
| $^{124}$Sb | $\beta^-$ | 11 | 10 | 0.23 | $\pm 0.04$ | | |
| $^{134}$Cs | $\beta^-$ | 12 | 11 | 0.118 | $^{+0.004}_{-0.003}$ | | |
| $^{152}$Eu | $\beta^-$ | 13 | 12 | 0.0038 | $\pm 0.0009$ | | |
| $^{156}$Eu | $\beta^-$ | 15 | 14 | 0.21 | $\pm 0.02$ | | |
| | | | | 0.10 | $\pm 0.02$ | | |
| | | | | 0.18 | $\pm 0.02$ | | |
| $^{170}$Lu | $\beta^+$ | 14 | 15 | 0.18 | $^{+0.05}_{-0.03}$ | | |
| $^{188}$W | $\beta^-$ | 20 | 19 | 0.12 | $^{+0.05}_{-0.03}$ | | |
| $^{234}$Np | $\beta^+$ | 24 | 25 | 0.31 | $^{+0.07}_{-0.06}$ | | |
| | | | | 0.27 | $^{+0.07}_{-0.06}$ | | |
| | | | | 0.71 | $^{+0.18}_{-0.15}$ | | |

[a] The experimental values are given in ref. Severijns et al. (2005).
[b] The experimental values are given in ref. Schuurmans et al. (2000).
[c] The experimental values are given in Chapter 8, this work.
[d] The experimental values are given in Chapter 7, this work.

**Table 9.1:** Experimental results for the admixture amplitude corresponding to the analog state, determined from $\beta^{\pm}$-decay. The last two columns list the total estimated isospin impurity obtained from Eq. 6.7 (Colò et al. (1995); Nagarajan et al. (1995)) and the ratio between this total expected impurity and the one from the analog state as obtained from experiments studied by our group.

Recently Farnea et al. (2003) investigated the isospin impurity in $^{64}$Ge through the observation of forbidden $E_1$ transitions, which probes the total $T_0 + 1$ isospin impurity in state with isospin $T_0$. Their experimental result, i.e. $\alpha^2 = (2.5^{+1.0}_{-0.7}) \cdot 10^{-2}$, has the same order of magnitude as the theoretical prediction of $\alpha^2 = 0.012$ obtained from Eq. 6.7 (Colò et al. (1995); Nagarajan et al. (1995), see also Fig. 6.2). It is to be noted though that the result of Farnea et al. (2003) is based on a rather schematic model such that no high precision can be expected.

Comparing the values listed in Table 9.1 with those calculated from Eq. 6.7 (Colò et al. (1995); Nagarajan et al. (1995)), the isospin impurity caused by the analog state turns out to represent only a very small fraction of the total expected isospin impurity from all states with isospin $T = T_0 + 1$ (with $T_0$ the isospin of the state investigated). This can intuitively be understood from the fact that at high excitation energies the density of the states is very high such that many states with isospin $T_0 + 1$ will exist. Nevertheless, due to this multitude of states the isospin impurity contribution from the analog state can still be dominant one, even though the value of it is rather small.

# Chapter 10

# Conclusion

In this work, we have investigated the nuclear magnetic moments of several ground and isomeric states with the Nuclear Magnetic Resonance on Oriented Nuclei method applied to $^{59}$Cu, $^{69}$As, and $^{104m,g}$Ag. In some experimental runs we in addition also deduced with the LTNO method the values of the partial isospin impurities for these nuclei, induced by analog states. To interpret the experimental results various theoretical models were used.

In case of $^{59}$Cu, comparison of our result for the nuclear magnetic moment with the prediction from shell-model calculations using perturbation theory (Golovko et al. (2004)) reveals a big discrepancy between theory and experiment. As the theoretical prediction was based on the assumption that $^{56}$Ni is a doubly closed-shell nucleus and the departure from this can be estimated in perturbation theory, the poor comparison of theory with experiment indicates $^{56}$Ni is not a doubly-magic closed-shell nucleus.

In case of $^{69}$As, the experimental result is in fairly good agreement with the simple theoretical model suggested by Bohr and Mottelson (1953) for a strong coupled system consisting of a single particle and the nuclear core, when taking into account 'effective' (modified) $g$-factors. The theoretical result based on this simple model is also in agreement with calculations carried out by Brant et al. (2004) in the framework of the proton-neutron interacting boson-fermion

model.

For the nuclei $^{104g,m}$Ag, the experimental results are in very good agreement with a calculation based on the 'additivity' rule for odd-odd nuclei (i.e. Blin-Stoyle (1956); Ames et al. (1961); Heyde (1990)) under the assumption of weak coupling between protons and neutrons. The best agreement is achieved when experimental $g$-factors of neighboring odd-even nuclei are used. As the theoretical nuclear magnetic moments for the $^{104}$Ag ground and isomeric states are not described by 'pure' single particle states but by the mixing of two configurations the coefficients for this configuration mixing were determined too.

The isospin mixing of the analog state of the final (daughter) state for $^{59}$Cu with isospin $T = 1/2$ has been measured using the LTNO method (see Chapter 7). The total isospin impurity has been calculated for this nucleus based on the model of Colò et al. (1995); Nagarajan et al. (1995). The partial isospin impurity from the analog state deduced from $\beta^+$-decay is well below these estimates.

The isospin mixing for $^{69}$As was not discussed here as it turned out (due to the lack of statistics in the data and a not negligible presence of other radioactive isotopes) that no reliable analysis was possible.

The isospin mixing of the analog state of the final (daughter) state for $^{104m}$Ag with isospin $T = 5$ has been measured using the LTNO method (see Chapter 8). It has been shown that due to the very precise measurement of the nuclear magnetic moment of the isomeric state of $^{104m}$Ag its contribution to the total error is almost negligible. Again, the partial isospin impurity from the analog state deduced from the emission asymmetry in the $\beta^+$-decay of $^{104m}$Ag is well below the estimate for the total isospin impurity given by the model of Colò et al. (1995); Nagarajan et al. (1995).

Note, finally, that though the observed isospin impurity contributions from the analog states are small they can still be larger than those of the non-analog states with isospin $T_0 + 1$ due to the multitude of states at high excitation energies.

# Appendix A

# Formulae for $\beta$-decay

The number of $\beta$-particles with momentum $p$ in the interval between $p$ and $p + dp$ emitted per unit time is (see Behrens and Jänecke (1969)):

$$N(p_e)dp_e = \frac{g^2}{2\pi^3} p_e^2 \cdot p_\nu^2 \cdot F(Z, W_e) \cdot C(W_e)dp_e \tag{A.1}$$

where

$g =$ weak interaction coupling constant,
$p_e =$ electron momentum in units of $m_0c$,
$W_e = \sqrt{p_e^2 + 1} =$ total electron energy in units of $m_0c^2$,
$W_0 =$ maximum value[1] of $W_e$
$p_\nu = W_0 - W_e =$ energy or momentum of the neutrino in units of $m_0c^2$ or $m_0c$, respectively,
$Z =$ atomic number of the daughter nucleus.

The Fermi-function $F(Z, W_e)$ takes into account the distortion of the electron wave function by the nuclear charge. It has the following form

$$F(Z, W_e) = F_0 L_0$$

[1] For $\beta^-$-decay the maximum kinetic energy $W_0 - 1$ is equal to the difference of the atomic masses, for $\beta^+$-decay $2m_0c^2$ must be subtracted from this difference in order to obtain $W_0 - 1$.

with

$$F_0 = 4 \cdot (2p_e R)^{-2(1-\gamma_1)} \cdot \frac{|\mathbf{\Gamma}(\gamma_1 + \mathbf{i}y)|^2}{[\mathbf{\Gamma}(2\gamma_1 + 1)]^2} \cdot \mathbf{e}^{\pi \cdot y}, \tag{A.2}$$

where

$$\begin{aligned} y &= \alpha Z \cdot \frac{W_e}{p_e}, \\ \gamma_1 &= \sqrt{1 - (\alpha Z)^2}, \\ \alpha &= 1/137.0388 && \text{fine structure constant,} \\ R &= r_0 A^{1/3} && \text{nuclear radius,} \\ r_0 &= && \text{Bohr radius } (\approx 1.2 \text{ fm}), \\ A &= && \text{mass number,} \end{aligned}$$

and

$$L_0 = \frac{\alpha_{-1}^2 + \alpha_{+1}^2}{2p_e^2 F_0}. \tag{A.3}$$

The $C(W_e)$ in Eq. A.1 is called the spectrum shape factor and exact formulae for its numerical calculation are given elsewhere (see Behrens and Jänecke (1969)). The quantities $\alpha_{k_e}$ are so-called Coulomb amplitudes, which must also be calculated numerically. Here we do not consider any difference in the spectrum shape factor for positrons and electrons.

The evaluation of beta-decay involves consideration of a large number of influences. These are enumerated. For purposes of highest accuracy it is desirable that these influences be exposed as far as possible in analytical form so that their interplay and their dependence upon their own internal parameterizations may be transparent. A programme to this effect is defined and is embarked upon by presenting the analytical forms for the traditional differential and integral phase space factors for (allowed) beta-decay as expansions in powers of $\alpha Z$. The accuracy of these expansions is indicated in detail by Wilkinson (1989, 1990, 1993, 1995a,b, 1997, 1998).

# Appendix B

# The statistical procedures

The statistical procedures we have followed in analyzing the experimental data are based on those used by the Particle Data Group in their periodic reviews of particle properties, e.g. by Eidelman et al. (2004). In the tables and throughout this work, error bars and uncertainties always refer to plus-and-minus one standard deviation (68 % confidence level). For a set of $N$ uncoupled measurements, $x_i \pm \delta x_i$, of a particular quantity, a gaussian distribution is assumed, the weighted average being calculated according to:

$$\overline{x} \pm \delta\overline{x} = \frac{\sum_i w_i x_i}{\sum_i w_i} \pm \left(\sum_i w_i\right)^{-1/2}, \tag{B.1}$$

where

$$w_i = 1/(\delta x_i)^2 \tag{B.2}$$

and the sums extend over all $N$ measurements. For each average, the $\chi^2$ was computed with the *MINUIT* programm (James and Roos (1975)), and a scale factor, $S$, was determined as:

$$S = \left[\chi^2/(N-\nu)\right]^{1/2}, \tag{B.3}$$

where $\nu$ is the number of fitting parameters (i.e. if we are fitting a constant $\nu = 1$). This factor is then used to establish the quoted uncertainty. If $S \leq 1$, the value of $\delta\overline{x}$ from Eq. B.1 is left unchanged. If $S > 1$ and the input $\delta x_i$ are

all about the same size, then $\delta\overline{x}$ is increased by the factor $S$, which is equivalent to assuming that all the experimental errors were underestimated by the same factor. Finally, if $S > 1$ but the $\delta x_i$ are of widely varying magnitudes, $S$ is recalculated with only those results for which $\delta x_i \leq 3N^{1/2}\delta\overline{x}$ being retained; the recalculated scale factor is then applied in the usual way. In all three cases, no change is made to the original average $\overline{x}$ calculated with Eq. B.1.

# Samenvatting

## Inleiding

Dankzij recente ontwikkelingen is het mogelijk geworden om een heel aantal nieuwe, protonrijke kernen te produceren, zodat nu de meeste kernen langs de N=Z lijn die nog gebonden verondersteld worden, geobserveerd zijn, tot aan A=100. Inmiddels werd de productie van deze kernen zo verbeterd, dat het mogelijk wordt om hun belangrijkste eigenschappen te meten. Hierdoor wordt de kennis van de kernstructuur in de buurt van de N=Z lijn grondig uitgebreid. Een gevolg van deze evolutie is de hernieuwde interesse in isospinbijmenging in N=Z kernen. Isospin is een goed kwantumgetal wanneer de fundamentele eigenschappen van ladingssymmetrie en ladingsonafhankelijkheid van de sterke kracht verondersteld worden. Dit betekent dat het proton en het neutron gezien worden als twee toestanden van hetzelfde deeltje: het nucleon. Wanneer de massa van de kern toeneemt, wordt de afstotende Coulombkracht sterker dan de aantrekkende kracht die het verschil tussen proton- en neutrondichtheden tracht te minimalizeren. De isospinbijmenging is groter voor kernen met hogere Z, en is het grootste voor kernen met N=Z. In dit werk werd niet enkel de isospinbijmenging gemeten, maar er werden ook drie magnetische momenten bepaald. Deze metingen waren noodzakelijk om de isospinbijmenging met voldoende nauwkeurigheid te kunnen bepalen maar aangezien deze momenten op zichzelf zeer interessant zijn in de context van kernstructuur, zijn deze metingen een belangrijk onderdeel van dit werk.

**Tabel B.1:** De belangrijkste eigenschappen van de gemeten isotopen en hun $\beta$-verval. $E^{\beta}_{\text{eind}}$ is de eindpuntsenergie van het $\beta$-spectrum van de bestudeerde overgang.

| Isotoop | $T_{1/2}$ | $I^{\pi}$ | $E^{\beta}_{\text{eind}}$, keV | $T$ |
|---|---|---|---|---|
| $^{59}$Cu | 82 s | $3/2^{-}$ | 3778 | 1/2 |
| $^{69}$As | 15.4 m | $5/2^{-}$ | 2991 | 3/2 |
| $^{104m}$Ag | 33.5 m | $2^{+}$ | 2708 | 5 |

# Experimenten

In dit onderzoek werd de isospinbijmenging gemeten in grondtoestanden met isospin T gaande van 1/2 tot 5 en dit in kernen met Z-waardes van 29 tot 47 (zie Tabel B.1). De asymmetrieparameters van de bestudeerde kernen werden gemeten met behulp van lage-temperatuurskernoriëntatie. Deze metingen werden uitgevoerd met de $^{3}$He-$^{4}$He dilutiecryostaat NICOLE verbonden met de ISOLDE separator in CERN, Genève. De bestudeerde isotopen werden in een Fe-folie geïmplanteerd die bevestigd was op de koude vinger van de cryostaat. De $\beta$-anisotropie werd bepaald met behulp van drie HPGe detectors die in de cryostaat geïnstalleerd werden, de $\gamma$-straling werd gemeten met drie Ge $\gamma$-detectoren die buiten de cryostaat opgesteld werden.

De isospinbijmengingsamplitudes werden bekomen door de *ft*-waardes voor de $\beta$-overgangen te combineren met de asymmetrieparameter bepaald uit de anisotropie van de $\beta$-deeltjes uitgezonden door georiënteerde kernen. De asymmetrieparameter moet echter met voldoende precisie gemeten worden om de isospinbijmengingsamplitudes te kunnen bepalen. Om de vereiste nauwkeurigheid te halen, is het noodzakelijk om alle andere parameters zoals de temperatuur, de implantatiekwaliteit (fractie van kernen op goede roosterposities), de Q-factoren, het magnetisch moment $\mu$ en het totale magnetische veld ($B_{\text{tot}}$) dat de kernen voelen, voldoende goed te kennen. De temperatuur werd bepaald met behulp van een gecalibreerde $^{57}$CoFe nucleaire thermometer die mee op de bronhouder bevestigd werd. Alle parameters in de $\gamma$-aniostropie van dit isotoop zijn gekend zodat uit de gemeten anistropie de temperatuur bepaald kan worden. De kwaliteit van de implantatie werd bepaald door een meting van de $\gamma$-

of $\beta$-anisotropie van een gekend isotoop van de kern die bestudeerd werd. Daar voor deze isotopen alle parameters gekend zijn, levert een meting van de anisotropie de maat voor de implantatiekwaliteit. De Q-factoren die onder meer de openingshoek, magnetische-veldeffecten en verstrooiïng in rekening brengen werden berekend met het simulatieprogramma GEANT4 (Agostinelliae et al. (2003)). De belangrijkste bijdrage in het magnetische veld $B_{\text{tot}}$ is het magnetische hyperfijnveld. Voor alle bestudeerde isotopen was dit veld met voldoende precisie gekend uit vorige metingen met Nucleaire Magnetische Resonantie op Georiënteerde Kernen (NMR/ON). De magnetische momenten waren echter niet voldoende gekend en werden voor dit werk gemeten met NMR/ON tijdens de meting van de isospinbijmenging. De isospin bijmenging van $^{69}$As werd niet bepaald door een gebrek aan statistiek en de niet te verwaarlozen contaminatie van de spectra door andere kernen.

# Experimentele resultaten

## Magnetisch moment van $^{59}$Cu

$^{59}$Cu ligt dicht bij de schilsluiting en er wordt dan ook verwacht dat het magnetisch moment goed beschreven wordt met een schillenmodelbenadering waarbij 1 proton zich buiten de gesloten protonschil bevindt, en twee neutronen buiten de neutronschil. Het gemeten kernmoment voor $^{59}$Cu verschilt echter zeer duidelijk van de voorspelde waarde berekend op basis van het schillenmodel (Golovko et al. (2004)). Deze theoretische voorspelling is gebaseerd op de veronderstelling dat $^{56}$Ni gesloten schillen heeft. Aangezien deze veronderstelling een verkeerde waarde voorspelt voor het magnetisch moment van $^{59}$Cu, is dit een aanwijzing dat $^{56}$Ni geen dubbel magische kern is.

## Magnetisch moment van $^{69}$As

De experimentele waarde voor het magnetische moment van $^{69}$As komt overeen met het model van Bohr and Mottelson (1953) voor een sterk gekoppeld systeem van een afzonderlijk deeltje en een kern waarbij de effectieve $g$-factoren

werden gebruikt. Het resultaat gebaseerd op dit eenvoudig model, is ook in overeenstemming met berekeningen van Brant et al. (2004) in het kader van het proton-neutron interagerend boson-fermion model.

## Magnetisch moment van $^{104m}$Ag

Voor $^{104g,m}$Ag zijn de experimentele resultaten in goede overeenstemming met een berekening gebaseerd op de 'additiviteit' voor oneven-oneven kernen (Blin-Stoyle (1956); Ames et al. (1961); Heyde (1990)) in de veronderstelling van zwakke koppeling tussen protonen en neutronen. Het beste resultaat wordt bekomen wanneer de experimenteel bepaalde $g$-factoren van naburige oneven-even kernen gebruikt worden. De theoretische kernmomenten van de grondtoestand en de isomere toestand van $^{104}$Ag worden beschreven door een menging van twee configuraties in plaats van zuivere toestanden. De mengcoëfficiënten van deze configuraties werden eveneeens bepaald.

## Isospinbijmenging in $^{59}$Cu

De isospin bijmenging van de analoge toestand van $^{59}$Cu (isospin $T = 1/2$) werd gemeten met Lage-Temperatuurskernoriëntatie. De totale isospinbijmenging voor deze kern werd dan uitgerekend op basis van het model van Colò et al. (1995); Nagarajan et al. (1995). De gedeeltelijke isospinbijmenging van de analoige toestand zoals gemeten in $\beta^+$ verval ligt heel wat lager dan deze schatting.

## Isospinbijmenging in $^{104m}$Ag

De isospinbijmenging door de analoge toestand werd ook bepaald voor $^{104m}$Ag (isospin $T = 5$). Door de zeer nauwkeurige bepaling van het magnetische moment van de isomere toestand $^{104m}$Ag, is de bijdrage van de fout op dit moment bijna geheel te verwaarlozen. De isospinbijmenging van de analoge toestand die werd bepaald uit de $\beta^+$-asymmetrie is opnieuw lager dan de geschatte waarde voor de totale bijmenging zoals die gegeven wordt door het model van Colò

et al. (1995); Nagarajan et al. (1995).

## Besluit

In dit werk werden drie magnetische kernmomenten bepaald met behulp van NMR/ON. Deze gemeten waardes werden vergeleken met berekende waarden. De isospinbijmenging door de analoge toestand werd gemeten voor $^{59}$Cu en voor $^{104m}$Ag. De bekomen waardes zijn klein in vergelijking met de voorspelling voor de totale isospinbijmenging. Het moet wel worden opgemerkt dat ondanks het feit dat de isospinbijmengingen van de analoge toestanden klein zijn, ze toch groter kunnen zijn dan de bijmenging van de niet-analoge $(T_0 + 1)$ toestanden door het groot aantal toestanden bij hoge excitatie-energie.

# Bibliography


Abele, H., E. Barberio, D. Dubbers, F. Gluck, J. Hardy, W. Marciano, A. Serebrov, and N. Severijns: 2004, 'Quark mixing, CKM unitarity - The unitarity problem'. *Eur. Phys. J. C* **33**, 1–8.

Agostinelliae, S., J. Allisonas, K. Amakoe, J. Apostolakisa, H. Araujoaj, P. Arcel, M. Asaig, D. Axeni, S. Banerjeebi, G. Barrandan, F. Behnerl, and L. Bellagambac: 2003, 'Geant4a simulation toolkit'. *Nucl. Instr. and Meth. A* **506**, 250–303.

Akai, H.: 1988, 'Nuclear spin-lattice relaxation of impurities in ferromagnetic iron'. *Hyp. Int.* **43**, 255–270.

Ames, O., A. M. Bernstein, M. H. Brennan, and D. R. Hamilton: 1961, 'Magnetic Moments of 69-min $Ag^{104}$ and 27-min $Ag^{104m}$'. *Phys. Rev.* **123**, 1793–1800.

Anderson, J. D., C. Wong, and J. W. McClure: 1965, 'Coulomb Displacement Energies Derived from the $(p, n)$ Isobaric Reactions'. *Phys. Rev. B* **138**, 615.

Andreoiu, C., D. Rudolph, I. Ragnarsson, C. Fahlander, R. Austin, M. Carpenter, R. Clark, J. Ekman, R. Janssens, T. Khoo, F. Kondev, T. Lauritsen, T. Rodinger, D. Sarantites, D. Seweryniak, T. Steinhardt, C. Svensson, O. Thelen, and J. Waddington: 2002, 'Evolution of shapes in Cu-59'. *Eur. Phys. J. A* **14**(3), 317–348.

Apostolakis, J. et al.: 1999, 'GEANT4 Low Energy Electromagnetic Models for Electrons and Photons'. Technical report, CERN.

Auerbach, N.: 1972, 'Isovector Monopole Strength in Nuclei'. *Nucl. Phys. A* **182**, 247–264.

Auerbach, N.: 1983, 'Coulomb Effects in Nuclear Structure'. *Phys. Reports* **98**, 273–341.

Auerbach, N., J. Hüfner, A. K. Kerman, and C. M. Shakin: 1972, 'A Theory of Isobaric Analog Resonances'. *Rev. Mod. Phys.* **44**, 48–125.

Auerbach, N. and A. Klein: 1983, 'A Microscopic Theory of Giant Electric Isovector Resonances'. *Nucl. Phys. A* **395**, 77–118.

Bacon, F., J. A. Barclay, J. A. Brewer, D. A. Shirley, and D. A. Templeton: 1972, 'Temperature-Independent Spin-Lattice Relaxation Time in Metals at Very Low Temperatures'. *Phys. Rev. B* **5**, 23972409.

Becker, F., W. Korten, F. Hannachi, P. Paris, N. Buforn, C. Chandler, M. Houry, H. Hubel, A. Jansen, Y. Le Coz, C. F. Liang, A. Lopez-Martens, R. Lucas, E. Mergel, P. H. Regan, and C. Schonwasser, G. Theisen: 1999, 'Investigation of prolate-oblate shape-coexistence in Kr-74'. *Eur. Phys. J. A* **4**(2), 103–105.

Behrens, H. and Jänecke: 1969, 'Numerical Tables for Beta-Decay and Electron Capture'. *Numeric. Data and Funct. Relat. in Scien. and Tech.* **4**, 1–315.

Berkes, I. et al.: 1985, 'Nuclear Implantation into Cold On Line Equipment, Proposal for on line nuclear orientation on ISOLDE-3'. Technical report, CERN.

Bertschat, H. et al.: 1973, 'Magnetic moments of excited $9/2^+$ states around A=70 experimental values for $^{67}$Zn and $^{67}$Ge'. *J. Phys. Soc. Japan.* **34**, 217–220.

Blin-Stoyle, R. J.: 1956, 'Theories of Nuclear Moments'. *Rev. Mod. Phys.* **28**(1), 75–101.

Bloembergen, N. and G. M. Temmer: 1953, 'Nuclear Magnetic Resonance of Aligned Radioactive Nuclei'. *Phys. Rev.* **89**, 883.

Bohr, A.: 1951a, 'Nuclear Magnetic Moments and Atomic Hyperfine Structure'. *Phys. Rev.* **81**(3), 331–335.

Bohr, A.: 1951b, 'On the Quantization of Angular Momenta in Heavy Nuclei'. *Phys. Rev.* **81**(1), 134–138.

Bohr, A. and B. R. Mottelson: 1953, 'Collective and Indidvidual-Particle Aspects of Nuclear Structure'. *Dan. Mat. Fys. Medd.* **27**, 7–174.

Bohr, A. and B. R. Mottelson: 1998, *Nuclear Structure*, Vol. 1. Singapore: World Scientific, 2 edition.

Bouchez, E., I. Matea, W. Korten, F. Becker, B. Blank, C. Borcea, A. Buta, A. Emsallem, G. de France, J. Genevey, F. Hannachi, K. Hauschild, A. Hurstel, Y. L. Coz, M. Lewitowicz, R. Lucas, F. Negoita, F. de Oliveira Santos, D. Pantelica, J. Pinston, P. Rahkila, M. Rejmund, M. Stanoiu, and C. Theisen: 2003, 'New Shape Isomer in the Self-Conjugate Nucleus Kr'. *Phys. Rev. Lett.* **90**(8), 082502.

Brack, M., A. Jensen, H. Pauli, Strutins.V.M., C. Wong, and J. Damgaard: 1972, 'Funny Hills: The Shell-Correction Approach to Nuclear Shell Effects and Its Applications to the Fission Process'. *Rev. Mod. Phys.* **44**(2), 320–405.

Brant, S., N. Yoshida, and L. Zuf: 2004, '$\beta$-decay of odd-$A$ As to Ge isotopes in the interacting boson-fermion model'. *Phys. Rev. C* **70**(5), 054301.

Buck, B. and A. C. Merchant: 2001, 'Magnetic moments of mirror nuclei'. *Phys. Rev. C* **63**, 037301.

Cabibbo, N.: 1963, 'Unitary Symmetry and Leptonic Decays'. *Phys. Rev. Lett.* **10**, 531–532.

Caso, C. et al.: 1998, 'Review of particle physics'. *Eur. Phys. J. C* **3**(1-4), 1–794.

Chikazumi, S.: 1964, *Physics of magnetizm*, Vol. 1. New York: J. Wiley and Sons, 4 edition.

Colò, G., M. A. Nagarajan, P. Van Isacker, and A. Vitturi: 1995, 'Isospin mixing in proton-rich $N \approx Z$ nuclei'. *Phys. Rev. C* **52**, R1175–R1178.

Courtnay, W. J. and J. Fox: 1975, 'Experimental Coulomb Displacement Energies between Analog Energy Levels of Isobaric Nuclei with A = 3, to A = 238'. *At. Data and Nucl. Data Tabl.* **15**, 141.

Dinger, U., J. Eberz, G. Huber, R. Menges, R. Kirchner, O. Klepper, T. Kühl, and D. Marx: 1989, 'Nuclear moments and change in the charge radii of neutron-deficient silver isotopes'. *Nucl. Phys. A* **503**, 331–348.

Dobaczewski, J. and I. Hamamoto: 1995, 'Isospin impurities in ground states of $N = Z$ nuclei near the proton-drip line'. *Phys. Lett. B* **345**, 181–184.

Eder, R., E. Hagn, and E. Zech: 1984, 'Nuclear Magnetic Resonance on oriented $^{106}$Ag in Fe and Ni'. *Phys. Rev. C* **30**, 676–683.

Eidelman, S., K. Hayes, K. Olive, M. Aguilar-Benitez, et al.: 2004, 'Review of Particle Physics'. *Phys. Lett. B* **592**(1-4), 1–1109.

Ekman, J., D. Rudolph, C. Fahlander, A. P. Zuker, M. A. Bentley, S. M. Lenzi, C. Andreoiu, M. Axiotis, G. de Angelis, E. Farnea, A. Gadea, T. Kröl, N. Mărginean, T. Martinez, M. N. Mineva, C. Rossi-Alvarez, and C. A. Ur: 2004, 'Unusual Isospin-Breaking and Isospin-Mixing Effects in the A = 35 Mirror Nuclei'. *Phys. Rev. Lett.* **92**, 132502.

Farnea, E., G. de Angelis, A. Gadea, P. G. Bizzeti, A. Dewald, J. Eberth, A. Algora, M. Axiotis, D. Bazzacco, A. M. Bizzeti-Sona, F. Brandolini, G. Colò, W. Gelletly, M. A. Kaci, N. Kintz, T. Klug, T. Kröll, S. M. Lenzi, S. Lunardi, N. Mărginean, T. Martínez, R. Menegazzo, D. R. Napoli, J. Nyberg, P. Pavan, Z. Podolyák, C. M. Petrache, B. Quintana, B. Rubio, P. Spolaore, T. Steinhardt, J. L. Taín, O. Thelen, C. A. Ur, R. Venturelli, and M. Weiszflog: 2003, 'Isospin mixing in the $N = Z$ nucleus $^{64}$Ge'. *Phys. Lett. B* **551**, 56–62.

Fedosseev, V. et al.: 2003, 'Atomic spectroscopy studies of short-lived isotopes and nuclear isomer separation with the ISOLDE RILIS'. *Nucl. Instr. and Meth. B* **204**, 353358.

Firestone, R. B.: 1996, *Table of Isotopes*, Vol. 1. New York: Wiley, 8 edition.

Fox, R. A., P. D. Johnston, and N. J. Stone: 1971, 'NMR/ON of $^{110}$Ag$^m$ in Fe and Ni'. *Phys. Lett. A* **34**, 211–212.

Fuchs, N. H., M. Knecht, and J. Stern: 2000, 'Contributions of order O(m(quark)**2) to K(l3) form factors and unitarity of the CKM matrix'. *Phys. Rev. D* **62**, 033003.

Giani, S. et al.: 1999, 'GEANT4 Simulation of Energy Losses of Ions'. Technical report, INFN.

Golovko, V. V., I. Kraev, T. Phalet, N. Severijns, B. Delauré, M. Beck, V. Kozlov, A. Lindroth, P. Herzog, C. Tramm, D. Zákoucký, D. Vénos, D. Srnka, M. Honusek, and U. Köster: 2005a, 'Measurement of the Nuclear Magnetic Moment of $^{104m}$Ag with On-Line $\beta$-NMR on Oriented Nuclei'. *to be published in Phys. Rev. C*.

Golovko, V. V., I. Kraev, T. Phalet, N. Severijns, B. Delauré, M. Beck, V. Kozlov, A. Lindroth, P. Herzog, C. Tramm, D. Zákoucký, D. Vénos, D. Srnka, M. Honusek, and U. Köster: 2005b, 'Nuclear Magnetic Moment of $^{69}$As from On-Line $\beta$-NMR on Oriented Nuclei'. *to be published in Phys. Rev. C*.

Golovko, V. V., I. Kraev, T. Phalet, N. Severijns, B. Delauré, M. Beck, V. Kozlov, A. Lindroth, P. Schuurmans, B. Vereecke, S. Versyck, P. Herzog, C. Tramm, D. Zákoucký, D. Vénos, D. Srnka, M. Honusek, U. Köster, and I. S. Towner: 2004, 'Nuclear Magnetic Moment of $^{59}$Cu from On-Line $\beta$-NMR on Oriented Nuclei'. *Phys. Rev. C* **70**(1), 014312.

Greenebaum, B. and E. A. Phillips: 1974, 'Nuclear moments of $^{102}$Ag$^m$ and $^{106}$Ag$^g$'. *Phys. Rev. C* **9**(4), 2028–2032.

Guin, R., S. K. Saha, S. M. Sahakundu, and S. Prakash: 1990, 'The decay of $^{104m}$Ag'. *J. Radioanal. Nucl. Chem.* **141**, 185–189.

Hagn, E., E. Zech, and G. Eska: 1981, 'Nuclear Magnetic Moment of 6.9 h $^{93}$Mo$^m$'. *Phys. Rev. C* **23**(5), 2252–2257.

Halbert, M., P. Tjom, I. Espe, G. Hagemann, B. Herskind, M. Neiman, and H. Oeschler: 1976, 'High Spin States in $^{74}$Se'. *Nucl. Phys. A* **259**(3), 496–512.

Hamamoto, I. and H. Sagawa: 1993, 'Gammow-Teller beta decay and isospin impurity in nuclei near the proton drip line'. *Phys. Rev. C* **48**, R960–R963.

Hamilton, J., A. Ramayya, W. Pinkston, R. Ronninge, G. Garciabe, H. Carter, R. Robinson, H. Kim, and R. Sayer: 1974, 'Evidence for Coexistence of Spherical and Deformed Shapes in $^{72}$Se'. *Phys. Rev. Lett.* **32**(5), 239–243.

Hardy, J. C. and I. S. Towner: 1975, 'Superallowed $0^+ \rightarrow 0^+$ nuclear $\beta$-decays and cabibbo universality'. *Nucl. Phys. A* **254**, 221–240.

Hardy, J. C. and I. S. Towner: 2005, 'New limits on fundamental weak-interaction parameters from superallowed $\beta$ decay'. *to be published in Phys. Rev. Lett.*

Heighway, E. A. and J. D. MacArthur: 1970, 'The effect of a finite size source on angular distribution attenuation coefficients'. *Nucl. Instr. and Meth.* **79**, 224–228.

Heisenberg, W.: 1932, 'The structure of atomic nuclei'. *Zeits. f. Physik* **77**, 1–11.

Herzog, P.: 1986, *Low-Temperature Nuclear Orientation*, Chapt. 15, On-Line Nuclear Orientation, pp. 731–767. Elsevier Science Publishers B.V.

Herzog, P., U. Dämmrich, K. Freitag, C. D. Herrmann, and K. Schlösser: 1989, 'The Magnetic Moments of $(\nu g_{9/2})$-Levels in Odd Zn Isotopes'. *Z. Physik A* **332**, 247–250.

Herzog, P., N. J. Stone, and P. D. Johnston: 1976, 'The nuclear magnetic moment of $^{71}$As and $^{72}$As'. *Nucl. Phys. A* **259**, 378–384.

Heyde, K. L. G.: 1990, *The Nuclear Shell Model*. Berlin: Springer, 2 edition.

Hogervorst, W., H. A. Helms, G. J. Zaal, J. Bouma, and J. Blok: 1980, 'The Hyperfine Structure and Nuclear Moments of Some Neutron-Deficient Arsenic Isotopes'. *Z. Physik A* **294**(1), 1–5.

Honma, M., B. A. Brown, T. Mizusaki, and T. Otsuka: 2002, 'Full pf-shell calculations with a new effective interaction'. *Nucl. Phys. A* **704**, 134c–143c.

Hurtado, S., M. Carciá-León, and R. Garciá-Tenorio: 2004, 'GEANT4 code for simulation of a germanium gamma-ray detector and its application to efficiency calibration'. *Nucl. Instr. and Meth. A* **518**, 764–774.

Hutchison, W. D., N. Yazidjoglou, and D. H. Chaplin: 1992, 'Nuclear Magnetic Resonance of Brute Force Oriented $^{110m}$AgAg'. *Hyp. Int.* **73**, 247–254.

Ivanchenko, V. N. et al.: 1999a, 'GEANT4 Simulation of Energy Losses of Ions'. Technical report, CERN.

Ivanchenko, V. N. et al.: 1999b, 'GEANT4 Simulation of Energy Losses of Slow Hardons'. Technical report, CERN.

James, F. and M. Roos: 1975, 'Minuit - a system for function minimization and analysis of the parameter errors and correlations'. *Computer Physics Communications* **10**, 343–367.

Kaplan, M., P. Kittel, P. D. Johnston, and N. J. Stone: 1972, 'Nuclear polarization and NMR of $^{74}$As in Fe'. *Nucl. Phys. A* **193**, 410–416.

Khoi, L. D., P. Veillet, and I. A. Campbell: 1975, 'The temperature dependence of hyperfine fields at impurities in Fe'. *J. Phys. F* **5**(11), 2184–2190.

Klein, E.: 1983, 'Nuclear Spin-Lattice Relaxation of Impurities in Iron'. *Hyp. Int.* **16**, 557–568.

Klein, E.: 1986, *Low-Temperature Nuclear Orientation*, Chapt. 12, pp. 579–640. Amsterdam: Elsevier.

Kobayashi, M. and T. Maskawa: 1973, 'CP violation in the renormalizable theory of weak interaction'. *Prog. Theor. Phys.* **49**, 652–657.

Koi, Y., M. Kawakami, T. Hihara, and A. Tsujimura: 1972, 'Hyperfine Fields at P-31, As-75, Nb-93, Sb-121 and Sb-123 in Iron'. *J. Phys. Soc. Japan.* **33**(1), 267.

Kontani, M., T. Hioki, and Y. Masuda: 1972, 'Nuclear Spin Relaxation of Impurities in Dilute Ferromagnetic Alloys'. *J. Phys. Soc. Japan.* **32**(2), 416.

Korten, W.: 2001, 'Shape coexistence and isomerism in Kr isotopes'. *ACTA PHYSICA POLONICA B* **32**(3), 729–738.

Köster, U., U. C. Bergmann, D. Carminati, R. Catherall, J. Cederkäll, J. G. Correia, B. Crepieux, M. Dietrich, K. Elder, V. Fedoseyev, L. Fraile, S. Franchoo, H. Fynbö, U. Georg, T. Giles, A. Joinet, O. C. Jonsson, R. Kirchner, C. Lau, J. Lettry, H. J. Maier, V. I. Mishin, M. Oinonen, L. Peräjärvi, H. L. Ravn, T. Rinaldi, M. Santana-Leitner, U. Wahl, L. Weissman, and the

ISOLDE Collaboration: 2003, 'Oxide fiber targets at ISOLDE'. *Nucl. Instr. and Meth. B* **204**, 303–313.

Köster, U., V. Fedoseyev, V. Mishin, L. Weissman, M. Huyse, K. Kruglov, W. Mueller, P. Van Duppen, J. Van Roosbroeck, P. Thirolf, H. Thomas, D. Weisshaar, W. Shulze, R. Borcea, M. La Commara, H. Schatz, K. Schmidt, S. Röttger, G. Huber, V. Sebastian, K. Kratz, R. Catherall, U. Georg, J. Lettry, M. Oinonen, H. Ravn, H. Simon, and I. collaboration: 2000, 'Isomer separation of $^{70g}$Cu and $^{70m}$Cu with a resonance ionization laser ion source'. *Nucl. Instr. and Meth.* **160**, 528–535.

Krane, K. S.: 1972, 'Solid-angle correction factors for coaxial Ge(Li) detectors'. *Nucl. Instr. and Meth.* **98**, 205–210.

Krane, K. S.: 1973, 'Orientation parameters for low-temperature nuclear orientation'. *Nucl. Data Tabl.* **11**, 407–431.

Krane, K. S.: 1986, *Low-Temperature Nuclear Orientation*, Chapt. 2, pp. 31–111. Amsterdam: Elsevier.

Kudryavtsev, Y., J. Andrzejewski, N. Bijnens, S. Franchoo, J. Gentens, M. Huyse, A. Piechaczek, J. Szeripo, I. Reusen, P. Van Duppen, P. Van Den Bergh, L. Vermeeren, J. Wauters, and A. Wöhr: 1996, 'Beams of short lived nuclei produced by selective laser ionization in a gas cell'. *Nucl. Instr. and Meth.* **114**, 350–365.

Kugler, E.: 2000, 'The ISOLDE facility'. *Hyp. Int.* **129**, 23–42.

Kugler, E., D. Fiander, B. Johnson, H. Haas, A. Przewloka, H. L. Ravn, D. J. Simon, and K. Zimmer: 1992, 'The new CERN-ISOLDE on-line mass-separator facility at the PS-Booster'. *Nucl. Instr. and Meth.* **70**, 41–49.

Kumar, K.: 1978, 'Dynamic deformation theory of shape coexistence, pair fluctuations, and shape transition in Ge nuclei'. *J. Phys. G* **4**, 849–856.

Kumar, K.: 1990, *The Electromagnetic Interaction in Nuclear Spectropy*, Chapt. 3. North-Holland, Amsterdam: .

Lecomte, R., M. Irshad, S. Landsberger, P. Paradis, and S. Monaro: 1980, 'Evidence of a spherical to prolate shape transition in the germanium nuclei'. *Phys. Rev. C* **22**(4), 1530–1533.

Lee, T. D. and C. N. Yang: 1956, 'Question of Parity Conservation in Weak Interactions'. *Phys. Rev.* **104**, 254–258.

Leuthold, K., E. Hagn, H. Ernst, and E. Zech: 1980, 'Ground-state nuclear $g$ factor of $^{97}$Ru'. *Phys. Rev. C* **21**(6), 2581–2589.

Lisetskiy, A. F., N. Pietralla, M. Honma, A. Schmidt, I. Schneider, A. Gade, P. von Brentano, T. Mizusaki, T. Otsuka, and B. A. Brown: 2003, 'Experimental evidence for $^{56}$Ni-core breaking from the low-spin structure of the $N = Z$ nucleus $^{58}_{29}\mathrm{Cu}_{29}$'. *Phys. Rev. C* **68**, 034316.

Lisetskiy, A. F., A. Schmidt, I. Schneider, C. Freiessner, N. Pietralla, and P. von Brentano: 2002, 'Isospin Mixing between Low-Lying States of the Odd-Odd $N = Z$ Nucleus $^{54}$Co'. *Phys. Rev. Lett.* **89**, 012502.

Lister, C., B. Varley, H. Price, and J. Olness: 1982, 'Extreme Prolate Deformation in Light Strontium Isotopes'. *Phys. Rev. Lett.* **49**(5), 308–311.

Liu, K. F. and G. E. Brown: 1976, 'Giant multipole resonances'. *Nucl. Phys. A* **265**, 385–415.

Möller, P. and J. R. Nix: 1981, 'Atomic Masses and Nuclear Ground-State Deformations Calculated with a New Macroscopic-Microscopic Model'. *At. Data and Nucl. Data Tabl.* **26**, 165.

Marshak, H.: 1986, *Low-Temperature Nuclear Orientation*, Chapt. 16, pp. 769–820. Amsterdam: Elsevier.

Matsuta, K., M. Fukuda, M. Tanigaki, T. Minamisono, Y. Nojiri, H. Akai, T. Izumikawa, M. Nakazato, M. Mihara, T. Yamaguchi, A. Harada, M. Sasaki, T. Miyake, T. Fukao, K. Sato, Y. Matsumoto, T. Ohtsubo, S. Fukuda, K. Yoshida, A. Ozawa, S. Momata, T. Kobayashi, I. Tanihata, K. G. Alonso, J. R. and, and T. J. M. Symons: 1996, 'Hyperfine Interaction of $^{13}$O and $^{23}$Mg implanted in Pt'. *Hyp. Int.* **97/98**, 501–508.

Matthias, E. and R. J. Holliday: 1966, 'Nuclear Magnetic Resonance in Polarized Nuclei'. *Phys. Rev. Lett.* **17**(17), 897–899.

Mayer, M. C.: 1950a, 'Nuclear Configurations in the Spin-Orbit Coupling Model. I. Empirical Evidence'. *Phys. Rev.* **78**(1), 16–21.

Mayer, M. C.: 1950b, 'Nuclear Configurations in the Spin-Orbit Coupling Model. II. Theoretical Considerations'. *Phys. Rev.* **78**(1), 22–23.

Mertzimekis, T. et al.: 2002, 'Magnetic Moment of $^{57}$Cu'. Technical report, NSCL.

Möller, P. Nix, J., W. Myers, and W. Swiatecki: 1995, 'Nuclear Ground-State Masses And Deformations'. *At. Data and Nucl. Data Tabl.* **59**(2), 185–381.

Münnich, F., A. Kjelberg, and D. J. Hnatowich: 1971, 'The decay of 33 min $^{104m}$Ag and 69 min $^{104g}$Ag'. *Nucl. Phys. A* **178**, 97–110.

Nagarajan, M. A., P. Van Isacker, and A. Vitturi: 1995, 'Isospin mixing in proton-rich $N \approx Z$ nuclei'. Technical report, GANIL.

Noya, H., A. Arima, and H. Horie: 1958. *Prog. Theor. Phys. Suppl.* **8**, 33.

Noya, H., A. Arima, and H. Horie: 1959, 'Nuclear Moments and Configuration Mixing'. *Prog. Theor. Phys.* **66**, 633–689.

Ormand, W. E. and B. A. Brown: 1985, 'Calculated Isospin-Mixing Corrections to Fermi $\beta$-decays in 1s0d-shell Nuclei with Emphasis on $A = 34$'. *Nucl. Phys. A* **440**, 274–300.

Ormand, W. E. and B. A. Brown: 1995, 'Isospin-mixing corrections for fp-shell Fermi transitions'. *Phys. Rev. C* **52**, 24552460.

Otsuka, T., M. Honma, and T. Mizusaki: 1998, 'Structure of the N=Z=28 Closed Shell Studied by Monte Carlo Shell Model Calculation'. *Hyp. Int. C* **81**, 1588–1591.

Phillips, E. and A. Jackson: 1968, 'Nuclear Magnetic Moments of $Cu^{60}$ and $Cu^{62}$: hfs Experiment and Configuration-Mixing Calculation'. *Phys. Rev.* **169**, 917–923.

Piercey, R., J. Hamilton, R. Soundranayagam, A. Ramayya, C. Maguire, X. Sun, Z. Zhao, R. Robinson, H. Kim, S. Frauendorf, J. Doring, L. Funke, G. Winter, J. Roth, L. Cleemann, J. Eberth, W. Neumann, J. Wells, J. Lin, A. Rester, and H. Carter: 1981, 'Evidence for Deformed Ground States in Light Kr Isotopes'. *Phys. Rev. Lett.* **47**(12), 1514–1517.

Postma, H. and N. J. Stone (eds.): 1986, *Low-Temperature Nuclear Orientation*. Amsterdam: Elsevier.

Raghavan, P.: 1989, 'Table of Nuclear Moments'. *At. Data and Nucl. Data Tabl.* **42**, 189.

Raman, S., T. A. Walkiewicz, and H. Behrens: 1975, 'Superallowed $0^+ \rightarrow 0^+$ and isospin-forbidden $J^\pi \rightarrow J^\pi$ Fermi transitions'. *At. Data and Nucl. Data Tabl.* **16**, 451–494.

Ramayya, A., R. Ronningen, J. Hamilton, W. Pinkston, G. Garciabermudez, R. Robinson, H. Kim, H. Carter, and W. Collins: 1975, 'Mean life and collective effects of the 937 keV, $0^+$ state in $^{72}$Se: Evidence for nuclear coexistance'. *Phys. Rev. C* **12**(4), 1360–1363.

Rehfield, D. V. and R. B. Moore: 1978, 'A study of the beta-ray responce function and performance of an intrinsic-germanium detector mounted in a superconducting solenoid'. *Nucl. Instr. and Meth.* **157**, 367–387.

Reinwater, J.: 1950, 'Nuclear Energy Level Argument for a Spheroidal Nuclear Model'. *Phys. Rev.* **79**(3), 432–434.

Rikovska, J., T. Giles, N. J. Stone, K. Van Esbroek, G. White, A. Wöhr, M. Veskovic, I. S. Towner, P. F. Mantica, J. I. Prisciandaro, D. J. Morrisey, V. N. Fedoseyev, V. I. Mishin, U. Köster, W. B. Walters, and the NICOLE and ISOLDE Callaborations: 2000, 'First On-Line Beta-NMR on oriented nuclei: Magnetic Dipole Moments of the $(\nu p_{1/2})^{-1}$ ground state in $^{67}$Ni and $(\pi p_{3/2})^{+1}$ ground state in $^{69}$Cu'. *Phys. Rev. Lett.* **85**, 1392.

Rikovska, J. and N. J. Stone: 2000, 'Beta-NMR/ON on-line at the NICOLE facility, ISOLDE-recent magnetic moment studies near double magic $^{68}$Ni'. *Hyp. Int.* **129**, 131–140.

Ronningen, R. M., A. V. Ramayya, J. H. Hamilton, W. Lourens, J. Lange, H. K. Carter, and R. O. Sayer: 1976, 'Mean life of the 854 keV $0_2^+$ state in $^{74}$Se and the coexistence model'. *Nucl. Phys. A* **261**, 439–444.

Rose, M. E.: 1953, 'The Analysis of Angular Correlation and Angular Distribution Data'. *Phys. Rev.* **91**, 610–615.

Rotbard, G., M. Vergnes, G. Berrier-Ronsin, J. Vernotte, and R. Tamisier: 1984, '(p,t) strengths in the Ga isotopes'. *Nucl. Phys. A* **430**, 409–425.

Sagawa, H., N. V. Giai, and T. Suzuki: 1995, 'Isospin mixing and the sum rule of super-allowed Fermi $\beta$ decay'. *Phys. Lett. B* **353**, 7–12.

Sagawa, H., N. V. Giai, and T. Suzuki: 1996, 'Effect of isospin mixing on superallowed Fermi $\beta$ decay'. *Phys. Rev. C* **53**, 2163–2170.

Saw, E. L. and C. T. Yap: 1989, 'The Fermi to Gamow-Teller Mixing Ratio of the $\beta^+$ Decay of $^{52}$Mn and Time-Reversal Invariance'. *Z. Physik A* **332**, 285–287.

Schlösser, K., I. Berkes, E. Hagn, P. Herzog, T. Niinikoski, H. Postma, C. Richard-Serre, J. Rikovska, N. J. Stone, L. Vanneste, E. Zech, the ISOLDE Collaboration, and the NICOLE Collaboration: 1988, 'Nuclear Orientation at ISOLDE/CERN'. *Hyp. Int.* **43**, 141–149.

Schuurmans, P.: 1996, 'The Angular Distributions of Alpha Particles Emitted by Oriented Nuclei and their Relation to Nuclear Deformation'. Ph.D. thesis, University of Leuven.

Schuurmans, P., J. Camps, T. Phalet, N. Severijns, B. Vereecke, and S. Versyck: 2000, 'Isospin mixing in the Ground State of $^{52}$Mn'. *Nucl. Phys. A* **672**, 89–98.

Sen, P., C. Sen, and D. Basu: 1977, 'Investigation of levels in nickel-59 following the $\beta^+$ decay of copper-59 '. *Zeits. f. Physik* **280**, 211.

Severijns, N.: 1989, 'Development of Techniques and the First Physical Results Obtained in the Study of Light Nuclei with On-Line and Off-Line Nuclear Orientation'. Ph.D. thesis, University of Leuven.

Severijns, N., D. Vénos, P. Schuurmans, M. Beck, B. Delauré, V. V. Golovko, M. Honusek, I. Kraev, T. Phalet, D. Srnka, B. Vereecke, S. Versyck, D. Zákoucký, and U. Köster: 2005, 'Isospin Mixing in the $T = 5/2$ ground state of $^{71}$As'. *accepted for Phys. Rev. C.*

Shaw, T. L. and N. J. Stone: 1988, 'Nuclear Spin-Lattice Relaxation in On-Line Nuclear Orientational Experiments'. *Hyp. Int.* **43**, 299–306.

Shaw, T. L. and N. J. Stone: 1989, 'Nuclear Spin-Lattice Relaxation Attenuation Coefficients for Use in On-Line Nuclear Orientation Experiments'. *At. Data and Nucl. Data Tabl.* **42**, 339.

Stefanescu, I., J. Eberth, G. de Angelis, N. Warr, G. Gersch, T. Steinhardt, O. Thelen, D. Weisshaar, T. Martinez, A. Jungclaus, R. Schwengner, K. P. Lieb, E. A. Stefanova, D. Curien, and A. Gelberg: 2004a, 'Level structure of $^{69}$Se'. *Phys. Rev. C* **69**(3), 034333.

Stefanescu, I., J. Eberth, G. Gersch, T. Steinhardt, O. Thelen, N. Warr, D. Weisshaar, B. G. Carlsson, I. Ragnarsson, G. de Angelis, T. Martinez, A. Jungclaus, R. Schwengner, K. P. Lieb, E. A. Stefanova, and D. Curien: 2004b, 'High-spin states and band terminations in $^{69}$As'. *Phys. Rev. C* **70**(4), 044304.

Steinwedel, H., J. Jensen, and D. Hans: 1950, 'Hydrodynamics of nuclear dipole oscillations'. *Zeitschrift fuer Naturforschung A* **5**, 413–20.

Stone, N.: 1986, *Low-Temperature Nuclear Orientation*, Chapt. 13, Nuclear Magnetic Resonance of Oriented Nuclei I. Continous wave methods, pp. 641–692. Amsterdam: Elsevier Science Publishers B.V.

Towner, I. S.: 1987, 'Quenching of spin matrix elements in nuclei'. *Phys. Reports* **155**, 263.

Towner, I. S. and J. C. Hardy: 1973, 'Superallowed $0^+ \rightarrow 0^+$ nuclear $\beta$-decays'. *Nucl. Phys. A* **205**, 33–55.

Towner, I. S. and J. C. Hardy: 2002, 'Calculated corrections to superallowed Fermi beta-decay: New evaluation of the nuclear-structure-dependent terms'. *Phys. Rev. C* **66**(3), 035501.

Towner, I. S. and J. C. Hardy: 2003, 'The evaluation of $V_{ud}$, experiment and theory'. *J. Phys. G* **29**, 197–211.

Towner, I. S., J. C. Hardy, and M. Harvey: 1977, 'Analogue symmetry breaking in superallowed fermi $\beta$-decay'. *Nucl. Phys. A* **284**, 269–281.

Tramm, C.: 2004, 'MAPON-Untersuchungen am System $^{82}$BrFe'. Jun, Helmholtz Institut für Strahlen- und Kernphysik, Universität Bonn, D-53115 Bonn, Germany.

Van Isaker, P.: 1999, 'Dynamical Symmetries in the Structure of nuclei'. *Rep. Prog. Phys.* **62**, 1661–1717.

van Patter, D. M., F. Rauch, and B. Seim: 1973, 'Gamma transitions in $^{59}$Ni following the $\beta^+$ decay of $^{59}$Cu'. *Nucl. Phys. A* **204**, 172–184.

Van Walle, E.: 1985, 'On-Line Kernorientatie van Neutronarme Overgangskernen'. Ph.D. thesis, University of Leuven.

Vandeplassche, D., E. Van Walle, C. Nuytten, and L. Vanneste: 1983, 'Nuclear Orientation of Neutron Deficient Isotopes in the Z=50 Region'. *Nucl. Phys. A* **396**, C115–C124.

Vandeplassche, D., E. Van Walle, J. Wouters, N. Severijns, and L. Vanneste: 1986, 'Direct Spin Determination of On-Line-Separeted Isotopes by Nuclear Orientation and Nuclear Magnetic Resonance'. *Phys. Rev. Lett.* **57**, 2641–2644.

Vénos, D., A. Van Assche-Van Geert, N. Severijns, D. Srnka, and D. Zákoucký: 2000, 'The bahaviour of HPGe detectors operating at temperatures below 77 K'. *Nucl. Instr. and Meth.* **454**, 403–408.

Vénos, D., D. Zákoucký, and N. Severijns: 2003, 'Spin-Lattice Relaxation attenuation coefficients for On-Line Nuclear Orientation Experiments'. *At. Data and Nucl. Data Tabl.* **83**, 1–44.

von Brentano, P., A. F. Lisetskiy, N. Pietralla, A. Schmidt, I. Schneider, and C. Freiessner: 2004, 'Isospin mixing in the $4^+$ doublet of $^{54}$Co'. *Eur. Phys. J. A* **20**, 129–130.

Wannberg, B., J. O. Jönsson, and L. Sanner: 1970, 'Nuclear Magnetic Moment and Hyperfine Structure Anomaly of $^{103}$Ag and Nuclear Spin of 13 m $^{102}$Ag'. *Physica Scripta* **1**, 238.

Weissman, L., U. Köster, R. Catherall, S. Franchoo, O. Jonsson, V. N. Fedoseyev, V. I. Mishin, M. D. Seliverstov, J. Van Roosbroek, S. Gheysen, M. Hyuse, K. Kruglov, G. Neyens, and P. Van Duppen: 2002, 'Magnetic moments of $^{68}$Cu$^{g,m}$ and $^{70}$Cu$^{g,m_1,m_2}$ nuclei measured by in-source laser spectroscopy'. *Phys. Rev. C* **65**, 024315.

Wigner, E.: 1937, 'On the Consequences of the Symmetry of the Nuclear Hamiltonian on the Spectroscopy of Nuclei'. *Phys. Rev.* **51**, 106–119.

Wigner, E. P. and E. Feenberg: 1941, 'Symmetry properties of nuclear levels'. *Rep. Prog. Phys.* **8**, 274–317.

Wilkinson, D. H.: 1989, 'Evaluation of beta-decay I. The traditional phase space factors'. *Nucl. Instr. and Meth. A* **275**(2), 378–386.

Wilkinson, D. H.: 1990, 'Evaluation of beta-decay II. Finite mass and size effects'. *Nucl. Instr. and Meth. A* **290**(2-3), 509–515.

Wilkinson, D. H.: 1993, 'Evaluation of beta-decay III. The Complex Gamma-function'. *Nucl. Instr. and Meth. A* **335**(1-2), 305–309.

Wilkinson, D. H.: 1995a, 'Evaluation of beta-decay Part IV. The complex gamma function; practicalities'. *Nucl. Instr. and Meth. A* **365**(1), 203–207.

Wilkinson, D. H.: 1995b, 'Evaluation of beta-decay V. The Z-independent outer Radiative-Corrections for Allowed Decay'. *Nucl. Instr. and Meth. A* **365**(2-3), 497–507.

Wilkinson, D. H.: 1997, 'Evaluation of beta-decay, Part VI: The Z-dependent outer radiative corrections for allowed decay'. *Nucl. Instr. and Meth. A* **401**(2-3), 275–280.

Wilkinson, D. H.: 1998, 'Evaluation of beta-decay, part VII: The Z-independent outer radiative correction for unique-forbidden decay'. *Nucl. Instr. and Meth. A* **406**(1), 89–92.

Wouters, J., N. Severijns, J. Vanhaverbeke, W. Vanderpoorten, and L. Vanneste: 1990, 'On Line Nuclear Orientation: from Technique to New Physics'. *Hyp. Int.* **59**, 59–76.

Yamazaki, T.: 1967, 'Tables of Coefficients for Angular Distribution of Gamma Rays from Aligned Nuclei'. *Nuclear Data A* **3**, 1.

Zákoucký, D., D. Srnka, D. Vénos, V. V. Golovko, I. Kraev, T. Phalet, P. Schuurmans, N. Severijns, B. Vereecke, S. Versyck, and the NICOLE/ISOLDE Collaboration: 2004, 'HPGe detectors for low-temperature nuclear orientation'. *Nucl. Instr. and Meth.* **520**, 80–83.